DEVELOPMENT OF ANCHOR SYSTEMS FOR FRCM RETROFITS

Abdulla Zahmak

Thesis submitted to the University of Ottawa
in partial Fulfillment of the requirements for the degree of
Master of Applied Science in Civil Engineering

Department Civil Engineering
Faculty of Engineering
University of Ottawa

Dedication and acknowledgement

This work is dedicated to my family whose support made it possible. Special thanks to my supervisor professor Martin Noël for the passion and care he showed, providing guidance and sharing his expertise.

Abstract

Fabric Reinforced Cementitious Matrix (FRCM) composites utilize a mineral mortar matrix as a substitute for epoxy resin that is used for Fibre Reinforced Polymer (FRP). This eliminates issues associated with the low thermal compatibility of FRP with concrete, susceptibility to UV radiation, and sensitivity to high temperatures in which organic polymers undergo vitrification. This study discussed the effect of varying parameters like the number of Carbon-FRCM (C-FRCM) layers (1, 2 and 3 layers), different anchorage configurations (non-anchored, spike anchor, wrap anchor and mechanical anchor), bond length (300 or 200 mm), and the fabric type (unidirectional and bidirectional) on the direct shear behaviour of C-FRCM composites bonded to a concrete substrate, especially the fibre-matrix bond which is the most common debonding interface of FRCM composites. Calibrated models of the bond – slip behaviour are provided based on the fabric type and number of fabric layers.

The results indicate that the anchor type and the overall composite thickness are the main factors that control the failure mode of the composite. All properly anchored specimens using spike and wrap anchors failed due to fabric rupture. Moreover, a considerable number of the non-anchored specimens failed due to composite-substrate debonding, although premature fabric rupture was frequently observed.

Furthermore, specimens with bidirectional fabric demonstrated shallower penetration of the strain into the composite which may be due to the horizontal fabric strands providing some anchorage for the longitudinal strands. They also exhibited slip initiation at a higher stress compared to unidirectional specimens. In addition, slip initiation stress of unidirectional specimens decreased with more fabric layers which may indicate that the additional layers have a lower bond efficiency. For the same reason, specimens with three layers of fabric generally experienced deeper strain penetration into the composite than one-layered or two-layered specimens regardless of the anchor type. The results also indicate that the use of bidirectional fabric and anchorage systems decreases the strain penetration into the composite and correspondingly, the effective length is shortened.

Surface strain measurements captured using digital image correlation generally did not match the internal fabric strain values obtained from strain gauges.

Table of Contents

1.0 Introduction 1

2.0 Literature Review 2

2.1 FRCM composites overview 2

2.2 Anchorage systems for externally bonded composites 2

2.3 Strain Measurement Using DIC 12

2.4 Research significance 18

3.0 Experimental program 19

3.1 Overview 19

3.2 Test matrix and specimen details 19

3.3 Fabrication of test specimens and material properties 23

3.4 Test set-up and procedure 28

4.0 Results 31

4.1 Overview 31

4.2 B_2_30_20_N 33

4.3 B_2_30_20_S1 36

4.4 B_2_30_20_W 38

4.5 B_3_30_20_N 42

4.6 B_3_30_20_S2 46

4.7 B_3_30_20_W 50

4.8 U_1_20_20_M 54

4.9 U_1_20_20_W 58

4.10 U_1_30_20_N 62

4.11 U_1_30_20_S1 64

4.12 U_2_20_20_N 68

4.13 U_2_20_20_S1 71

4.14 U_2_20_20_W 76

4.15 U_2_30_20_N 79

4.16 U_3_20_20_N 84

4.17 U_3_20_20_S2 85

4.18 U_3_20_20_W 90

4.19 U_3_30_20_N 93

4.20 U_3_30_20_S2 98

5.0 Discussion 102
5.1 Non-anchored specimens 102
5.2 Spike anchor specimens 105
5.3 Wrap anchor specimens 108
5.4 Effect of anchor types on composite behaviour 110
5.5 Bond behaviour modelling 114
5.6 Effective length 122
5.7 Unexpected results and implications for design 123
6.0 Conclusion 126
7.0 References 128

List of figures

Figure 2.1: RC column strengthened with EB FRP sheets combined with spike anchors (Bournas et al., 2015)........ 3

Figure 2.2: Anchoring configurations and inclination angles of the the PBO-FRCM mesh (Trapko et al., 2015)........ 4

Figure 2.3: Fibres used for beams strengthened with: (a) carbon FRP; (b) steel FRP; (c) carbon FRCM; (d) steel FRCM composite (Gonzalez-Libreros et al., 2017) 6

Figure 2.4: Spike anchors installed into the beams (Gonzalez-Libreros et al., 2017) 7

Figure 2.5: PBO-FRCM anchorage configurations (Trapko & Musial, 2017)........ 7

Figure 2.6: Mechanical FRCM anchorage (Younis et al., 2017)........ 8

Figure 2.7: Tested anchorage systems (Aljazaeri et al., 2019)........ 9

Figure 2.8: PBO-FRCM anchorage techniques (Marcinczak et al., 2019)........ 11

Figure 2.9: DIC experimental setups for shear bond tests (a) and grid of virtual markers on the surface of the specimen (b) (Tekieli et al., 2017)........ 13

Figure 2.10: Full-field strain measurement for a strengthened beam as analyzed with DIC software DaVis (Pohoryles et al., 2017) 15

Figure 2.11: PBO-FRCM shear strengthening configuration with end-anchorage (Marcinczak & Trapko, 2019)........ 16

Figure 3.1: Unidirectional fabric (a) and Bidirectional fabric (b) 21

Figure 3.2: Layout and geometry of specimens U_1_30_20_N (a), U_1_30_20_S (b), U_1_30_20_W (c) and U_1_20_20_M in mm 23

Figure 3.3: Eight strain gauges on a 20 cm-long specimen........ 25

Figure 3.4: Prism surface roughened to a CSP 9 26

Figure 3.5: Carbon spike anchors installation........ 27

Figure 3.6: Tapes with speckle pattern to track global displacement 28

Figure 3.7: Front view schematic (a) and side view schematic of the gripping assembly (b)........ 29

Figure 3.8: Photography system for DIC 30

Figure 4.1: ruptured fabric (a) and close-up of some ruptured strands (b) 33

Figure 4.2: Load-slip curve obtained using DIC........ 34

Figure 4.3: strain profile obtained from DIC (a) and strain profile obtained from strain gauges (b) 35

Figure 4.4: Load-strain curve for every strain gauge 35

Figure 4.5: front view of the fabric (a) and close-up to the ruptured strands (b) 36

Figure 4.6: Load-slip curve obtained using DIC........ 37

Figure 4.7: strain profile obtained from DIC (a) and strain profile obtained from strain gauges (b) 37

Figure 4.8: Load-strain curve for every strain gauge 38
Figure 4.9: (a), (b), (c) and (d) different spots of ruptured fabric 40
Figure 4.10: load-slip curve obtained using DIC 41
Figure 4.11: strain profile obtained from DIC (a) and strain profile obtained from strain gauges (b) 41
Figure 4.12: Load-strain curve for every strain gauge 42
Figure 4.13: front view of the fabric (a) and close-up to the debonding surface (b) 43
Figure 4.14: load-slip curve obtained using DIC 43
Figure 4.15: strain profile obtained from DIC (a) and strain profile obtained from strain gauges (b) 44
Figure 4.16: Load-strain curve for every strain gauge 45
Figure 4.17: DIC generated 2D strain contour map 46
Figure 4.18: close-up to the right edge of the fabric (a) and close-up to the right edge of the fabric (b) 47
Figure 4.19: load-slip curve obtained using DIC 47
Figure 4.20: strain profile obtained from DIC (a) and strain profile obtained from strain gauges (b) 48
Figure 4.21: Load-strain curve for every strain gauge 49
Figure 4.22: DIC generated 2D strain contour map 50
Figure 4.23: front view of the fabric (a), close-up to a ruptured fabric spot (b) and close-up to another ruptured fabric spot (c) 51
Figure 4.24: load-slip curve obtained using DIC 52
Figure 4.25: strain profile obtained from DIC (a) and strain profile obtained from strain gauges (b) 53
Figure 4.26: Load-strain curve for every strain gauge 53
Figure 4.27: DIC generated 2D strain contour map 54
Figure 4.28: front view of the fabric (a) and side view of the debonding surface (b) 55
Figure 4.29: load-slip curve obtained using DIC 55
Figure 4.30: strain profile obtained from DIC (a) and strain profile obtained from strain gauges (b) 56
Figure 4.31: Load-strain curve for every strain gauge 57
Figure 4.32: DIC generated 2D strain contour map 58
Figure 4.33: ruptured fabric 59
Figure 4.34: load-slip curve obtained using DIC 59
Figure 4.35: strain profile obtained from strain gauges 60
Figure 4.36: Load-strain curve for every strain gauge 61
Figure 4.37: DIC generated 2D strain contour map 62
Figure 4.38: fabric rupture near the composite edge (a) and fabric rupture near the grip (b) 63
Figure 4.39: surface strain profile obtained from DIC 63

Figure 4.40: DIC generated 2D strain contour map 64
Figure 4.41: front view (a), fabric rupture near the composite (b), fabric rupture near the edge (c), fabric rupture near the grip (d) 65
Figure 4.42: load-slip curve obtained using DIC 66
Figure 4.43: surface strain profile obtained from DIC (a) and strain profile obtained from strain gauges (b)........ 67
Figure 4.44: Load-strain curve for every strain gauge 67
Figure 4.45: DIC generated 2D strain contour map 68
Figure 4.46: debonded composite 69
Figure 4.47: load-slip curve obtained using DIC 70
Figure 4.48: DIC generated 2D strain contour map 71
Figure 4.49: front view (a),debonded composite (b), ruptured fabric close-up (c) and (d) 72
Figure 4.50: load-slip curve obtained using DIC 73
Figure 4.51: strain profile obtained from strain gauges 74
Figure 4.52: Load-strain curve for every strain gauge 75
Figure 4.53: DIC generated 2D strain contour map 76
Figure 4.54: ruptured fabric 77
Figure 4.55: load-slip curve obtained using DIC 78
Figure 4.56: surface strain profile obtained from DIC 78
Figure 4.57: DIC generated 2D strain contour map 79
Figure 4.58: side view (a) and front view of the debonded composite (b) 80
Figure 4.59: load-slip curve obtained using DIC 81
Figure 4.60: surface strain profile obtained from DIC (a) and strain profile obtained from strain gauges (b)........ 82
Figure 4.61: Load-strain curve for every strain gauge 82
Figure 4.62: DIC generated 2D strain contour map 83
Figure 4.63: ruptured fabric 84
Figure 4.64: load-slip curve obtained using DIC 85
Figure 4.65: front view (a), cracking (b), splitting (c) and fabric rupture (d) 86
Figure 4.66: load-slip curve obtained using DIC 87
Figure 4.67: strain profile obtained from strain gauges 88
Figure 4.68: Load-strain curve for every strain gauge 89
Figure 4.69: DIC generated 2D strain contour map 90
Figure 4.70: front view (a) and ruptured fabric (b) 91

Figure 4.71: load-slip curve obtained using DIC 92
Figure 4.72: surface strain profile obtained from DIC 92
Figure 4.73: DIC generated 2D strain contour map 93
Figure 4.74: front view (a) and edge strands (b)........ 94
Figure 4.75: load-slip curve obtained using DIC 95
Figure 4.76: surface strain profile obtained from DIC (a) and strain profile obtained from strain gauges (b)........ 96
Figure 4.77: Load-strain curve for every strain gauge 97
Figure 4.78: DIC generated 2D strain contour map 98
Figure 4.79: fabric rupture close-up (a) and (b) and matrix cracking (c) 99
Figure 4.80: load-slip curve obtained using DIC 100
Figure 4.81: strain profile obtained from strain gauges 101
Figure 4.82: Load-strain curve for every strain gauge 101
Figure 5.1: failure stress of all the non-anchored specimens........ 102
Figure 5.2: strain profiles of the fabric at failure of non-anchored specimens 104
Figure 5.3: failure stress of all the spike anchored specimens 106
Figure 5.4: strain profiles of the fabric at failure of spike anchored specimens 107
Figure 5.5: failure stress of all the wrap anchored specimens 108
Figure 5.6: strain profiles of the fabric at failure of wrap anchored specimens 109
Figure 5.7: failure stress of all specimens with one or two fabric layers (a) and failure stress of all specimens with three fabric layers (b)........ 112
Figure 5.8: strain profiles of all specimens with one or two fabric layers (a) and strain profiles of all specimens with three fabric layers (b)........ 113
Figure 5.9: Eligehausen et al. (1983) modified bond–slip relationship 114
Figure 5.10: Calibrated stress–slip curves for specimens B_3_30_20_S2 (a) and U_2_30_20_N (b); and bond stress–slip curves for all modelled specimens (c)........ 116
Figure 5.11: Slip profiles for specimens B_2_30_20_W (a), B_3_30_20_S2 (b), U_1_20_20_W (c), U_2_30_20_N (d), and U_3_30_20_S2 (e) 119
Figure 5.12: Axial stress profiles for specimens B_2_30_20_W (a), B_3_30_20_S2 (b), U_1_20_20_W (c), U_2_30_20_N (d), and U_3_30_20_S2 (e) 120
Figure 5.13:Bond stress profiles for specimens B_2_30_20_W (a), B_3_30_20_S2 (b), U_1_20_20_W (c), U_2_30_20_N (d), and U_3_30_20_S2 (e) 122
Figure 5.14: idealized load - slip curve for FRCM (a) and the corresponding stress–transfer stages (D'Antino et al., 2014)........ 123

List of tables

Table 3.1: Geometric properties of Unidirectional and bidirectional fabrics 20
Table 5.1: slip measurements of non-anchored specimens 105
Table 5.2: slip measurements of spike anchored specimens 108
Table 5.3: slip measurements of wrap anchored specimens 110
Table 5.4: Calibrated parameters for each specimen 117

1.0 Introduction

Fabric Reinforced Cementitious Matrix (FRCM) is an effective concrete-retrofitting material, developed to overcome the issues associated with externally bonded Fibre Reinforced Polymer (FRP) sheets. FRP, which is applied using epoxy, is less tolerant to high temperatures and more susceptible to UV radiation compared to FRCM which depends on a cementitious matrix for adhesion. FRCM systems are also more breathable and are more compatible with the concrete substrate. Various anchorage solutions have been developed for FRP sheets since they are prone to debonding. Conversely, the effectiveness of anchors for FRCM systems have not been widely studied. Although FRCM generally exhibit improved bond characteristics, the design of anchorage regions may be critical for certain applications.

A limited number of previous studies have been conducted to model FRCM composites behaviour with different anchorage systems. However, none of them have analyzed external surface strains on the composite and the slip of carbon fabric reinforced cementitious matrix (C-FRCM), of spike and transverse wrap anchored specimens along with varying number of fabric layers, in a direct shear test configuration. To optimize the efficiency of FRCM anchors, a better understanding is required of the impact of different parameters on strain distribution, bond stress and failure mode. This study aims to clarify the effect of varying parameters like the number of C-FRCM layers (1, 2 and 3 layers), different anchorage configurations (non-anchored, spike anchor, wrap anchor and mechanical anchor), bond length (300 or 200 mm) and the fabric type (unidirectional and bidirectional) on the direct shear behaviour of C-FRCM, especially the fibre-matrix bond which is the most common debonding interface of FRCM composites.

First, this thesis provides a literature review (Chapter 2) to provide an oversight of previous work on the topic and understand the significance of this study. The experimental program is then explained in detail (Chapter 3) including the test set-up, followed by the test results of each specimen (Chapter 4). Finally, the results are discussed in detail and a model of the bond – slip is provided with a discussion of some of the unexpected results and how to avoid them (Chapter 5). Conclusions of the study are presented in Chapter 6.

2.0 Literature Review

2.1 FRCM composites overview

The two most popular externally bonded composite reinforcing systems for rehabilitation of concrete structures are fibre-reinforced polymers (FRP) and fabric reinforced cementitious matrices (FRCM). FRCM, which is the main subject of interest in this study, consists of fibres from similar material types as those used for FRP, except that fibre sheets are replaced with a fabric mesh with openings and mineral mortar is used as an adhesive instead of epoxy resin. There are several types of fibres that can be used for FRCM composites which also affect the mechanical properties significantly, including PBO, carbon, glass, and steel. The utilization of mineral mortar matrix as a substitute for epoxy resin is an advantage for FRCM as it eliminates the low thermal compatibility of FRP with concrete, susceptibility to UV radiation, and sensitivity to high temperatures in which organic polymers undergo vitrification (Trapko et al., 2015). However, the brittle matrix of the FRCM in most cases results in a lower bond strength at the fabric-matrix interface. Moreover, previous studies suggest that debonding at the fabric-matrix interface is the predominant failure mode of FRCM-strengthened reinforced concrete (RC) beams (Hadad et al., 2020; Aljazaeri et al., 2019; Sabau et al., 2017; Donnini et al., 2019); hence, there is a need to further study FRCM anchorage systems and bond behaviour.

2.2 Anchorage systems for externally bonded composites

Multiple studies have been conducted in the literature to analyze and understand the behaviour of various anchorage systems used to enhance the bond strength of FRP and FRCM composites. Bournas et al. (2015) investigated the effectiveness of carbon fibre spike anchors as a means of anchoring externally bonded (EB) fibre-reinforced polymers (FRP) and textile reinforced mortar (TRM) sheets into concrete. Experimental work included RC columns strengthened with various configurations of EB FRP and TRM sheets connected to RC footings via carbon fibre spike anchors as shown in Figure 2.1. Eight specimens were tested to investigate the effect of multiple parameters on the effectiveness of FRP anchors-composite sheets system, namely the number of anchors, the anchor cross sectional area, the type of EB sheets connected with the spike anchors, the bonding agent used to bind the sheet-anchor system and the presence of external confinement with composite material jacket. Specimens were tested under direct uniaxial tension applied to the column part, with tensile force applied through steel bars protruding from the column specimen and base block, respectively.

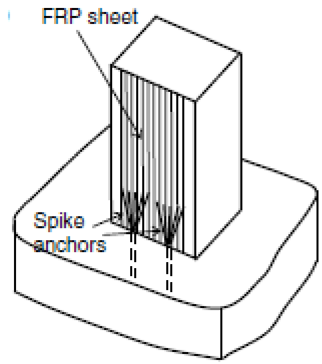

Figure 2.1: RC column strengthened with EB FRP sheets combined with spike anchors (Bournas et al., 2015)

No clear conclusion could be made about the preferable number of anchors with approximately the same cross-sectional area. The carbon fibre spike anchors comprised an effective anchorage system for preventing premature delamination of FRP and TRM sheets from concrete surfaces. When they were properly anchored into concrete and connected to EB FRP sheets, the spike anchors failed due to tensile rupture. Doubling the amount of spike anchors resulted in an increase of the anchors-FRP tensile capacity of 70%; however, the corresponding increase was only 50% for TRM sheets. The effectiveness of FRP spike anchors in connecting EB bidirectional textile reinforcement to concrete was 15% lower when mortar was used as a bonding agent instead of epoxy resin, and failure was controlled by anchor debonding rather than anchor rupture. Even when failure of the FRP anchors was due to tensile rupture, the failure strain was less than the uniaxial ultimate strain derived from material testing.

Trapko et al. (2015) also studied FRCM composites, but their objective was to analyze the functionality of reinforced concrete beams shear-strengthened with different designs of completely wrapped transverse PBO-FRCM composite mesh embedded in a mineral mortar. They varied the angle of inclination of the fibres with respect to the longitudinal axis, as well as the anchoring configurations for the mesh at the top and bottom surface of the beams. Anchoring configurations included overlapping the PBO-FRCM mesh and anchoring the mesh in the incisions in the concrete cover at the bottom and top of the beams with epoxy resin or mineral mortar as presented in Figure 2.2. The main tensile reinforcement was over-designed to prevent failure due to bending, and the stirrup spacing was greater than the beams' depth so that the beams were almost unreinforced in shear.

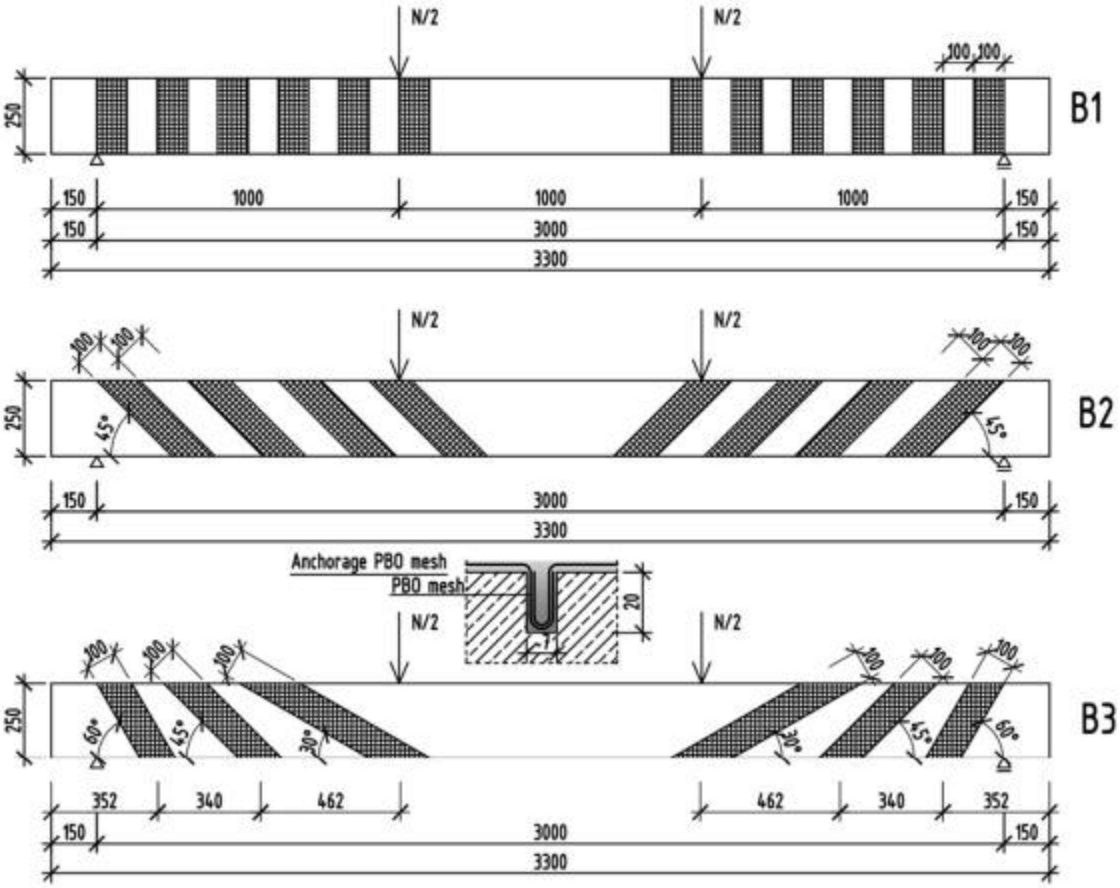

Figure 2.2: Anchoring configurations and inclination angles of the the PBO-FRCM mesh (Trapko et al., 2015)

Trapko et al. concluded that application of the PBO-FRCM system improves the functionality and shear strength of flexural elements. They observed that the shape of the anchoring system had a great impact on the effectiveness of the strengthening layer, but the positive impact of aligning composite fibres at an angle was not proven, with highest carrying capacity obtained with strips aligned at 90° (i.e., vertical). Moreover, the destruction was rapid (brittle failure), but observed deflections were approximately 2.5-3.0 times greater than the allowable deflection for an element without strengthening. All proposed methods of anchoring the external stirrups did not ensure a complete utilization of the tensile strength of the PBO mesh (failure occurred due to loosening of the mesh at the overlap or extraction of the anchor from the top surface of the concrete). In addition, before the first shear crack appeared and crossed the PBO stirrup, the composite followed concrete tensile strains during shear. The authors mentioned that strips of PBO mesh should be close enough to one another to prevent the propagation of too many cracks between them.

Sneed et al. (2016) tested the flexural response of RC beams strengthened using externally bonded steel-FRCM. Parameters varied were the presence/absence of the external layer of matrix, presence/absence of U-wrap anchorages, and loading rate. Beams were tested in four-point bending under quasi-static loading conditions, beyond their yield load and debonding load (where applicable), but only one beam was tested to failure because the other beams were to be repaired in a separate study.

Sneed noticed that RC beams strengthened in flexure with steel-FRCM failed due to debonding of the composite. The strengthening system increased the yield load by 15–21% relative to the un-strengthened beam. The debonding load was larger than the yield load, and the ratio of debonding load to yielding load ranged from 1.11 to 1.19. The debonding load and corresponding midspan displacement for the strengthened beam with U-wrap anchorages were similar to those of the strengthened beams without U-wraps. Furthermore, average values of the maximum fibre strain at debonding, ε_{max}, were less than the fibre rupture strain and larger than the average value determined from the direct-shear tests.

Moreover, Gonzalez-Libreros et al. (2017) compared the behaviour of RC beams strengthened in shear with externally bonded FRP and FRCM composites of two different fibre types (carbon and steel) as displayed in Figure 2.3, without anchors or anchored using 10 mm diameter and 250 mm long fanned out aramid fibre anchors that were impregnated with an epoxy resin, and placed in holes drilled 120 mm into the beam as shown in Figure 2.4. Experimental work included RC beams shear-reinforced with external FRP or FRCM composites with different internal shear reinforcement (stirrups) ratios. Fourteen RC beams, which were included in the experimental program, were strengthened using one layer of FRP or FRCM composite and two different stirrup spacings. For carbon FRP-strengthened beams, a unidirectional dry fibre fabric was used, while for the carbon FRCM-strengthened beams, a bidirectional, balanced, dry, open mesh textile was employed, while steel FRP and FRCM specimens were strengthened using brassed and galvanized unidirectional sheets, respectively. All beams were strengthened with a U-wrapped configuration continuous along the studied shear span.

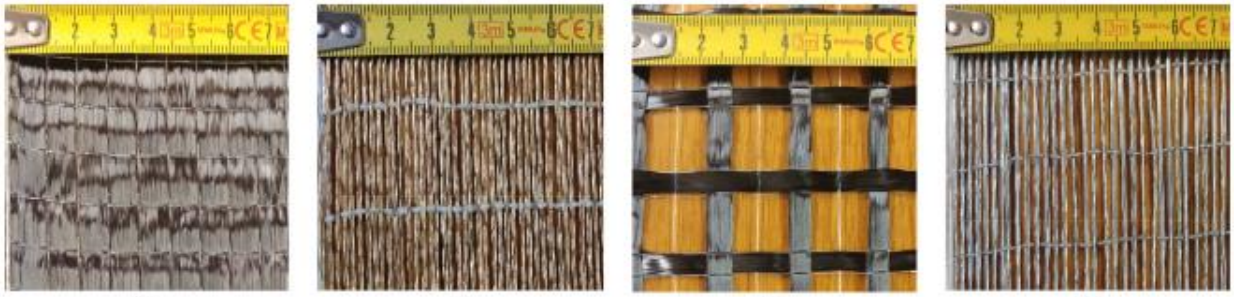

Figure 2.3: Fibres used for beams strengthened with: (a) carbon FRP; (b) steel FRP; (c) carbon FRCM; (d) steel FRCM composite (Gonzalez-Libreros et al., 2017)

Gonzalez-Libreros noticed that the shear strength of strengthened beams increased with increasing axial stiffness of the composite. For the steel FRP and FRCM-strengthened beams that had similar axial stiffness, the increase in shear strength was similar and did not vary depending on the type of matrix. In addition, they found that the effectiveness of the FRCM composite was related to the spacing of the internal reinforcement, where larger increases in the shear strength were observed for strengthened beams with larger stirrup spacing. For carbon FRCM-strengthened beams, local detachment of the entire composite and fibre slippage along the main crack were observed. While for steel FRCM-strengthened beams, failure was caused by detachment of the composite system, without damage to the concrete substrate. Anchors used in this study modified the failure mode, concrete crack pattern, and mid-span displacement of beams strengthened with FRCM composites. Beams strengthened with carbon FRCM composite with anchors exhibited a diagonal crack that formed around the anchors without detachment of the composite, unlike non-anchored FRCM composites, and the crack widths were larger. However, the use of anchors did not significantly increase shear strength. Fibre exploitation ratios for the carbon FRCM-strengthened beams were higher than those for the steel FRCM-strengthened beams.

Figure 2.4: Spike anchors installed into the beams (Gonzalez-Libreros et al., 2017)

Furthermore, Trapko & Musial (2017) described different ways of anchoring reinforcements made of PBO fibre mesh and tried improving their adhesion to concrete to improve the utilization of its properties as reinforcement for beams under bending by applying a single force in the middle of their span. Twelve RC beams were strengthened against bending with a single layer of PBO mesh. They used three types of PBO mesh reinforcement anchorage; 100 mm wide stirrups wrapped around the beam at the ends of the longitudinal reinforcement, ends of the longitudinal reinforcement wound on composite rods made of glass fibre and bonded, and longitudinal reinforcement covered with a layer of flexible mortar along its entire length. The three anchorage configurations are displayed in Figure 2.5.

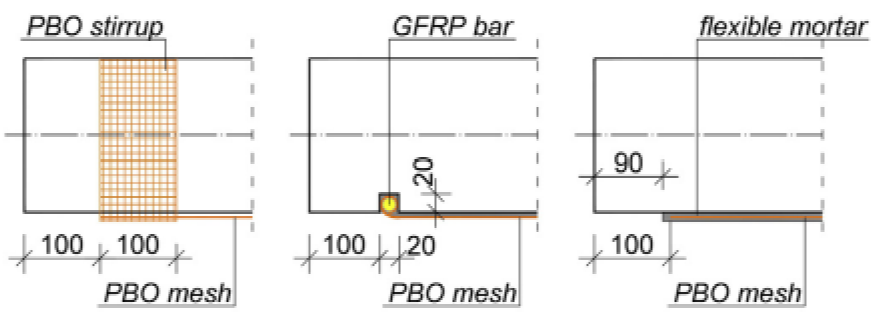

Figure 2.5: PBO-FRCM anchorage configurations (Trapko & Musial, 2017)

They observed that mineral mortar being part of the PBO-FRCM system was characterized by poor adhesion to concrete, underwent small deformations under tension, and cleaning of the substrate only minimally improved adhesion. In the initial loading stage, the composite and the matrix followed the deformations of the concrete but under greater strains, in some places the mortar cracked and peeled off and the mesh debonded from the concrete. As a result, it was difficult to estimate the degree to which the reinforcement was mobilized. In the case of the first two anchor configurations (the longitudinal FRCM reinforcement anchored at their ends), the maximum strains in the longitudinal reinforcement after the concrete cracked decreased to about 0.1-0.2% from 0.2-0.3% at the instant of cracking. However, in the case of the third anchor configuration (longitudinal reinforcement covered with a layer of flexible mortar), when the ultimate tensile strength of the concrete was exceeded, a marked increase in the longitudinal strains was registered at mid-span of the beams and the longitudinal reinforcement did not debond from the concrete in the crack area. The PBO mesh did not rupture and no ultimate strains corresponding to the rupture were reached. They also mentioned that it would be optimal to anchor the reinforcement ends and to cover the reinforcement with flexible mortar, so that PBO mesh used as longitudinal reinforcement would certainly be even better mobilized.

Following previous studies, Younis et al. (2017) investigated the efficiency of three different FRCM systems for the strengthening of RC beams which were critical in shear, but focused on the orientation of the FRCM strips and the effect of the end-anchorage of the FRCM strips. Sixteen shear-critical RC beams without stirrups were shear-strengthened using FRCM with different configurations within the shear-critical span and tested under three-point loading. Four different test variables were considered; FRCM type (carbon, PBO, and glass), strengthening scheme (full/continuous FRCM plate or a set of spaced FRCM strips), strengthening orientation (vertical or 45°), and FRCM anchorage by mechanically fixing two FRP plates on top and bottom of the strip as shown in Figure 2.6.

Figure 2.6: Mechanical FRCM anchorage (Younis et al., 2017)

Younis concluded that FRCM anchorage had an insignificant effect on the strength enhancement of the strengthened beams. The average gain in the load carrying capacity was 51% for the strengthened beams when compared to the non-strengthened reference. More ductile behaviour was generally observed as well for all strengthened beams, where deflection at failure reached up to 2.4 times that reported for the reference specimen. While debonding of the strengthening layer was the common type of failure mode for all specimens, crack width values were noticed to be smaller for carbon–FRCM systems than those reported for the PBO– or glass–FRCM systems. Crack widths corresponding to the continuous FRCM systems were smaller than those reported for the intermittent counterparts. Younis stated that reasonable agreement was achieved between the experimental and the theoretically (ACI 549-driven method) predicted values for load carrying capacity.

Similar to previous studies, Aljazaeri et al. (2019) investigated the influence of anchorage systems used to increase the flexural performance of FRCM composites either by delaying or preventing debonding. Seven medium-scale beams were tested under four-point loading with two different anchorage systems; glass spikes and a novel U-wrapped PBO strip as illustrated in Figure 2.7. Cement-based mortar was made of a combination of Portland cement, silica fume, and fly ash as a binder and had less than 5% polymer. It also contained glass fibres to improve the bond between the PBO mesh and the cement mortar and to provide better tensile properties.

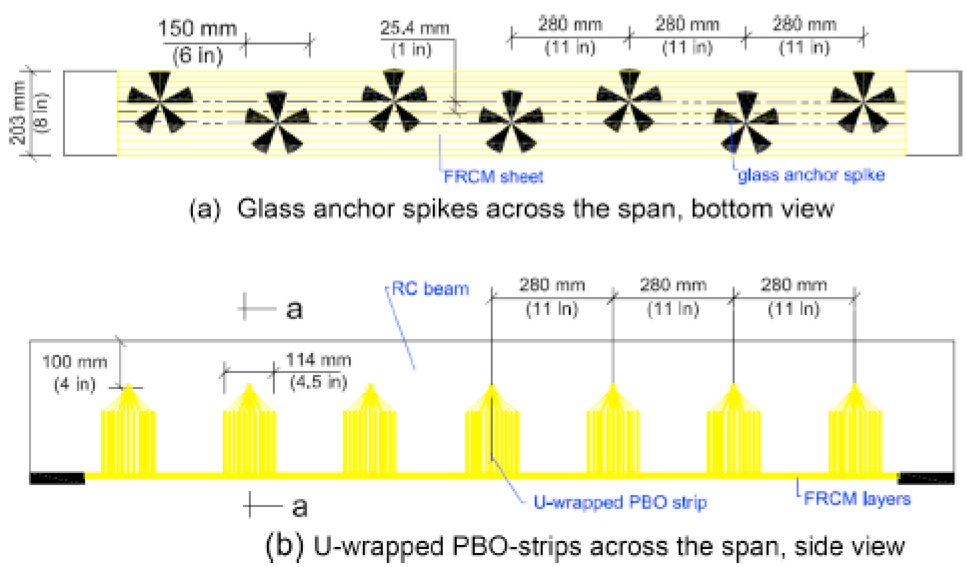

Figure 2.7: Tested anchorage systems (Aljazaeri et al., 2019)

Non-anchored beams exhibited intermediate debonding at the maximum loaded area and endplate debonding at the free end, with debonding at the interface between the PBO sheets and the cementitious matrix, similar to beams anchored with glass spikes. U-wrapped PBO strips anchored beams exhibited a slippage of the PBO sheets and U-wrapped PBO strips out of the cementitious matrix at the mid-span. The mode of failure was improved from intermediate debonding and end plate debonding to the slippage of PBO sheets, while anchorage systems contributed to delay the premature debonding failure mode and increase the ultimate loads in beams. Beams anchored with glass spikes and U-wrapped PBO strips had 10% and 24% higher ultimate load than the non-anchored beam, respectively.

Marcinczak et al. (2019) researched the effect of different types of anchorages on shear strength and mobilization of the PBO-FRCM composite for T-shaped beams. Ten T-shaped RC beams were strengthened with U-shaped PBO-FRCM materials in an identical configuration. The PBO mesh used was a bidirectionally woven sheet with four times more fibres in the main direction as in the lateral direction. Beams were anchored with 3 different techniques; PBO strips wound on a GFRP composite bar which was embedded under the slab, PBO fibre cord with dedicated mineral mortar inserted into 10 mm holes, and an anchorage in the form of a 150 mm wide PBO strip glued under the slab to the beam along its whole length and the direction of the fibres was perpendicular to the shear direction of the mesh strips. The anchorage techniques are shown in Figure 2.8.

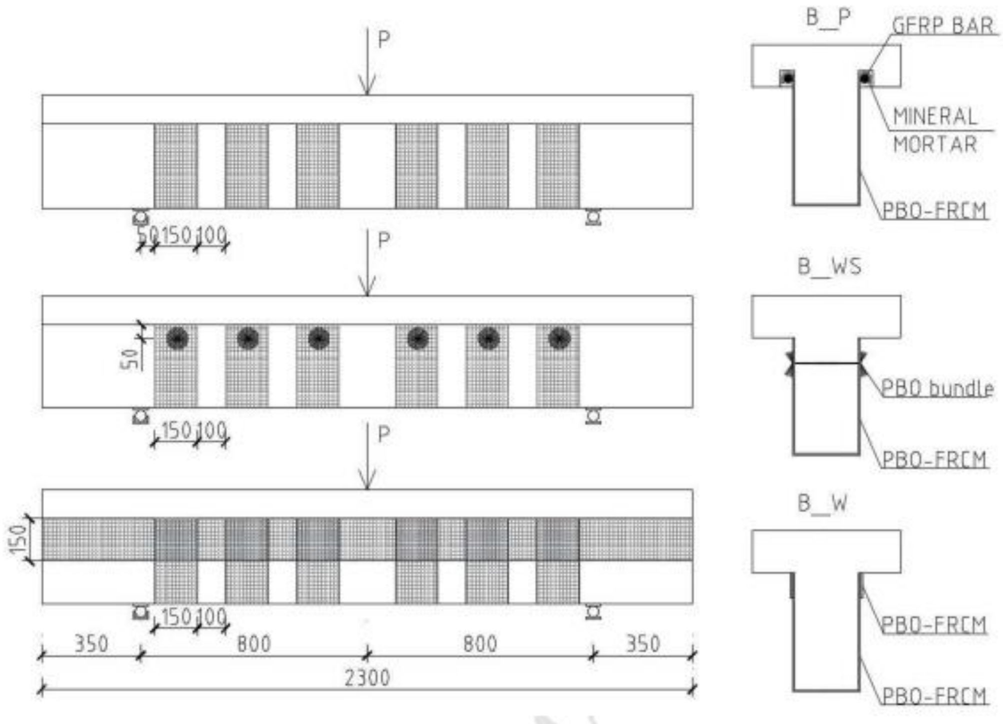

Figure 2.8: PBO-FRCM anchorage techniques (Marcinczak et al., 2019)

In their research, Marcinczak found that the shear strength of the strengthened beams increased by 10–27% in comparison with the un-strengthened reference beam. For all strengthened beams, the failure mechanism consisted in the development of an inclined crack in the web and in the slab, with propagation of a crack along/around the anchorage, resulting in the debonding of the latter and the outer stirrups from the surface of the member, in the layer between the fibres and the matrix. Maximum strains in the anchored composite reached 8.23%, which amounts to 47% of the ultimate tensile strain. In the tested beams strengthened with the PBO-FRCM system without anchorage, the maximum strains in the composite reached 3.5%, while the largest shear capacity increase of 27% was obtained with the anchorage that consisted of a PBO mesh strip along the entire length of the beam. The presence of reinforcement did not change the slope of the diagonal features (approximately 45°), and diagonal cracks in the strengthened beams with strip anchorage appeared under almost twice the load than in the reference beam without strengthening. The authors mentioned that the estimated shear strength of T-beams according to standard ACI549.4R-13 was underestimated.

In addition to previous studies, Wakjira & Ebead (2019) conducted an experiment on shear-critical deep RC beams strengthened with FRCM applied using both the externally bonded and near-surface embedded techniques, considering the effects of the internal transverse reinforcement (ITR) configuration (aligned and unaligned with the FRCM strips) and various types of FRCM fabrics (carbon, glass, and PBO). Fourteen rectangular RC deep beams strengthened with three layers of fabric plies using a side-bonded configuration (not U-wrapping) were tested in a three-point loading configuration.

They concluded that the configuration of the ITR relative to the FRCM strips did not show a significant effect on the percentage gain in the load capacities of the strengthened beams. They also stated that the NSE technique was beneficial in eliminating the undesired debonding failure due to an improved FRCM/concrete bond performance leading to FRCM tensile rupture (no sign of FRCM debonding was observed), while beams strengthened with the EB-FRCM failed due to the debonding of the composite from the concrete. Beams strengthened with the NSE-FRCM showed a higher gain in P_{max} compared to the EB-FRCM (NSE-FRCM increased the load capacities of the beams by an average of 41.0% compared to an average of 27.9% increase in P_{max} by the EB-FRCM). A strut-and-tie model was used to predict the load capacities of the FRCM-strengthened deep beams and exhibited a good agreement with the experimental results for both EB-FRCM and NSE-FRCM.

2.3 Strain Measurement Using DIC

Digital image correlation (DIC) has grasped the interest of researchers as a relatively new strain measurement method that has great potential. DIC is a non-contact optical technique which compares digital photographs of a specimen at different stages of deformation to measure strain and displacement. Through specially developed software, the DIC system can make high-resolution measurements of surface displacement and build up full field 2D and 3D deformation and strain maps, using input datasets which can be obtained from a wide variety of sources including images, surface roughness maps, or 2D surfaces of structures (McCormick and Lord, 2010).

DIC has several advantages over conventional methods as it is simple to implement providing cost-effective precise results leading to a huge range of potential applications, including examining the development and uniformity of strain in materials, crack tip and crack propagation studies, structural deflections, high temperature strain mapping, and dynamic vibrational analysis (McCormick and Lord, 2010). Moreover, DIC is significantly cheaper and easier to use outside the laboratory compared to other techniques as it uses conventional digital photography. Nevertheless, DIC suffers from a few limitations. Measurement accuracy is significantly dependent on the size of the measured area, lighting change during the test, the angle between the camera and analyzed surface, digital camera noise, lens quality, and preparation of the tested surface (Krawczyk et al., 2019).

Tekieli et al. (2017) used DIC in combination with displacement transducers and extensometers for tensile tests on dry textile specimens and composite coupons, as well as composite-to-substrate shear bond tests done to masonry, as can be seen in Figure 2.9. Tensile tests on composites were carried out on coupons of composites comprising steel, carbon, or basalt textiles and either organic (epoxy resin) or inorganic (cement or lime mortar) matrices. Global displacements were acquired by an LVDT and local strains were detected by a 50 mm gauge extensometer in addition to two displacement transducers, while digital images were taken at constant time intervals with two different software programs.

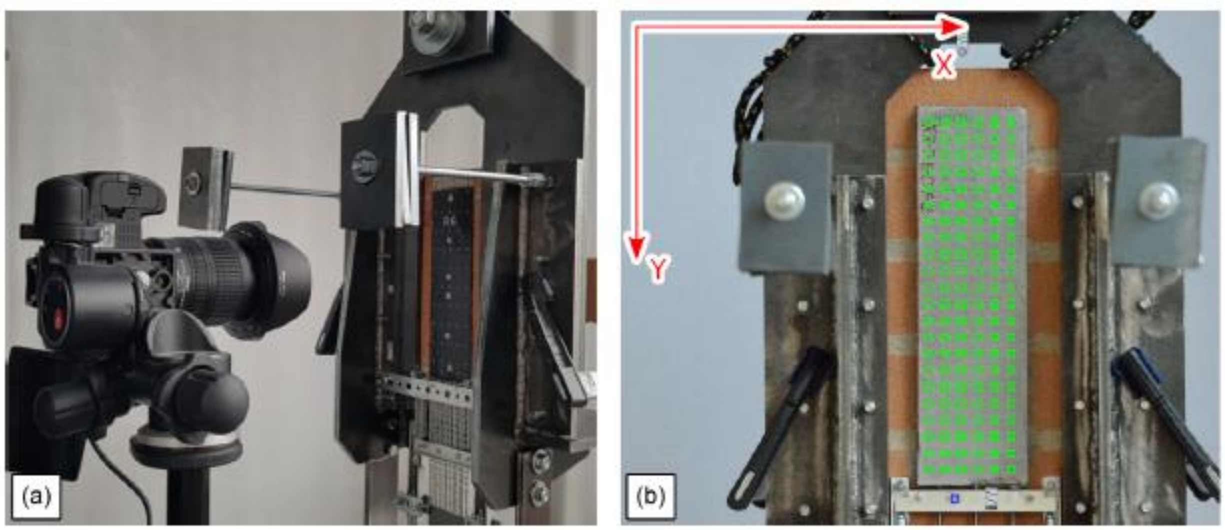

Figure 2.9: DIC experimental setups for shear bond tests (a) and grid of virtual markers on the surface of the specimen (b) (Tekieli et al., 2017)

Tekieli found that DIC was reliable and did not rely on the software selected for image processing. Moreover, in direct tensile tests, DIC measured the average strain over the entire length of the specimen excluding the gripping areas, thus indicating possible slippage at clamping by comparison with the integrated transducer, without being affected by crack occurrence or local strain concentrations. In addition, DIC tracked the occurrence, number, location, width and distance of cracks, even before they become visible to the naked eye and automatically, while its reliability was not affected by crack location. However, only the outer surface of the specimen can be monitored, so no direct information is provided on the textile within the matrix.

Moreover, Sabau et al. (2017) compared Image Correlation Systems (ICS), Point Tracking and DIC, and traditional contact measurement approaches such as LVDTs and electrical strain gauges, for determining displacement and strain to characterize the bond behaviour of FRCM composite to concrete joints. Three specimens were tested in single-lap direct shear tests with composites comprised of a bidirectional balanced dry carbon fibre net and a cementitious mortar matrix of 330 mm bonded length. The commercially available 3D ICS used contained two 5 Megapixel CCD digital cameras equipped with 12 mm focal length lenses.

Sabau observed that the strain in the bare fibre bundles at the loaded end measured using ICS (PT method) showed good correlation with the measurements obtained from electrical strain gauges, and the load-global slip response of each individual fibre bundle and of the FRCM-concrete joint, can be determined with a higher accuracy compared to LVDTs and overcome the need to attach additional elements to the tested specimen. ICS results demonstrated that in single-lap direct shear setups, the applied load was not distributed uniformly to the fibre bundles but was rather randomly distributed based on the bond properties of each bundle. Furthermore, sudden drops in the applied load were shown to be correlated with the formation of cracks. Debonding of the carbon-FRCM composite occurred at the matrix-fibre interface.

Similar to previous studies, Pohoryles et al. (2017) compared five monitoring techniques which were strain gauges, fibre Bragg grating (FBG) sensors, LVDTs, DIC and acoustic emission (AE) sensors, for monitoring strain, displacement, cracking, and debonding of beams retrofitted with FRP and FRCM. Six T-beam specimens were tested under four-point loading. For three beams, unidirectional carbon fibre reinforced polymer (CFRP) for flexural strengthening was applied to the bottom face of the beam and applied as U-strips for anchorage and shear strengthening. Whereas for the two beams strengthened with FRCM, one or two layers were applied as a U-wrap along the length of the beam. Figure 2.10 presents full-field strain measurement for one of the tested beams as analyzed with DIC software.

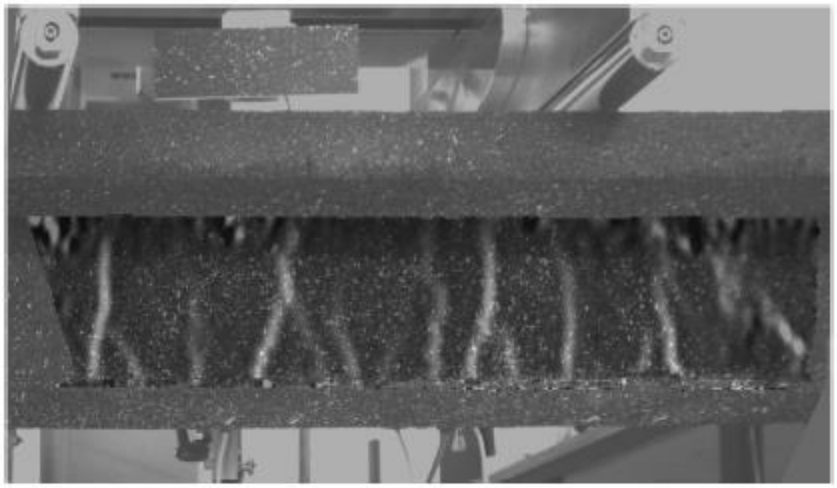

Figure 2.10: Full-field strain measurement for a strengthened beam as analyzed with DIC software DaVis (Pohoryles et al., 2017)

Pohoryles noticed that DIC provided accurate strain and displacement measurements that were comparable to those produced by classical instrumentation and could monitor them simultaneously and hence substitute for LVDTs and strain gauges at the same time. However, they stated that DIC could not measure deformations that occurred below the surface of the retrofitting material or on the steel reinforcement, so AE sensors were needed to accurately detect damage in a specimen below the retrofitting material. They also stated that AE can be used to anticipate the failure of RC beams strengthened with composite materials because the rate of AE hits is directly correlated with specimen damage and changes at yield and maximum force. Different crack types and fracture mechanisms were well characterized by analysis of the Average Frequency (AF) and RA (rise time/hit amplitude) parameters of AE recordings. Additionally, AE analysis well characterized FRP debonding, but it did not do as well with FRCM debonding, which can be explained by the nature of the debonding fracture mechanism.

D'Antino and Papanicolaou (2018) conducted tensile tests on four different TRM composites (carbon, glass, basalt, and steel fibres) using two tensile test set-ups (clamping-grip method applied to rectangular prism specimens and curved flange method applied to dumbbell specimens), then measured strain along specimens using LVDTs and DIC method. They tested twelve specimens (4 rectangular prisms and 8 dumbbells). For the rectangular prisms, displacements were measured by two LVDTs of 210 mm gauge length, one on each side of the specimen. Whereas dumbbell specimens' longitudinal strain was measured using one LVDT with a gauge length of 210 mm applied in the central part on one side of the specimen with DIC employed on the other side of the specimen using a frequency of 1 Hz with a 2 Megapixel resolution camera.

Results showed that the two test set-ups provided completely different behaviours for the same composite material and results of the tensile tests should be related to the test set-up employed. Moreover, pressure induced by wedges using the clamping-grip method influenced the matrix-fibre bond properties within and close to the clamping area, which in turn affected the specimen results and, in some cases, changed the stress-strain response from a trilinear to a bilinear one. The effect of the clamping pressure depended on the specific composite used and should be properly investigated.

Furthermore, Marcinczak and Trapko (2019) measured the deformation of RC T-shaped beams strengthened in shear with PBO-FRCM composites using strain gauges and the DIC method and compared them. Two RC T-beams were tested, with one beam as a reference beam without strengthening, and the second one was shear-strengthened with PBO-FRCM. The flexural reinforcement was designed to prevent failure due to bending before exhausting the shear strength with one beam strengthened with one layer of U-wrapped PBO-FRCM strips at a spacing of 100 mm wound at the ends on a GFRP bar and glued in a cut under the flange, as shown in Figure 2.11. In addition, 50 mm long strain gauges were glued at half the height of the beams with 25 mm gauges glued to the place of anchors on both sides of the beam.

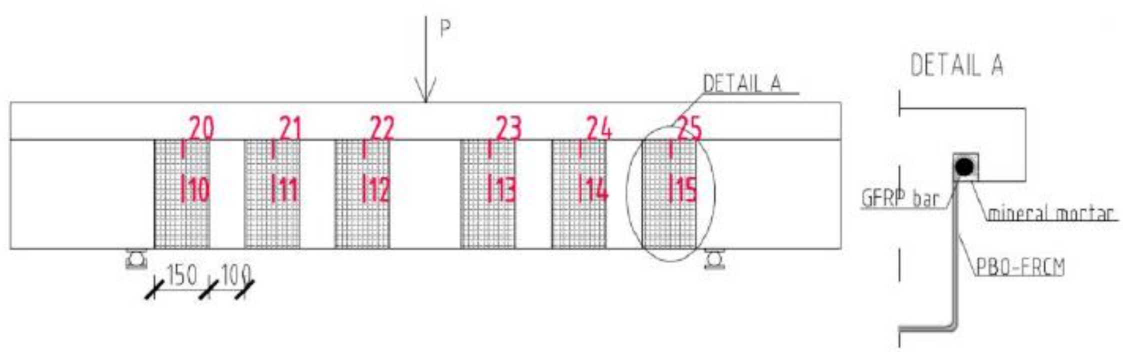

Figure 2.11: PBO-FRCM shear strengthening configuration with end-anchorage (Marcinczak & Trapko, 2019)

Marcinczak and Trapko mentioned that the failure mechanism of the strengthened beam consisted in debonding of the PBO mesh, accompanied by the development of diagonal cracks, which is where detachment and deformation started. Using the DIC method, it was possible to determine what the course of the diagonal crack would look like before it initiated, and it could be monitored.

Whereas strain gauges failed to determine the maximum deformations, because the strain gauges were installed in locations where the deformations were smaller. Moreover, with the DIC method it was possible to determine the maximum effort of PBO fibres, and show that redistribution of deformations occurred in each strip of the PBO-FRCM composite as the load increased.

Donnini et al. (2019) conducted an investigation on beams subjected to tensile stress with different configurations (one reinforced with a single layer of bidirectional glass fabric and three others with different fabric overlap lengths). They then developed a phase-field model that accounted for fracture of the matrix and fabric, and possible slippage at the fabric-to-matrix interface, using a finite element code to simulate the tensile behaviour of FRCM systems and the effects of using different fabric overlap lengths. Their investigation included a total of 20 FRCM coupons with four different specimen configurations: single layer of fabric, overlap of 100, 150, and 200 mm. Global displacement was recorded by the LVDT integrated in the testing machine, while the local axial deformation was measured using a clip-on extensometer with a 100 mm gauge length and DIC was performed with a digital camera at 2 frames per second.

Results showed that specimens reinforced with a single layer of glass fabric failed due to fabric rupture within the free length of the specimen, whereas FRCM specimens with fabric overlap length of 100 mm failed due to slippage at the overlay interface. The minimum glass fabric overlap length, which allows to restore the specimen's integrity and the complete transfer of tensile stresses from one fabric to another, was about 150 mm, with the maximum stress attained at failure being almost the same as that of specimens with continuous fabric, while the stiffness was greatly increased. Moreover, DIC allowed to detect the number and width of the cracks at any load value and the strain field on the whole surface of the specimens, and the variational model accurately captured all the evolution stages leading up to failure. Stress–strain curves obtained from simulations were compared with the experimental ones providing a great predictive capability.

In addition, D'Antino and Poggi (2019) studied fibre textile tensile strength and elastic modulus through tensile tests on specimens comprising bare glass fibre textiles and glass fibre textiles impregnated with epoxy resin and lime-based mortar. They used an extensometer with a gauge length of 25 mm attached to one of the edge fibre bundles, and used DIC for all specimens impregnated with resin and mortar. DIC was performed with a camera of 20.9 Megapixel resolution and Vic-2D software.

They found that epoxy resin penetrated within the fibre bundles, redistributing the tensile stresses among the fibre filaments, which led to an average tensile strength 256% higher than that obtained with the bare fibre textile. In contrast, impregnating the textile with the lime-based mortar slightly improved the tensile strength with respect to that of the bare textile, due to the difficulty of the mortar in penetrating within the fibre bundles. The fibre elastic modulus was slightly affected by the presence of an impregnating matrix. They also mentioned that tensile tests on specimens comprising glass textile and inorganic mortar are recommended to obtain the maximum tensile stress that would be provided by the fibre textile in real applications.

2.4 Research significance

Using a wide range of recently developed techniques and equipment, the reviewed studies have been conducted to model FRCM composites behaviour with different anchorage systems. However, none of the previous studies have analyzed crack formation and the displacement of carbon fabric reinforced cementitious matrix (C-FRCM), with and without spike and transverse wrap anchors along with varying number of fibre layers, using DIC in a direct shear test configuration. To optimize the efficiency of FRCM anchors, a better understanding is needed of the effects of different parameters on local strain distribution and load transfer efficiency. This research provides the opportunity to understand the effect of varying the number of C-FRCM layers and different anchorage configurations on the direct shear behaviour of C-FRCM, especially the fibre-matrix bond which is the main setback of FRCM composites.

3.0 Experimental program

3.1 Overview

The experimental program includes a total of 25 specimens. Each specimen consists of one or more C-FRCM layers externally bonded to a concrete prism (450 mm x 400 mm x 200 mm), to be tested under single lap shear test. An inorganic matrix layer was used to bond the carbon fabric to the surface of the prism. The specimens differ in terms of fabric type (unidirectional or bidirectional), number of fabric layers (one, two, or three layers), length of the bonded fabric (200 mm or 300 mm), and anchor type (none, spike anchor, transverse wrap of 150 mm width, or mechanical anchors). A speckle pattern was applied to the surface of the FRCM using white paint and black dots in order to measure the strain on the exposed face using DIC.

3.2 Test matrix and specimen details

A total of 25 single-lap shear specimens were prepared with four varying parameters and bonded to concrete prisms that are 450 mm high, 400 mm wide, and 200 mm thick. Two types of carbon fabric were used, unidirectional and bidirectional. The unidirectional carbon fabric (CSS-UCG) is a high-strength, corrosion-resistant carbon FRP grid designed specifically to be installed with CSS-CM cementitious matrix to create a FRCM composite for structural reinforcement applications. The CSS-CM cementitious matrix was utilized for all test specimens to ensure good compatibility with the carbon grid. The unidirectional grid is lightweight, weighing only 440 g/m^2, making it convenient to work with. Every strand within the grid is 3.7 mm wide and the spacing between every 2 strands is 12 mm from inner edge to inner edge. Thus, each 200 mm width of the fabric used in this study includes 12 strands. Horizontal strands made of synthetic fibres are used by the manufacturer to keep the longitudinal carbon strands in place and to keep the shape of the grid intact (although the bond between the horizontal synthetic fibres strands and the vertical carbon strands is relatively weak, allowing carbon strands to slip out of place while applying the cementitious matrix and trowelling the surface to fabricate the composite). The unidirectional fabric can be seen in Figure 3.1 (a). The bidirectional fabric, on the other hand, has different geometry and physical properties, although it shares the same manufacturer and material with the unidirectional carbon fabric. The bidirectional grid weighs 260 g/m^2 which is much lighter than the unidirectional grid at 60% of the latter's weight. The inner-inner spacing between every 2 strands is 17 mm which is bigger than the unidirectional grid spacing, and every strand within the grid is 2.7 mm wide, in both vertical and horizontal directions. Hence, a width of 200 mm of the fabric for each bidirectional specimen includes 10 strands as shown in Figure 3.1 (b). The bond between the vertical and horizontal carbon strands of the carbon grid is much stronger compared to that of the unidirectional fabric, making it much sturdier, and easier to work with and handle while fabricating the specimens. Table 3.1 compares the geometric properties of unidirectional and bidirectional fabric.

Table 3.1: Geometric properties of Unidirectional and bidirectional fabrics

Material	Weight (g/m^2)	Inner-Inner strand spacing (mm)	Strand width (mm)	No. of strands per 20 cm wide specimen
Unidirectional carbon fabric	440	12	3.7	12
Bidirectional carbon fabric	260	17	2.7	10

Each type of fabric was tested with bonded length of either 200 mm or 300 mm while the width was fixed at 200 mm across all specimens. These dimensions were chosen based on previous studies which found that the effective bond length of carbon FRCM composite is longer than 200 mm (Sabau et al., 2017). Tested specimens had 3 different anchorage configurations. C-FRCM in 8 specimens was anchored using carbon-FRP spike anchors as shown in Figure 3.2. The spike anchors were over-designed to avoid rupture within the anchor itself and to force the failure to occur within the composite. Therefore, one spike anchor was used for specimens with one or two layers of carbon fabric, while two were used for the ones with 3 layers of carbon fabric. The CSS-PCA3712-4 spike anchors which were manufactured and supplied by Simpson Strong-Tie, are high-strength corrosion-resistant carbon anchors designed to be laminated with epoxy resin to create C-FRP composite anchor. The spike anchor is comprised of 2 sections, a factory precured sand-coated embedded length of 10 cm, for better quality control, and a flexible 20 cm long fan section that can be spread and bonded to the carbon fabric using epoxy resin as can be seen in Figure 3.5. The total length of the anchor is approximately 30 cm including both embedded and fan sections, and the diameter of the precured portion is 9.5 mm.

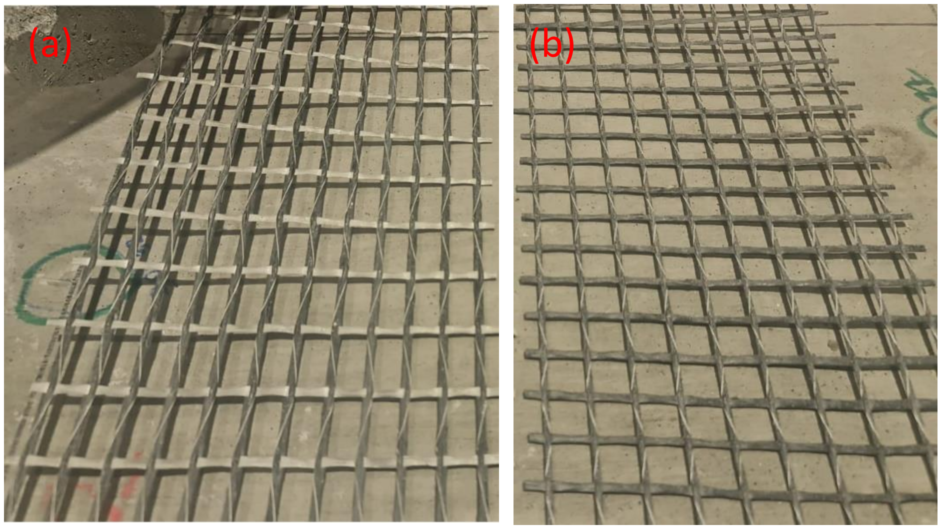

Figure 3.1: Unidirectional fabric (a) and Bidirectional fabric (b)

Another eight specimens were anchored using a transverse wrap with a width of 150 mm as presented in Figure 3.2. The width of the transverse wrap anchor was chosen to be 150 mm for practical reasons related to the specimen size and test equipment geometry. One specimen was anchored using mechanical anchorage. Construction screws were used for the mechanical anchor that are #6x2, which have a length and a diameter of 51 mm (2 in) and 3.3 mm (0.13 in), respectively. Washers were used in combination with the screws to distribute the anchoring force of the screws as shown in Figure 3.2. The remaining eight specimens were not anchored in order to be compared with anchored ones and to observe the change in bond behaviour due to the presence of different types of anchorage.

The prepared specimens were assigned names based on the fabric type, number of fabric layers, length of the bonded fabric, width of the bonded fabric and anchor type, respectively. The details of some specimens and geometry are demonstrated in Figure 3.2. The letter (U) at the start denominates unidirectional fabric while the letter (B) denominates bidirectional fabric, followed by a number representing the number of fabric layers (1, 2, or 3). The following two numbers represent the bonded length and the width of the FRCM in cm, respectively. The last letter represents the anchorage type used for the specimen with (N) denoting there is no anchorage, (S) denoting there is a spike anchor, (M) for mechanical anchors, and (W) denoting there is a transverse wrap anchor within the specimen. The test matrix is presented in Table 3.2 showing summarized details of the specimens.

Table 3.2: Test matrix and specimen characteristics

Specimen name	Fabric type (unidirectional or bidirectional)	Number of layers	Length	Width	Anchor type (e.g. none, spike [#], transverse wrap [width])
U_1_20_20_N	Unidirectional	1	200	200	none
U_1_20_20_S	Unidirectional	1	200	200	spike [1]
U_1_20_20_W	Unidirectional	1	200	200	wrap [150mm]
U_1_20_20_M	Unidirectional	1	200	200	mechanical
U_1_30_20_N	Unidirectional	1	300	200	none
U_1_30_20_S	Unidirectional	1	300	200	spike [1]
U_1_30_20_W	Unidirectional	1	300	200	wrap [150mm]
U_2_20_20_N	Unidirectional	2	200	200	none
U_2_20_20_S	Unidirectional	2	200	200	spike [1]
U_2_20_20_W	Unidirectional	2	200	200	wrap [150mm]
U_2_30_20_N	Unidirectional	2	300	200	none
U_2_30_20_S	Unidirectional	2	300	200	spike [1]
U_2_30_20_W	Unidirectional	2	300	200	wrap [150mm]
U_3_20_20_N	Unidirectional	3	200	200	none
U_3_20_20_S	Unidirectional	3	200	200	spike [2]
U_3_20_20_W	Unidirectional	3	200	200	wrap [150mm]
U_3_30_20_N	Unidirectional	3	300	200	none
U_3_30_20_S	Unidirectional	3	300	200	spike [2]
U_3_30_20_W	Unidirectional	3	300	200	wrap [150mm]
B_2_30_20_N	Bidirectional	2	300	200	none
B_2_30_20_S	Bidirectional	2	300	200	spike [1]
B_2_30_20_W	Bidirectional	2	300	200	wrap [150mm]
B_3_30_20_N	Bidirectional	3	300	200	none
B_3_30_20_S	Bidirectional	3	300	200	spike [2]
B_3_30_20_W	Bidirectional	3	300	200	wrap [150mm]

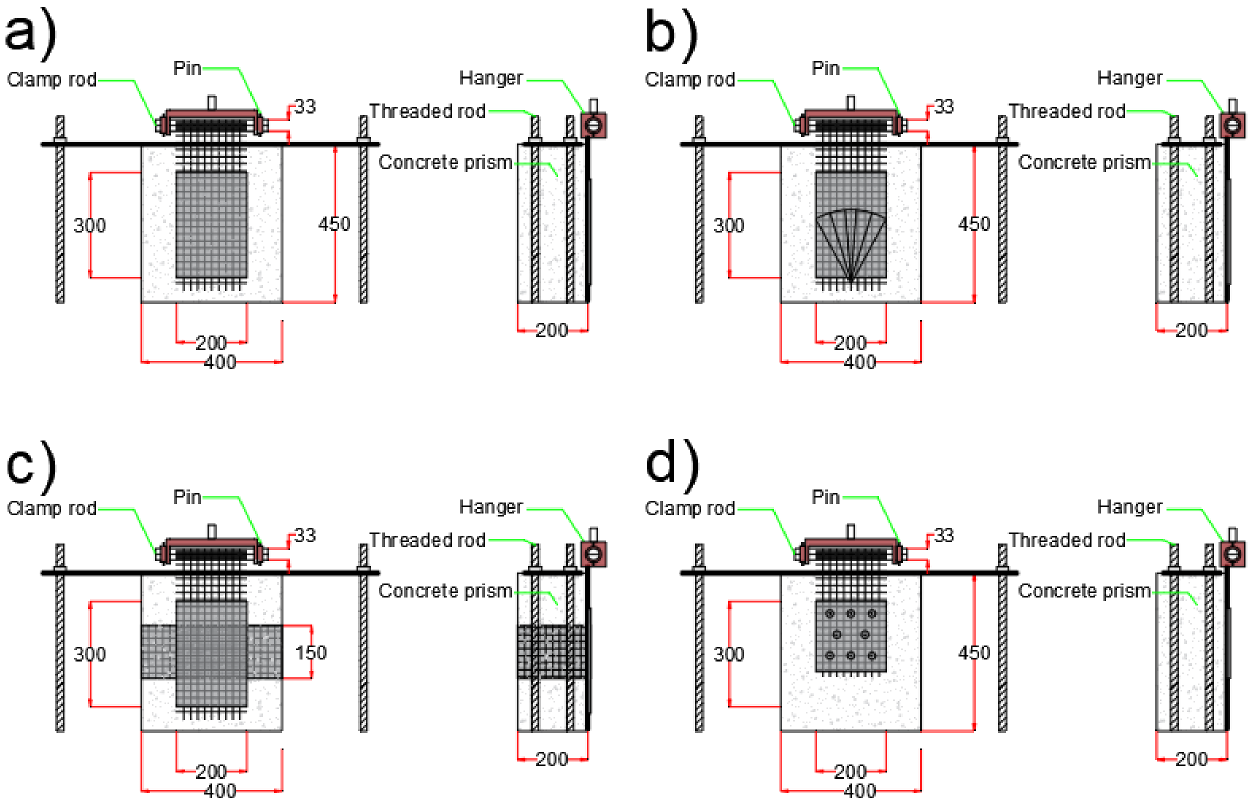

Figure 3.2: Layout and geometry of specimens U_1_30_20_N (a), U_1_30_20_S (b), U_1_30_20_W (c) and U_1_20_20_M in mm

3.3 Fabrication of test specimens and material properties

High strength concrete was used to cast the concrete prisms which represents the substrate. Three 100 mm cylinders were sampled from the mix to measure the strength in accordance with ASTM C31. The cylinders were wet cured and the 28th day compressive strength of the cylinders was tested in accordance with ASTM C39. The average compressive strength of the prisms was found to be 53 MPa.

CSS-CM is a shrinkage-compensated, polypropylene-fibre reinforced cementitious matrix designed specifically for FRCM composites. The unit weight of the cementitious matrix is 2240 kg/m^3 and the 28-day compressive strength is 52 MPa, as reported by the manufacturer. Three mortar cube samples were collected from each batch while creating composite samples, following ASTM C109, to compare the actual 28-day compressive strength of the cementitious matrix with the manufacturer's published data, and to ensure good quality control for proper sample comparison. Test results of the 28-day compressive strength of the mortar cubes are summarized in Table 3.3. The average 28-day compressive strength of the cementitious matrix was 48.4 MPa.

Table 3.3: Mechanical properties of used materials

Material	Reported ultimate tensile strength (MPa)	Experimental ultimate tensile strength (MPa)	Reported ultimate tensile strain (%)	28-day compressive strength (MPa)	Cracked Tensile Modulus (MPa)
Concrete prisms	-	-	-	53	-
Cementitious matrix	-	-	-	48.4	-
Unidirectional carbon fabric	2866	-	1.5	-	-
Bidirectional carbon fabric	3136	-	1.5	-	-
Cured composite with unidirectional fabric	885	791	1.1	-	49000
Cured composite with bidirectional fabric	986	882	1.1	-	48300
Carbon spike anchors	4600	-	1.9	-	98000

Although both unidirectional and bidirectional carbon fabrics used in this study share the same ultimate tensile strain of 1.5% at failure, the ultimate tensile strength of the bidirectional and the unidirectional fabrics is 3136 MPa and 2866 MPa, respectively as reported by the manufacturer. Tensile tests were conducted in another study by Asgharigharakheili (2022) on the same materials used for this experiment. The strength was reported to be 791 MPa and 882 MPa for cured composite with unidirectional fabric and bidirectional fabric, respectively.

The carbon FRP spike anchor used has a higher ultimate tensile strength compared to carbon fabric at 4600 MPa, and a higher strain capacity of 1.9%. The spike anchor was designed to ensure that the failure would happen within the FRCM composite itself rather than the anchor. All material properties are summarized in Table 3.3.

Eight 10 mm-long strain gauges were used for each specimen, which were bonded directly to the carbon grid prior to installation. Four strain gauges were installed on a single strand at 6.6 cm from each side of the FRCM as shown in Figure 3.3. This was done so that the average can be calculated in order to reduce the effect of eccentricity. The first strain gauge was installed at a depth of 2 cm from the top (loaded) end of the FRCM for the 20 cm-long specimens and at 3 cm for the 30 cm-long ones. The vertical spacing between the four strain gauges on each side was 5 cm and 8 cm for the 20 cm-long specimens and the 30 cm-long ones, respectively. Strain gauges were glued to the fabric using a special fast setting glue, and then were covered by polyurethane to protect the gauges from the cementitious matrix while applying the FRCM composite.

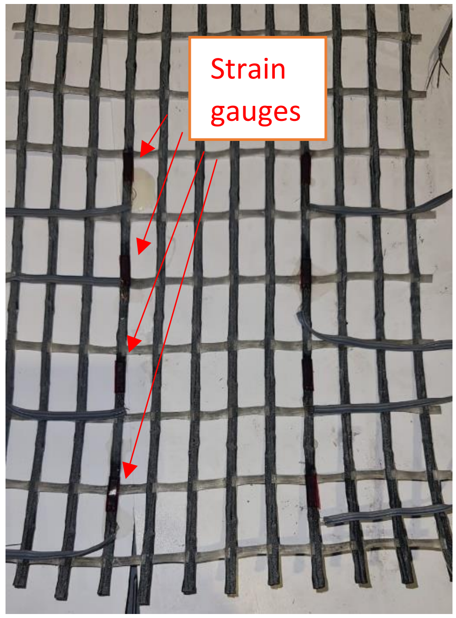

Figure 3.3: Eight strain gauges on a 20 cm-long specimen

The surface of the concrete prisms was prepared before mixing the cementitious matrix. The surface of each prism was crushed using a bush hammer to reach a minimum amplitude of 6 mm (0.25 in) or Concrete Surface Profile (CSP) 6-9 as recommended by the manufacturer as presented in Figure 3.4. Only one face of each prism was prepared for composite installation, except for wrap anchored specimens where all faces were roughened all around the prism in order to install the wrap anchor. All corners were rounded to a 19 mm (0.75 in) minimum radius using a grinder. After crushing the concrete surface and grinding the corners, compressed air was used to clean the surface of any debris and dust. Then, following the manufacturer's installation guide, all prepared surfaces were wetted to a Saturated Surface Dry (SSD) condition prior to FRCM application.

To mix the cementitious matrix, 90% of the total mixing water recommendation was added in the initial step. Based on the manufacturer's recommended range of water to be added, which was 2.7-3.2 L per 24.9 kg bag of cementitious matrix, a maximum water content of 3.2 L was chosen for the mix to reach the desired consistency and for the ease of application. The components were mixed with a mechanical mixer for 3 minutes, while adding the remaining 10% of the recommended total water until a homogeneous mixture with the desired consistency was formed. The mixture was left to rest for one minute and then remixed another 10 seconds before application.

Figure 3.4: Prism surface roughened to a CSP 9

To apply the non-anchored FRCM to each prism, a 10 mm-thick layer of the matrix was applied first. Then a fabric grid was set immediately into the wet cementitious matrix layer, followed with additional layers of carbon fabric grids, when required based on the number of layers determined for each specimen, set into other 10 mm layers of CSS-CM each. FRCM application was finished with a final 10 mm-thick layer of cementitious matrix trowelled to desired finish.

Application of wrap anchored specimens was exactly the same, except for an extra 150 mm wide layer applied on top of the FRCM and all the way around the prism. The overlap part was at the back of the prism and it was 200 mm long. This overlap length was chosen based on a study by Donnini et al. (2019) that showed the minimum overlap length for effective stress transfer between 2 fabrics in a FRCM composite to be 150 mm.

Preparation of the spike anchored specimens was a little different compared to the latter two types. A two-component epoxy resin was mixed in a clean mixing container and was paddled for approximately 5 minutes until uniformly blended. The fan part of the carbon spikes was anchored to the fabric grid using the epoxy resin and was left to cure for 72 hours prior to FRCM application. The fan part of the spike anchor was spread at a 45^{o} angle to cover the fabric strands after being embedded in epoxy while ensuring full fibre saturation was achieved. The prefabricated part was left dry to be anchored to the concrete prism later. Figure 3.5 displays the spike anchors during the installation process. After the epoxy resin cured, the FRCM was applied to the prism following the same procedure for non-anchored specimens. However, after the FRCM cured, a 12.7 mm (0.5 in) -wide, 100 mm -deep hole was drilled for each spike anchor. The edge of the hole opening was curved and smoothened to avoid stress concentrations. After cleaning them, the holes were filled with the same epoxy resin used for the fan section, and the prefabricated sand-coated section of the carbon spike anchor was inserted immediately afterwards.

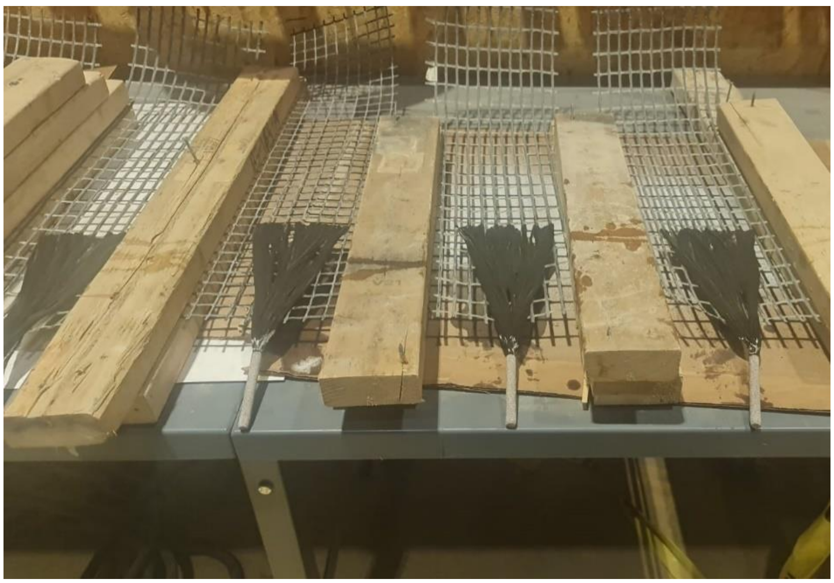

Figure 3.5: Carbon spike anchors installation

Finally, for the mechanically anchored specimens, FRCM was applied to the prisms following the same steps as the non-anchored specimens. After 5 days of FRCM application, 4.76 mm (3/16 in) holes were carefully drilled through the FRCM all the way into the prism with a total depth of 55 mm, approximately. Then, 50 mm-deep 3 mm-wide screws were installed to anchor the FRCM to the concrete prism. The 8 screws were distributed in a staggered formation at a 7 cm spacing, with washers that are 20 mm in diameter to ensure that the applied stresses increase the bond strength on the fabric/matric interface.

After the fabrication of the specimens was done, they were covered with a plastic drop sheet for 28 days to maintain the moisture, and were watered regularly to avoid shrinkage cracks and to ensure proper curing of the FRCM.

The last step of specimen preparation before testing was spray painting. To create a speckle pattern for the DIC, a flat white paint was sprayed on top of the FRCM covering the whole surface of the specimen. Then a flat black paint was sprayed on top creating small random dots or a speckle pattern. These two colors were chosen in order to create a contrast to make it easier for the software to recognize the dots and follow the deformation. Two pieces of white paper tape were attached, from both sides of the specimen, and were sprayed with a random speckle pattern to be tracked using the software to record the global displacement (i.e., slip) of the fabric as illustrated in Figure 3.6.

Figure 3.6: Tapes with speckle pattern to track global displacement

3.4 Test set-up and procedure

The test set-up was comprised of two main parts: a gripping assembly to pull the fabric and fix the prism in place, and a photography system to record the FRCM deformation for the DIC. A 190x600 mm steel plate was placed on top of the concrete prism and was fixed to the lower part of the tensile machine with four threaded bars to apply compression on the prism and pin it in place while pulling the fabric upwards. A new type of epoxy-less clamp was introduced for a faster and easier specimen set-up before every test. A 30 mm round bar was cut in half longitudinally to clamp the tip of the free fabric. The two parts of the bar were then bolted together to tighten the grip of the clamp. After that, the bar was rolled downwards 3 – 4 rolls while the fabric was rolling around the bar and overlapping. The bar was then attached to the upper lever of the tensile machine through a hanger, and 2 pins were used to prevent the bar from rolling back as illustrated in Figure 3.8. The bar was long enough to fit the width of the composite.

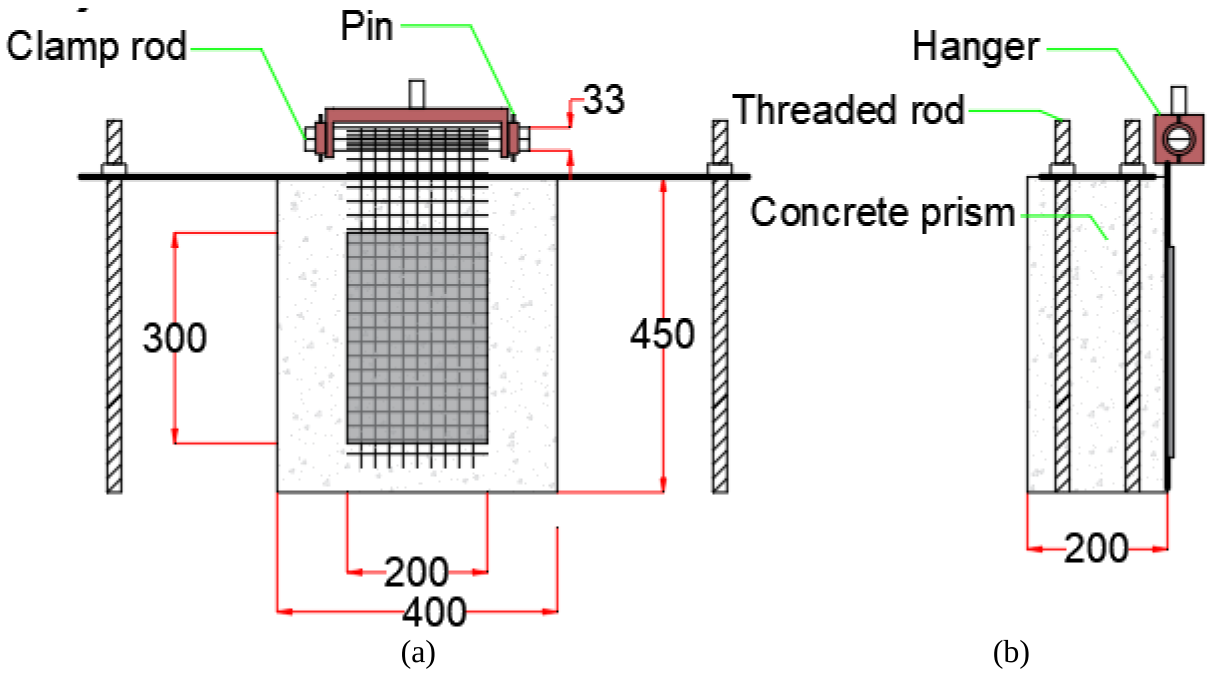

Figure 3.7: Front view schematic (a) and side view schematic of the gripping assembly (b)

The photography system consisted of three parts: lighting, an intervalometer, and a camera. The camera was a Canon DSLR EOS Rebel T5i mounted on a tripod at a distance of 4 m from the specimen, just enough to include the whole specimen into the frame. The lens used for the camera was a Canon EF 180mm f/3.5L Macro USM which is a medium telephoto lens with a focal length of 180 mm. The intervalometer was used to control the frequency of photo shooting and to prevent shaking the camera while the test is ongoing. In addition to the camera and the intervalometer, two 40 W LED lights were used to maintain consistent lighting and suitable brightness on the specimen while photo shooting was ongoing. Each LED light was mounted on a tripod 1 m away from the specimen. The photography system is shown in Figure 3.9.

Just before the start of each test, a photo of the specimen was taken and uploaded to the GOM Correlate software to assess the quality of the speckle pattern and adjust it as needed, which is the same software used to analyze the collected photos for the DIC. The intervalometer was set for a photo frequency of 1 Hz (1 photo/sec) which is compatible with the 0.5 mm/min displacement rate set for the experiment, which was adopted in other previous studies with similar test set-ups. Strain readings, applied load, and displacement of the test machine crosshead were recorded using a data acquisition system and a separate load cell.

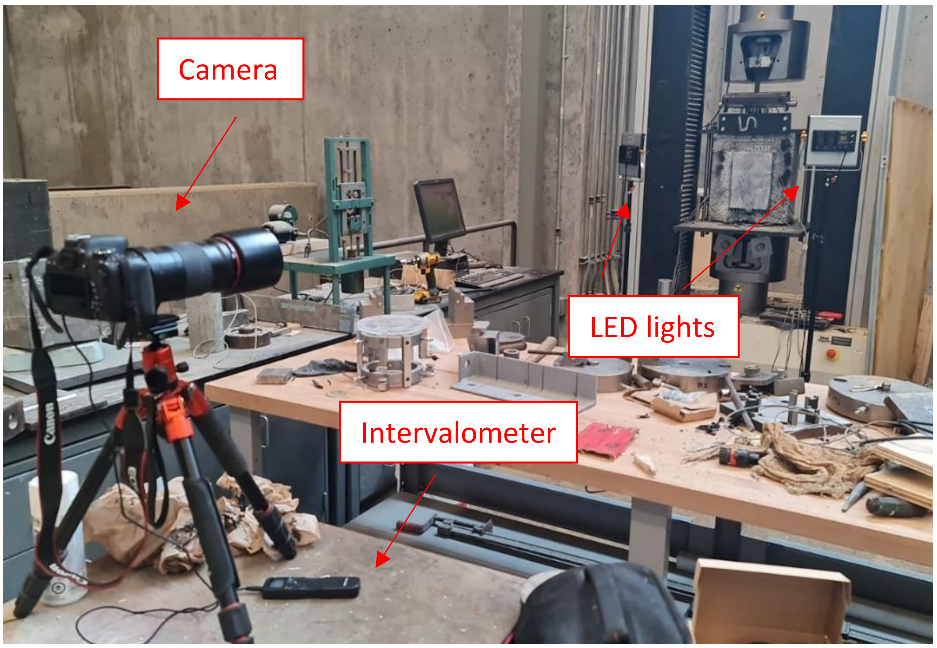

Figure 3.8: Photography system for DIC

4.0 Results

4.1 Overview

This study is conducted to better understand the behaviour of C-FRCM subjected to direct shear with varying number of C-FRCM layers and different anchorage configurations. Results of previous studies in the literature reported mostly composite debonding/slip at the fabric-matrix interface (Bournas et al., 2015; Trapko et al., 2015; Gonzalez-Libreros et al., 2017; Trapko &Musial, 2017; Aljazaeri et al., 2019; Marcinczak et al., 2019; Younis et al., 2017; Sneed et al., 2016) with very few reporting fabric rupture or composite debonding at the substrate-composite interface (Gonzalez-Libreros et al., 2017; Wakjira & Ebead, 2019). However, the failure mode observed the most across the specimens tested in this study was fabric rupture for reasons that are discussed in detail below. Table 4.1 summarizes the failure load, stress and failure modes of all specimens included in this study. The results of each test are presented in detail first, followed by a discussion of the effect of each key parameter in Chapter 5.

Table 4.1: Summary of test results

Specimen	Failure mode	Failure load (kN)	Average tensile stress in fabric at peak load (MPa)	Average bond stress at composite/substrate interface at peak load (MPa)
B_2_30_20_N	Rupture in the dry fabric	6.00	456.3	0.13
B_2_30_20_S1	Rupture in the dry fabric	6.13	348.2	0.10
B_2_30_20_W	Rupture in the dry fabric	9.21	523.1	0.15
B_3_30_20_N	Substrate/composite debonding	9.36	354.6	0.16
B_3_30_20_S2	Slip in some strands followed by rupture	17.91	678.3	0.30
B-3-30-20-W	Matrix cracking followed by rupture	9.61	364	0.16
U_1_20_20_M	Substrate/composite debonding	10.77	343.7	0.27
U_1_20_20_N	Substrate/composite debonding	5.26	168.0	0.13
U_1_20_20_S1	Rupture in the dry fabric	4.34	138.5	0.11
U_1_20_20_W	Rupture in the dry fabric	15.81	504.7	0.40
U_1_30_20_N	Slip in some strands followed by rupture	21.77	695.2	0.36
U-1-30-20-S1	Rupture in the dry fabric	10.71	341.9	0.18
U_2_20_20_N	Substrate/composite debonding	14.10	225.0	0.35
U_2_20_20_S1	Substrate/composite debonding followed by slip and then rupture	11.46	182.9	0.29
U_2_20_20_W	Rupture in the dry fabric	14.63	233.6	0.37
U_2_30_20_N	Substrate/composite debonding and matrix cracking	12.73	203.2	0.21
U_2_30_20_S1	Rupture in the dry fabric	9.21	147.0	0.15
U_2_30_20_W	Rupture in the dry fabric	14.77	235.8	0.25
U_3_20_20_N	Rupture in the dry fabric	18.71	199.2	0.47
U_3_20_20_S2	Slip of strands on both edges with matrix splitting and cracking followed by rupture	38.52	409.9	0.96
U_3_20_20_W	Rupture in the dry fabric	23.55	250.6	0.59
U_3_30_20_N	Fabric slip and rupture	29.55	314.5	0.49
U_3_30_20_S2	Rupture with spalling	29.18	310.6	0.49
U_3_30_20_W	Matrix cracking followed by rupture and slip	14.89	158.4	0.25

4.2 B_2_30_20_N

This specimen was fabricated using two non-anchored layers of bidirectional carbon fabric, with a composite length and width of 300 mm and 200 mm, respectively. During the test, no cracking nor delamination were observed on the composite. At the failure load, some of the fabric strands ruptured at various locations in both layers as shown in Figures 4.1a & 4.1b, although the experimental failure stress was lower than the theoretical one. The tensile stress in the fabric was 456.3 MPa at the peak load of 8.03 kN.

For the first half of the test as demonstrated in the load-slip curve shown in Figure 4.2, the tensile stress in the fabric increased at an increasing rate as the relaxed fabric was tightening around the grip. Then the stress increased linearly for the remainder of the test up to the maximum load, at which a brittle rupture took place. All load-slip curves were created using the global slip data collected from DIC of the tapes. The dotted line is extrapolated from the linear portion of the load-slip curve since the software lost track of the tapes in the late stages of the test. The maximum global slip was 2.4 mm and the slip initiated around 0.7 kN.

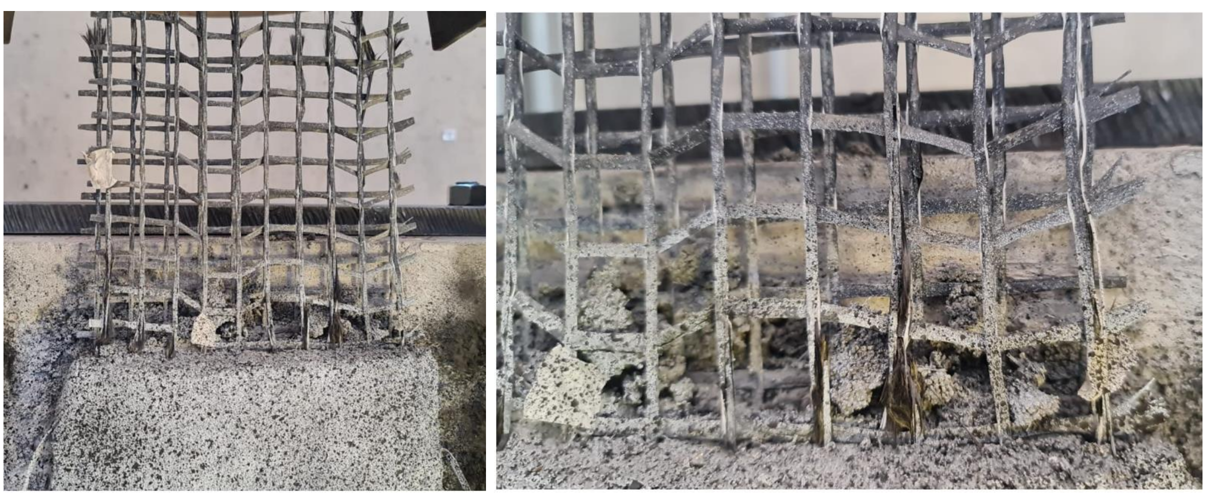

(a) (b)

Figure 4.1: ruptured fabric (a) and close-up of some ruptured strands (b)

The external surface strain profile obtained from the DIC of the specimen shows no noticeable strain nor cracking on the surface of the composite as the strain is almost 0% along the length as shown in Figure 4.3a. The strain profiles obtained using DIC correspond to the location of instrumented strands for a better comparison. This profile supports the visual observations. In comparison, the internal strain data acquired directly from the fabric inside the composite using strain gauges shown in Figure 4.3b is different.

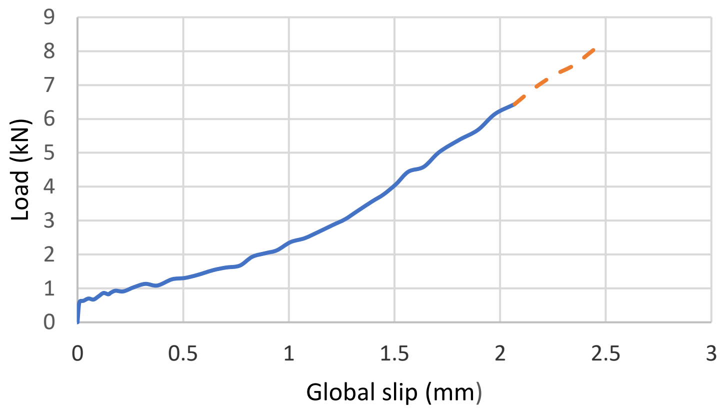

Figure 4.2: Load-slip curve obtained using DIC

At 5 kN load, internal fabric strain was measured to be 0.19% at a depth of 30 mm from the loaded end of the composite, and no strain was detected deeper than that along the specimen. The strain experienced a jump to 1.03% at a load of 6 kN, which is close to the 1.5% rupture strain of the fabric as specified by the manufacturer. The dissimilar fabric and matrix strains suggest slip. No strain data was recorded after reaching 6 kN load as some of the strands ruptured and redistributed the load to other parts of the fabric. The strain at 80 mm depth was negligible and no strain was detected at deeper strain gauges. In comparison to the strain calculated at the loaded end at 6 kN (0.71%), the strain measured using strain gauges at a depth of 30 mm is higher. This means that the stress in this strand was higher than the average across the strands which suggests the strands were not equally loaded. This is observed in other specimens and is discussed in more detail in the next chapter.

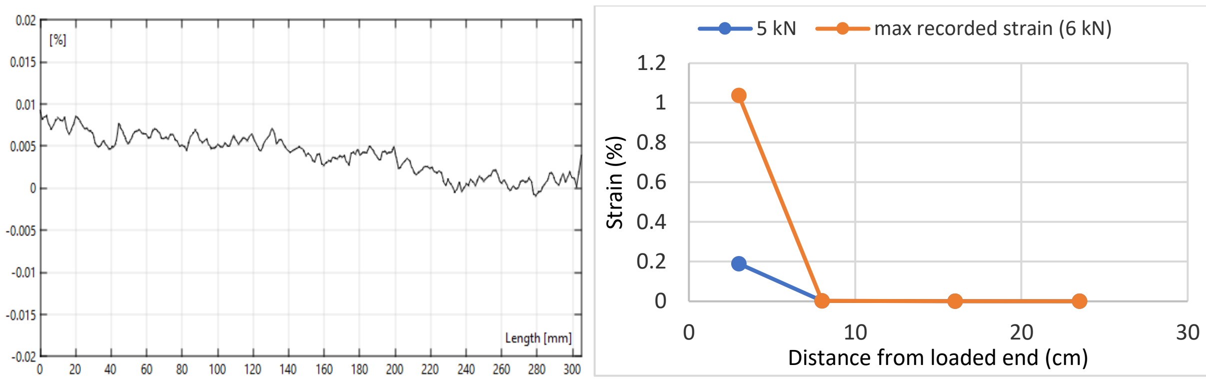

(a) (b)

Figure 4.3: strain profile obtained from DIC (a) and strain profile obtained from strain gauges (b)

The load-strain curve for every strain gauge is plotted in Figure 4.4. This curve shows that no noticeable strain was detected in the fabric within the composite until a load of 3 kN was reached, indicating that the fabric debonding had penetrated to a depth of 3 cm. The strain at a distance of 3 cm from the loaded end kept increasing with the load until some individual strands ruptured at 5.9 – 6 kN load. This rupture caused the load to be redistributed to other less loaded strands leading to a jump in the strain reading and eventually resulted in the strain gauge detaching from the fabric.

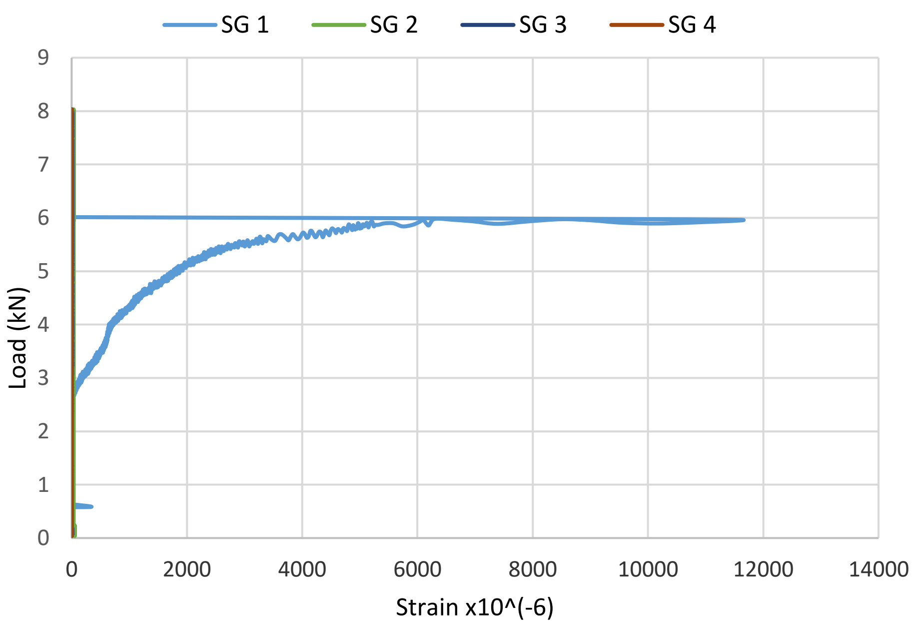

Figure 4.4: Load-strain curve for every strain gauge

4.3 B_2_30_20_S1

This specimen was fabricated using two layers of bidirectional carbon fabric, anchored using a carbon spike anchor, with a composite length and width of 300 mm and 200 mm, respectively. Similar to the previous specimen, no cracking nor delamination were observed on the composite. At the failure load, some of the fabric strands ruptured at both the composite loaded end and at the grip as can be seen in Figures 4.5a & 4.5b. Failure stress was significantly lower than the theoretical one. The failure stress of this specimen was 348.2 MPa at a load of 6.13 kN.

(a) (b)

Figure 4.5: front view of the fabric (a) and close-up to the ruptured strands (b)

The load-slip curve presented in Figure 4.6 shows a linear increase all the way to the rupture at the maximum load, which was brittle. The rate of stress increase was almost equal to that of specimen B_2_30_20_N which is expected as both specimens were created using the same fabric. The maximum global slip at failure was 1.2 mm and the slip initiated around 0.6 kN.

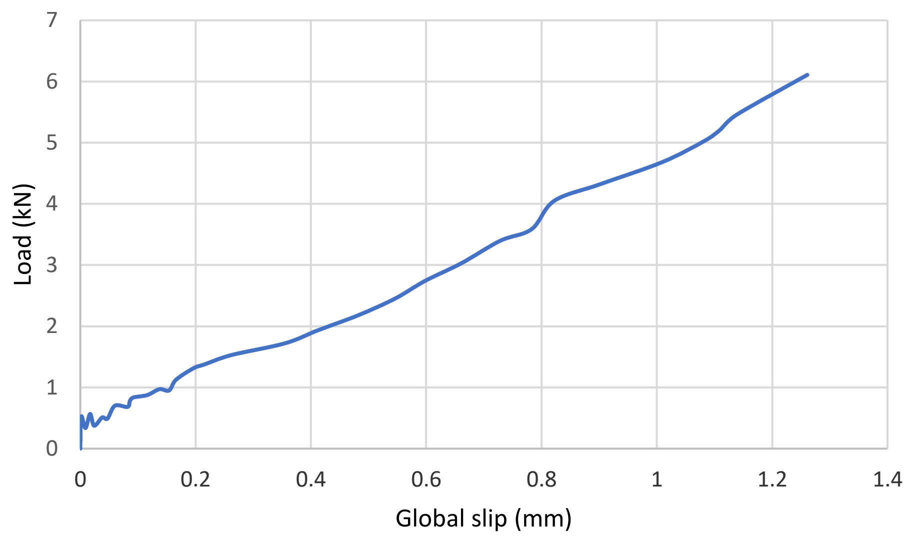

Figure 4.6: Load-slip curve obtained using DIC

The external strain profile obtained from the DIC of the specimen Figure 4.7a shows no noticeable strain nor cracking on most of the surface of the composite as the strain is almost 0% along the length except for the first 20 mm. The tensile strain was approximately 0.1% at the loaded end at the peak load which then decreases to 0% at a depth of 20 mm, suggesting some local strain concentration at the loaded edge of the composite. The internal strain data acquired directly from the fabric inside the composite using strain gauges, shown in Figure 4.7b, demonstrate more close strain values.

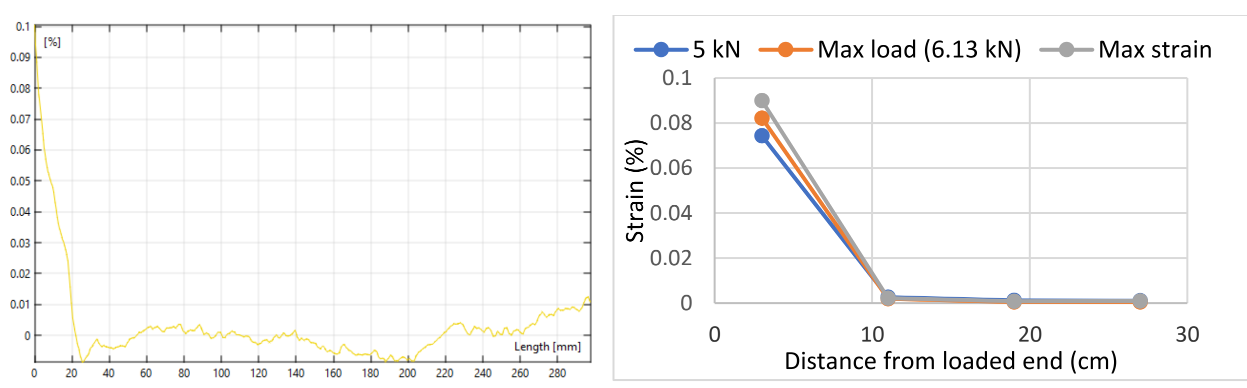

(a) (b)

Figure 4.7: strain profile obtained from DIC (a) and strain profile obtained from strain gauges (b)

At 5 kN load, strain was measured to be very low at 0.07%, 30 mm from the loaded end of the composite, and no strain was detected beyond 100 mm along the specimen. No significant change in the strain profile was observed at the maximum load (6.13 kN) nor at max strain. The strain at these two load checkpoints, 30 mm from the loaded end of the composite were 0.08% and 0.09%, respectively. The difference in the position of the internal and external strains (i.e., 30 mm for the fabric vs 0-20 mm for the matrix) may be due to shear lag which will be discussed in the next chapter.

The load-strain curve for every strain gauge is plotted in Figure 4.8. This curve shows that no noticeable strain was detected in the fabric until a load of 1.7 kN was reached. The strain kept increasing with the load until a rupture occurred at 6.13 kN load, which happened to the strands carrying the majority of the load. Although the fabric ruptured, the measured strain was low because the strands carrying most of the load were not the ones with the strain gauges.

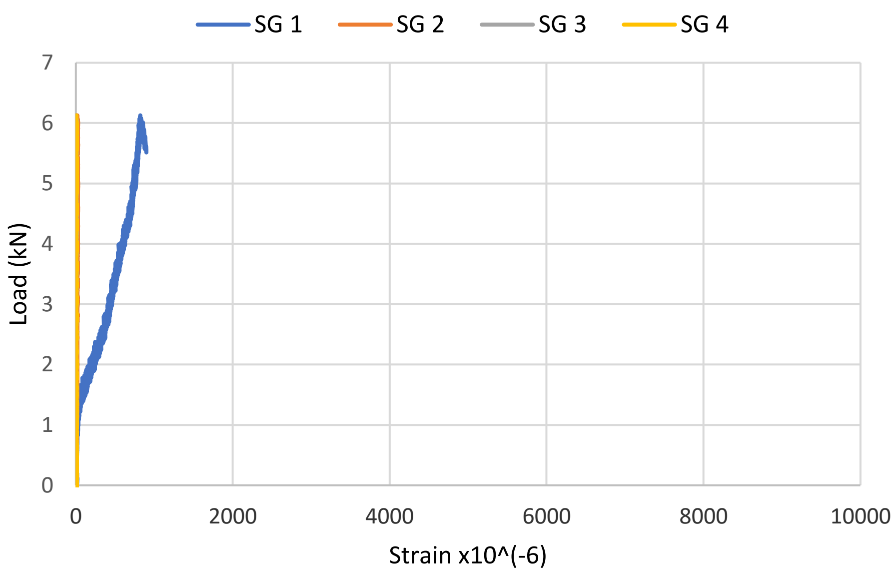

Figure 4.8: Load-strain curve for every strain gauge

4.4 B_2_30_20_W

This specimen was fabricated using two layers of bidirectional carbon fabric, anchored using a 15 cm-wide wrap anchor, with a composite length and width of 300 mm and 200 mm, respectively. Similar to the specimens B_2_30_20_N and B_2_30_20_S1, no cracking nor delamination were observed on the composite. At the failure load, some of the fabric strands ruptured at multiple parts of the fabric as can be seen in Figures 4.9a, 4.9b, 4.9c and 4.9d. Failure stress for this specimen was significantly lower than the theoretical one although it performed better than other bidirectional ones with two layers. First rupture of this specimen occurred at a load of 5.7 kN and the fabric started picking up the load again up to a stress of 523.1 MPa at a load of 9.2 kN.

The load-slip curve presented in Figure 4.10 shows a steady increase in the load as the measured global slip increased all the way to a load of 4.4 kN. More fabric strands that were not as loaded as the critical ones started picking up more load which increased the applied load rapidly until the dry fabric fully ruptured at 9.2 kN. The maximum global slip recorded for this specimen was 0.8 mm and it initiated at 0.3 kN.

(a) (b)

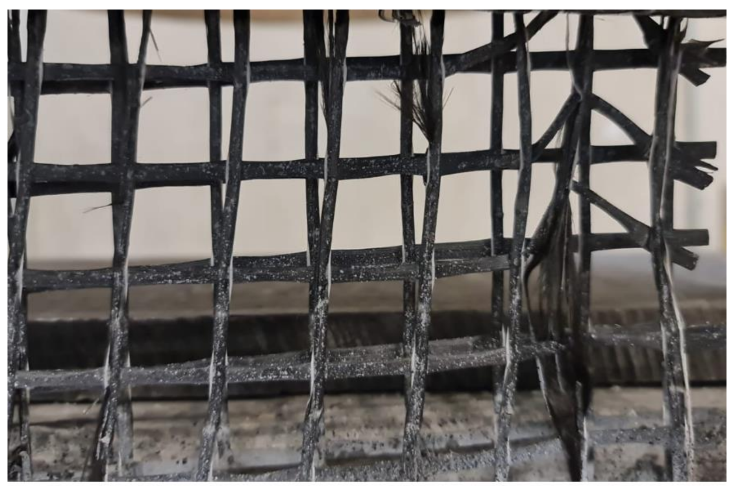

(c) (d)

Figure 4.9: (a), (b), (c) and (d) different spots of ruptured fabric

The external strain profile obtained from the DIC of the specimen is presented in Figure 4.11a. This strain profile shows no noticeable strain nor cracking on the surface of the composite just like the previous specimens, as the strain oscillates around 0% along the length except for the first 15 mm, where the tensile strain is 0.3% at the loaded end which then decreases all the way to 0% at a depth of 15 mm. This is due to the same reasons discussed earlier in addition to the round edge at the top of the composite which affects DIC results. The strain data collected directly from the fabric inside the composite using strain gauges shown in Figure 4.11b, demonstrate more noticeable strain values contrary to that of DIC. A strain profile is created for the 5 kN load checkpoint and at the maximum strain. No strain data is available beyond 5.7 kN as the strain gauges got damaged after that load.

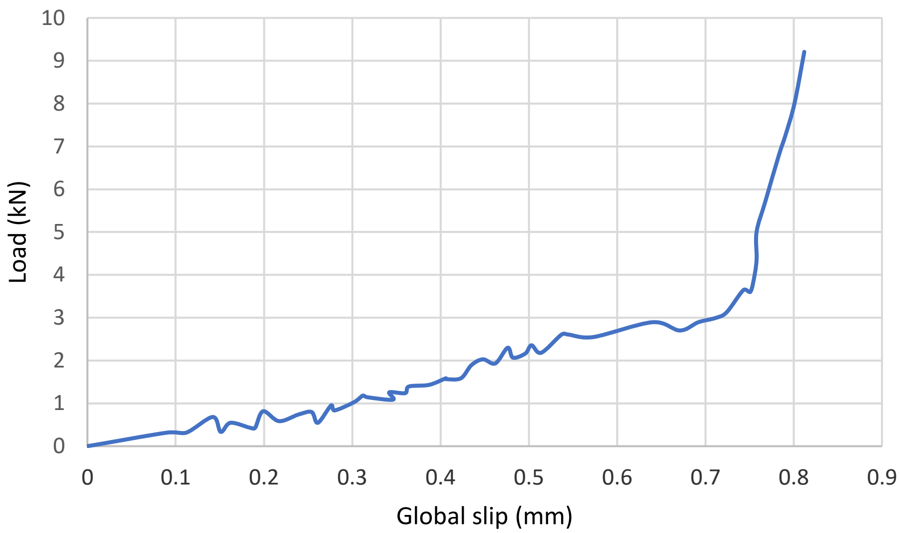

Figure 4.10: load-slip curve obtained using DIC

At 5 kN load, strain in the fabric strands was measured to be 0.5% at 30 mm from the loaded end of the composite, and no strain was detected beyond 110 mm along the specimen. The strain subsequently increased to 1.19% at a load of 5.7 kN at 30 mm from the loaded edge, which is the maximum recorded strain. No strain data is available after that load.

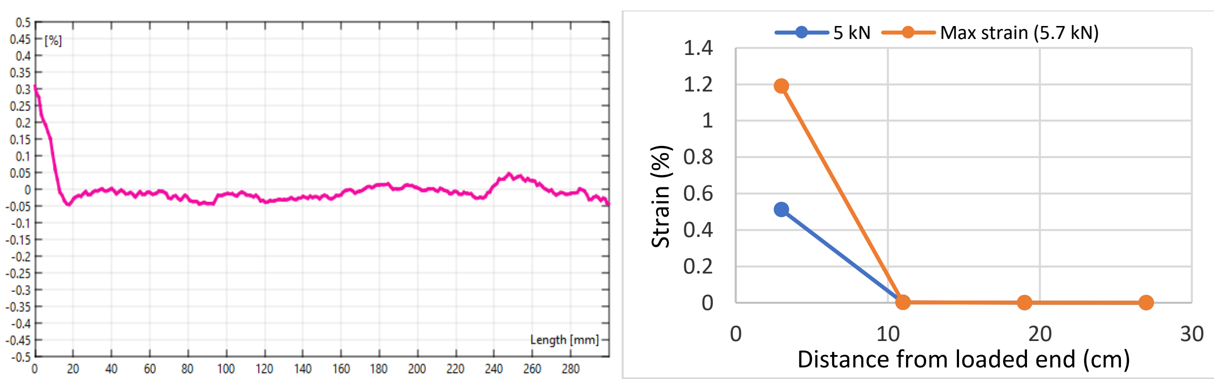

(a) (b)

Figure 4.11: strain profile obtained from DIC (a) and strain profile obtained from strain gauges (b)

The load-strain curve for every strain gauge is plotted in Figure 4.12. This curve shows that the strain starts to be observable at a load of 3.5 kN. The strain then increased rapidly to reach its maximum value when the load reached 5.7 kN. Other strain gauges did not detect any strain in the fabric at any load. The fabric strand with the strain gauges attached to it was clearly one of the strands carrying majority of the load before it ruptured.

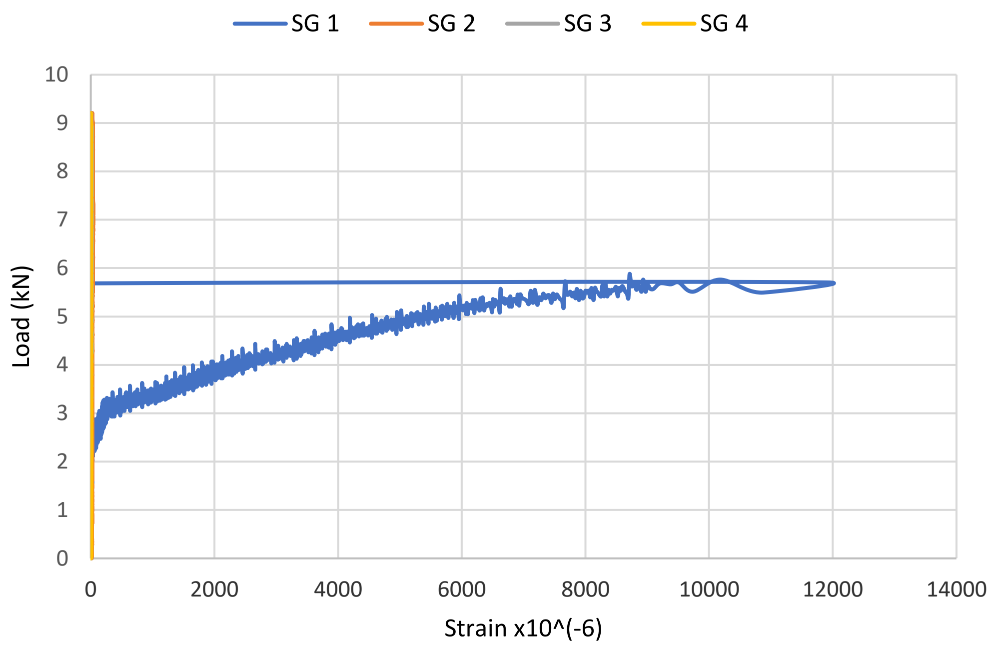

Figure 4.12: Load-strain curve for every strain gauge

4.5 B_3_30_20_N

This specimen was fabricated using three layers of non-anchored bidirectional carbon fabric, with a composite length and width of 300 mm and 200 mm, respectively. Similar to the previous specimen, no cracking nor delamination were observed on the composite. At the failure load, no damage was observed in the dry fabric nor on the composite surface. The composite fully debonded from the concrete block (the substrate), as shown in Figures 4.13a & 4.13b, in a brittle manner. The tensile stress at failure was 354.6 MPa in the fabric and the average composite-substrate bond stress was 0.16 MPa at the peak load of 9.36 kN.

(a) (b)

Figure 4.13: front view of the fabric (a) and close-up to the debonding surface (b)

The load-slip curve presented in Figure 4.14, shows a linear increase all the way to a load of 7.5 kN at a slip of 2 mm. The fabric then started picking up load at a significantly higher rate due to more strands being loaded as slip increased until the composite – substrate debonding occurred at a load of 9.36 kN and a maximum global slip of 2.04 mm and it initiated at 0.6 kN.

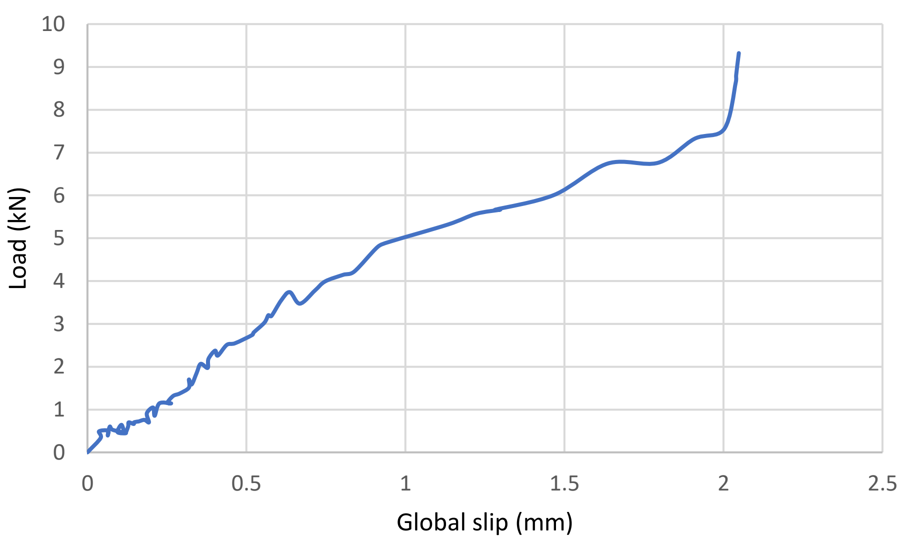

Figure 4.14: load-slip curve obtained using DIC

The external strain profile obtained from the DIC of the specimen Figure 4.15a shows no noticeable strain nor cracking on the surface of the composite as the strain is almost 0% along the length which supports the visual observations. In comparison, the strain data that was collected directly from the fabric inside the composite using strain gauges, shown in Figure 4.15b, show that the strain at 8.19 kN was at its maximum with a value of 0.79% 30 mm from the loaded end. Then it decreased to 0% at a distance of 110 mm from the loaded end. No significant strain was measured at a load of 5 kN. The strain at this load was measured to be 0.03% 30 mm from the loaded end with no strain below this point. No strain data is available beyond 8.19 kN load due to the strain gauges being damaged at that load.

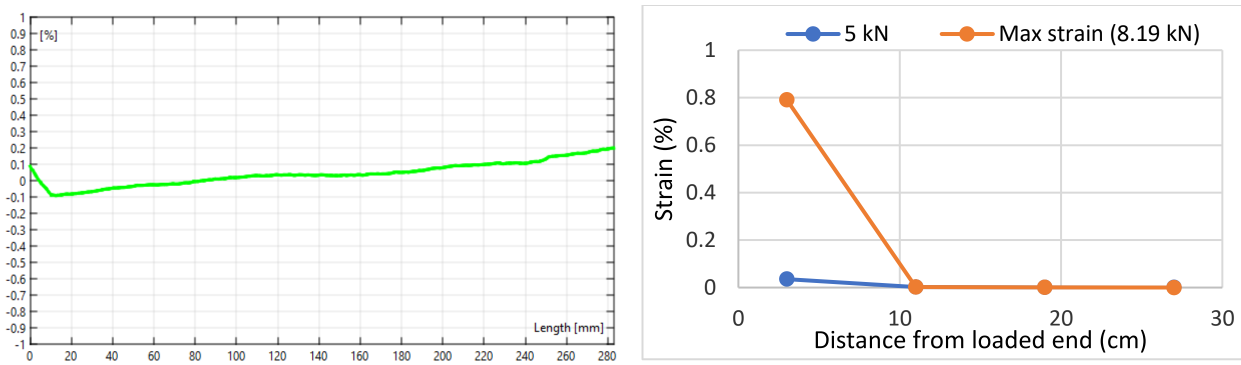

(a) (b)

Figure 4.15: strain profile obtained from DIC (a) and strain profile obtained from strain gauges (b)

The load-strain curve for every strain gauge is plotted in Figure 4.16. This curve shows that the strain starts to be observable at a load of 4.33 kN. The strain then increased significantly to reach the maximum at 8.19 kN. Other strain gauges did not detect any strain in the fabric at any load. Moreover, it can be seen that the strain gauge was damaged during the test at 8.19 kN before reaching the maximum load.

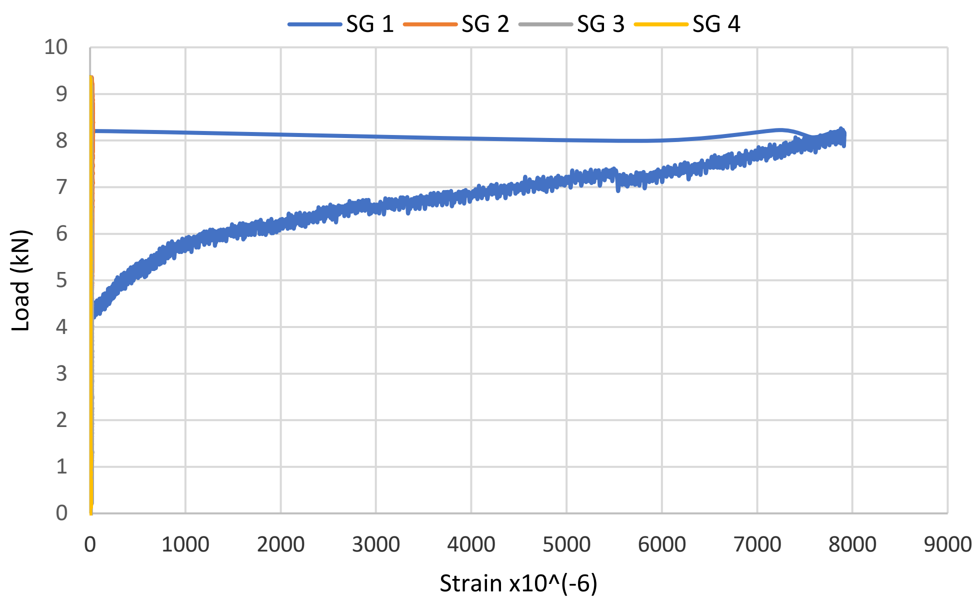

Figure 4.16: Load-strain curve for every strain gauge

The 2D strain map of this specimen created using DIC is presented in Figure 4.17. Just like the DIC generated strain profile, no significant strain is visible on the surface of the composite with the whole surface covered in green indicating 0% strain.

Figure 4.17: DIC generated 2D strain contour map

4.6 B_3_30_20_S2

This specimen was fabricated using three layers of bidirectional carbon fabric, anchored using 2 carbon spike anchors, with a composite length and width of 300 mm and 200 mm, respectively. Like all previous specimens, no cracking nor delamination were observed on the composite. However, slip was observed in this specimen during the test before the fabric ruptured. The slipped fabric strands were on both edges of the composite as shown in Figures 4.18a & 4.18b in addition to the ruptured fabric. The stress at the full rupture was 678.3 MPa in the fabric at a load of 17.9 kN which the highest among the specimens with bidirectional fabric.

(a) (b)

Figure 4.18: close-up to the right edge of the fabric (a) and close-up to the right edge of the fabric (b)

The load-slip curve for this specimen is shown in Figure 4.19. This specimen exemplifies the different behaviour of individual fabric strands due to unequal loading and different location of each strand. The increase of the load with respect to the slip was approximately linear until a load of 11 kN was reached at a global slip of 1.2 mm. The fabric strands then started slipping near the edges of the specimen before a major rupture took place at a load of 12 kN and a global slip of 1.4 mm. The load kept increasing while the fabric kept slipping at the edges until a second minor rupture followed shortly at a load of 15.6 kN. The final full rupture happened at a load of 17.9 kN and a global slip of 2.18 mm which initiated at 1.9 kN. Moreover, the fabric near the composite edges did not rupture.

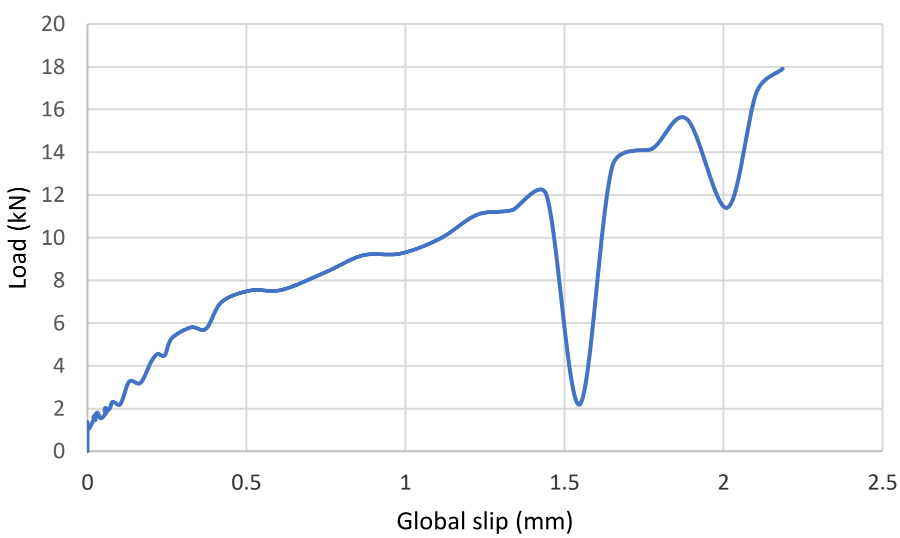

Figure 4.19: load-slip curve obtained using DIC

The external strain profile obtained from the DIC of the specimen as presented in Figure 4.20a shows no strain nor cracking on the surface of the composite as the strain is almost 0% along the length which correlates with the visual observations. On the other hand, the internal strain data that was collected directly from the fabric inside the composite using strain gauges shown in Figure 4.20b show that the strain at 8.8 kN was at its maximum with a value of 1%, 30 mm from the loaded end. Then it decreases back to 0% at a distance of 114 mm from the loaded end. The strain was measured to be much lower at a load of 5 kN. The strain at this load was measured to be 0.17%, 30 mm from the loaded end with no strain at any of the other strain gauges further from the loaded end of the composite. No strain data is available beyond 8.8 kN load because the strain gauge closest to the loaded end got damaged at that load.

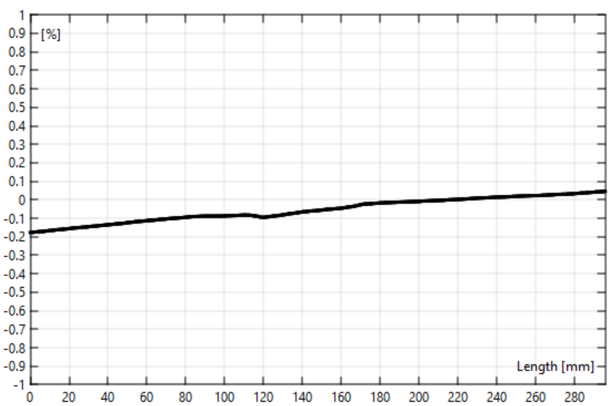

(a)

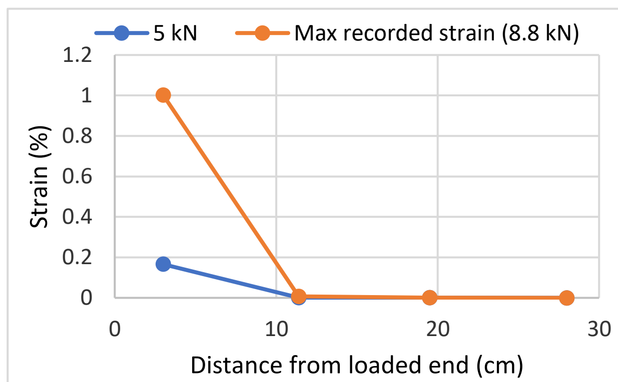

(b)

Figure 4.20: strain profile obtained from DIC (a) and strain profile obtained from strain gauges (b)

The load-strain curve for every strain gauge is plotted in Figure 4.21. This curve shows that the strain starts to be observable at a load of 2 kN. The strain then increased linearly with the load until a load distribution happened at 8 kN, where the strain jumped to reach the maximum recorded at 8.8 kN which is when the strain gauge got damaged shortly before the first major rupture. Other strain gauges did not detect any strain in the fabric at any load.

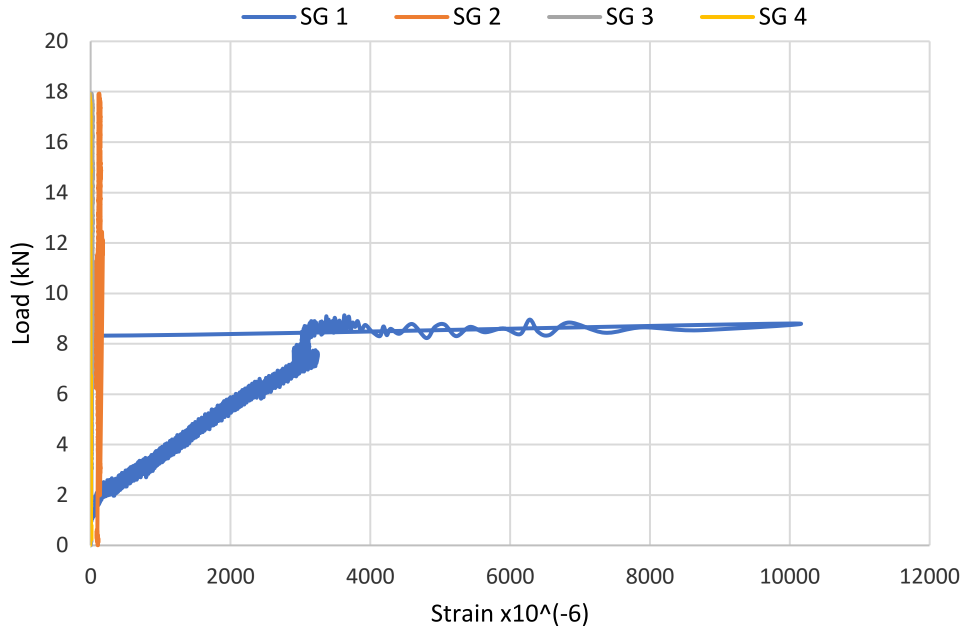

Figure 4.21: Load-strain curve for every strain gauge

The 2D strain map of this specimen created using DIC is shown in Figure 4.22. Similar to the DIC generated strain profile, no significant strain is visible on the surface of the composite with the whole surface covered in green indicating 0% strain. The excessive strain that can be seen at the corner of the specimen is not actual because the surface at this corner is tilted and not on the same plane of the DIC.

Figure 4.22: DIC generated 2D strain contour map

4.7 B_3_30_20_W

This specimen was fabricated using three layers of bidirectional carbon fabric, anchored using a wrap anchor, with a composite length and width of 300 mm and 200 mm, respectively. Unlike previous specimens, cracking was observed on the composite and fabric rupture at failure as can be seen in Figures 4.23a, 4.23b and 4.23c. Despite the matrix cracking and the fabric rupture, no visible fabric slip was observed during the test. The stress at the rupture was 364 MPa in the fabric at a load of 9.61 kN.

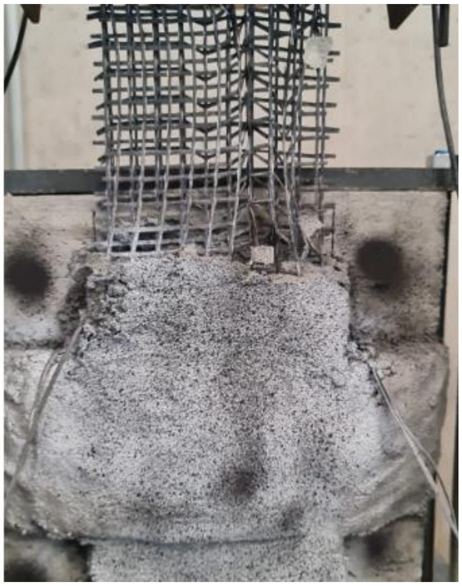

(a)

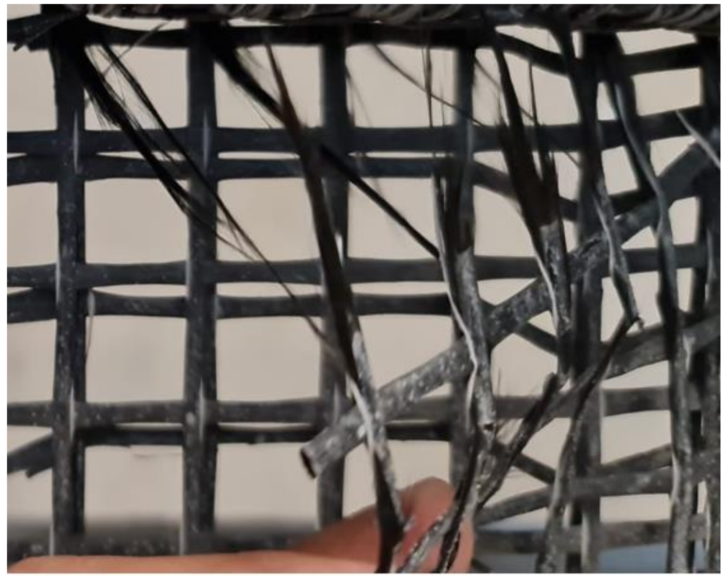

(b)

(c)

Figure 4.23: front view of the fabric (a), close-up to a ruptured fabric spot (b) and close-up to another ruptured fabric spot (c)

The load-slip curve presented in Figure 4.24 shows a linear increase in the load with respect to the global slip until a load of 3.6 kN is reached. The load then increased exponentially with respect to the slip until the fabric ruptured at 9.6 kN with a maximum global slip of 2.46 mm which initiated at 1.6 kN. Despite the change in the behaviour of the specimen at 3.6 kN, no cracking in the matrix nor fabric rupture were observed on the composite until the failure load was reached.

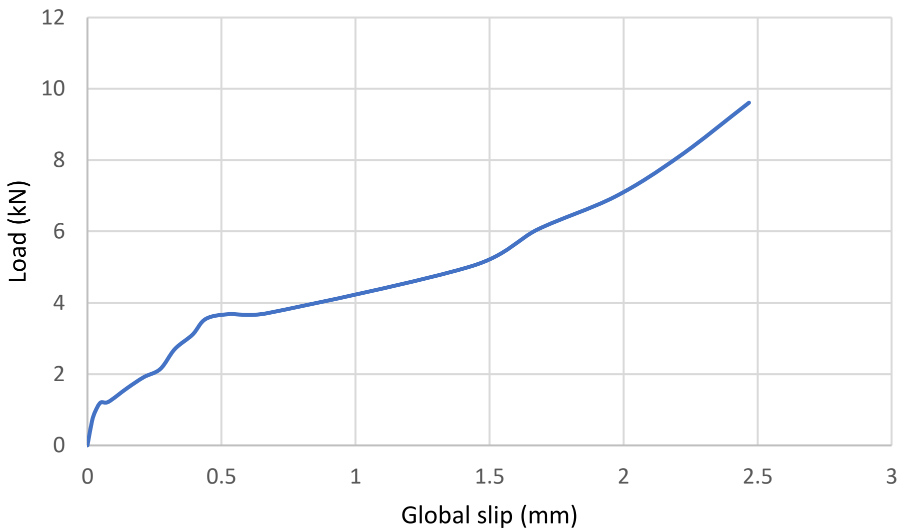

Figure 4.24: load-slip curve obtained using DIC

The external strain profile obtained from the DIC of the specimen as presented in Figure 4.25a shows two strain spikes after the full crack propagation at the loaded end of the specimen right on the edge and 20 mm deep. Beyond that, no cracking on the surface of the composite was detected, as the strain is almost 0% along the remaining length which correlates with the visual observations. The internal strain data that was collected directly from the fabric inside the composite using strain gauges, shown in Figure 4.25b, show that the strain at 9.5 kN was at its maximum with a value of 1.2%, 31 mm from the loaded end. Then it decreases back to 0% at a distance of 116 mm from the loaded end. The strain was measured to be significantly lower at a load of 5 kN. The strain at this load was measured to be 0.08%, 31 mm from the loaded end with no strain at any of the other strain gauges further from the loaded end of the composite. No strain data is available beyond 9.5 kN load due to the strain gauges being damaged at that load.

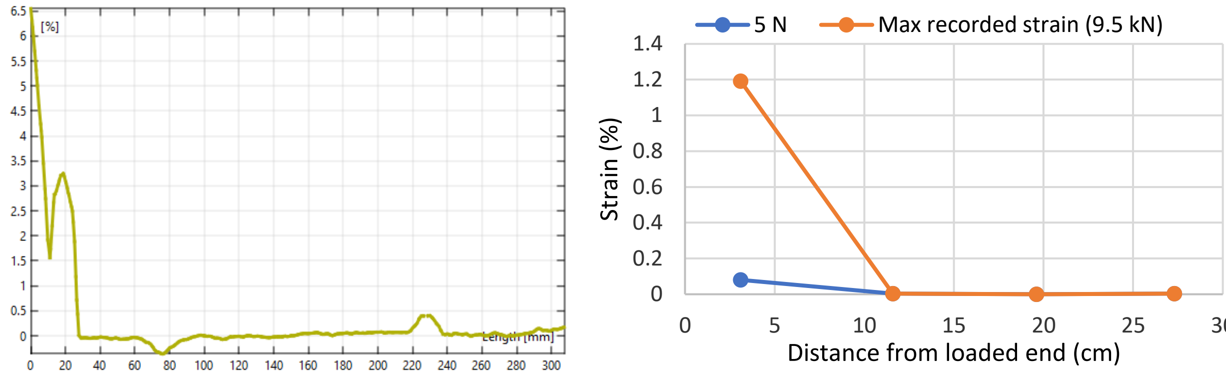

(a) (b)

Figure 4.25: strain profile obtained from DIC (a) and strain profile obtained from strain gauges (b)

The load-strain curve for every strain gauge is plotted in Figure 4.26. This curve shows that the strain starts to be noticeable at a load of 2.4 kN. The strain then increased linearly with the load until a load distribution happened at 8 kN, where the strain jumped to reach the maximum recorded at 9.61 kN which is when the strain gauge got damaged shortly before the first major rupture. Other strain gauges did not detect any strain in the fabric at any load.

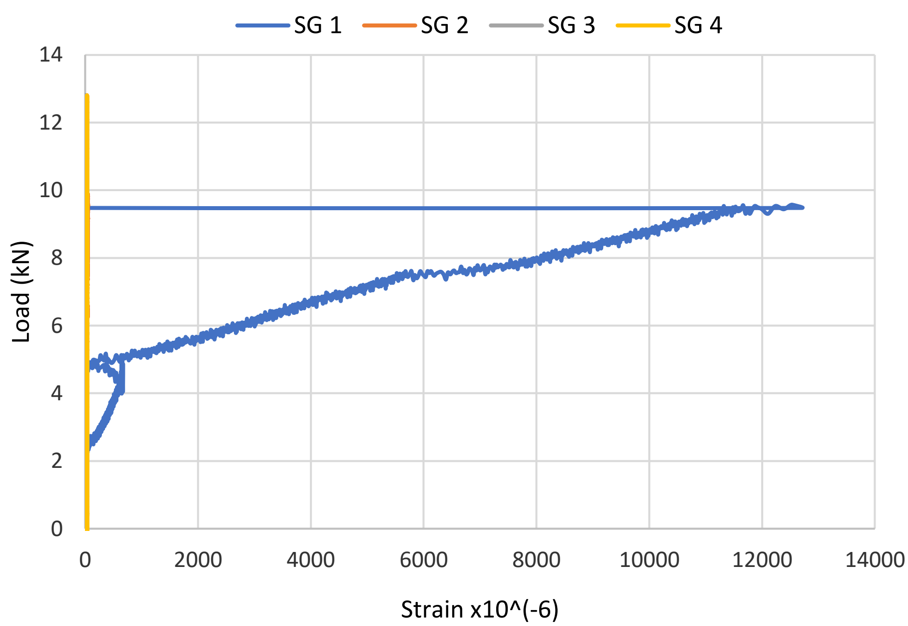

Figure 4.26: Load-strain curve for every strain gauge

The 2D strain map of this specimen created using DIC is displayed in Figure 4.27. Similar to the DIC generated strain profile, no significant strain is visible on the surface of the composite with the whole surface covered in green indicating 0% strain, except for the cracks at the top left part of the composite.

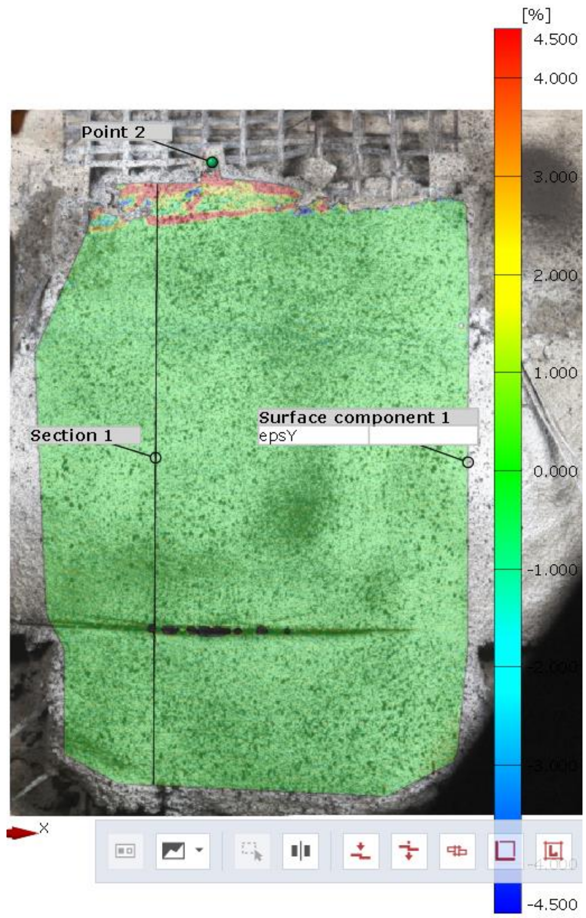

Figure 4.27: DIC generated 2D strain contour map

4.8 U_1_20_20_M

This specimen was fabricated using one layer of unidirectional carbon fabric, anchored using a mechanical anchor (screws), with a composite length and width of 200 mm. No cracking nor delamination were observed on the composite during the test. Moreover, no damage was observed on the dry fabric strands. The initial failure observed was the debonding at the composite – substrate interface while the screws were still attached to the concrete block. At the second failure, the screws were pulled out of the concrete block completely as shown in Figures 4.28a & 4.28b. Failure stress was significantly lower than the theoretical one. The failure stress of this specimen was 343.7 MPa at a load of 10.77 kN.

(a) (b)

Figure 4.28: front view of the fabric (a) and side view of the debonding surface (b)

The load-slip curve presented in Figure 4.29 shows a linear increase of the load with respect to the global slip all the way to the composite – substrate debonding at the maximum load, which was a brittle failure. The loading rate was slightly higher than that of other specimens with similar fabric behaviour like B_2_30_20_N and B_2_30_20_S1. Furthermore, the maximum global slip was 1.9 mm and it initiated at 0.5 kN.

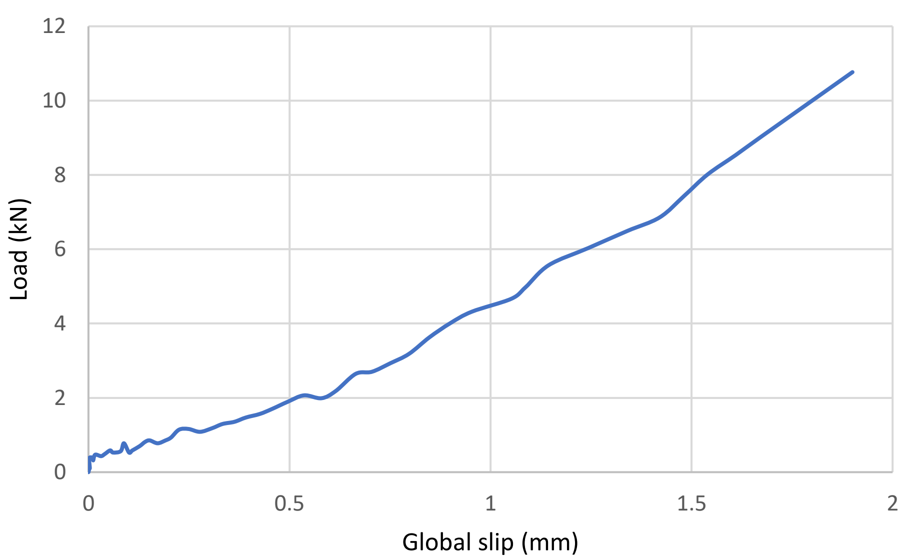

Figure 4.29: load-slip curve obtained using DIC

The external strain profile obtained from the DIC of the specimen Figure 4.30a shows no noticeable strain nor cracking on the surface of the composite as the strain is oscillating around 0% along the length except for four strain spikes. These strain spikes are a result of the curvature of the specimen at the top and bottom edges as well as the edge of the washer around one of the screws, since 2D DIC systems are not intended for curved surfaces. In comparison, the internal strain data acquired directly from the fabric inside the composite using strain gauges shown in Figure 4.30b demonstrate slightly more noticeable strain values. A strain profile is created for every 5 kN load interval to the maximum load, and at the maximum strain.

At 5 kN load, strain was measured to be very low at 0.06%, 20 mm from the loaded end of the composite, and no strain was detected beyond 70 mm along the specimen length. The strain then almost quadrupled at the maximum load (10.7 kN) and at the 10 kN load checkpoint although it was still low compared to the fabric capacity. The strain at these two load checkpoints, 20 mm from the loaded end of the composite were 0.23% and 0.21%, respectively.

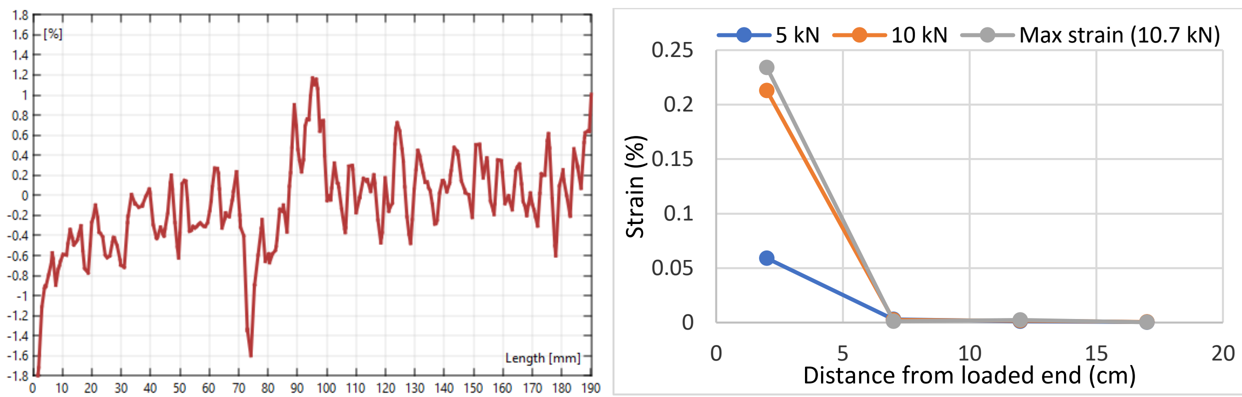

(a) (b)

Figure 4.30: strain profile obtained from DIC (a) and strain profile obtained from strain gauges (b)

The load-strain curve for every strain gauge is plotted in Figure 4.31. This curve shows a slight increase of the strain with the load in the fabric until the load reaches 3.5 kN. The strain then increases at a much faster rate all the way to a maximum strain of 0.23% at a load of 10.7 kN, which is when the debonding occurred. The fabric was unloaded as a result of the debonding and the strain decreased but started picking up again shortly until the screws were pulled out of the concrete block, at a load of 8.4 kN and a strain of 0.2%.

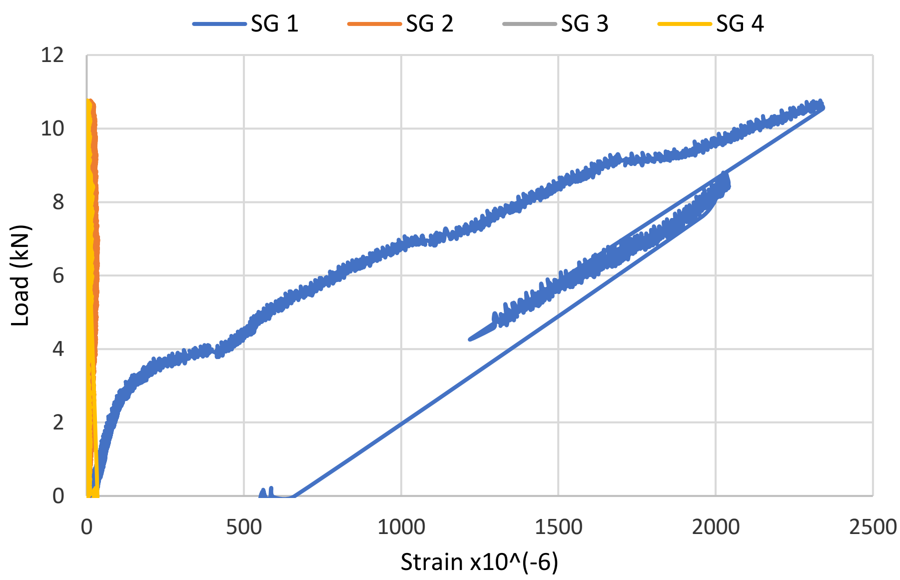

Figure 4.31: Load-strain curve for every strain gauge

The 2D strain map of this specimen created using DIC can be seen in Figure 4.32. Similar to the DIC generated strain profile, no significant strain is visible on the surface of the composite with the whole surface covered in green indicating 0% strain. This strain map illustrates how round edges out of the DIC plane are translated in the strain profile.

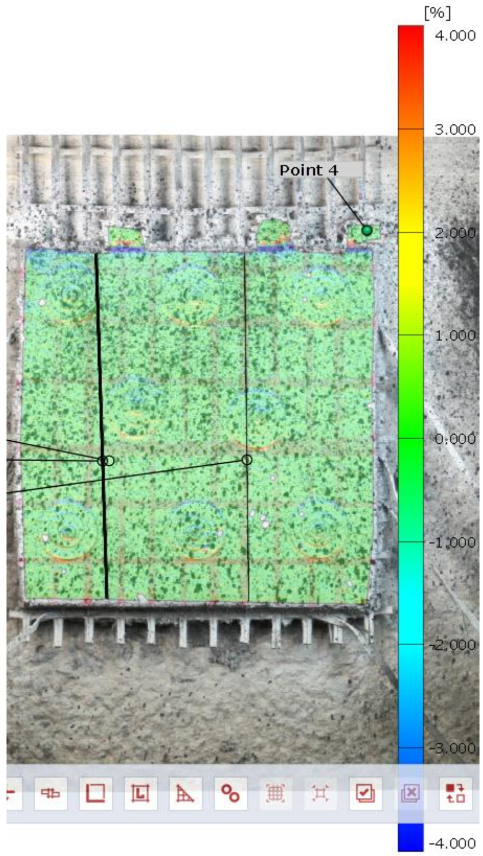

Figure 4.32: DIC generated 2D strain contour map

4.9 U_1_20_20_W

This specimen was fabricated using one layer of unidirectional carbon fabric, anchored using a wrap anchor, with a composite length and width of 200 mm. No cracking nor delamination were observed on the composite during the test. However, the fabric strands were worn out at various spots at the failure load before fully rupturing shortly as shown in Figure 4.33. This specimen presented the second highest stress in the fabric among the unidirectional specimens although failure stress was still lower than the theoretical one. The failure stress of this specimen was 504.7 MPa at a load of 15.81 kN.

Figure 4.33: ruptured fabric

The load-slip curve presented in Figure 4.34 shows a linear increase of the load with respect to the global slip until the fabric started wearing out at a load of 14.8 kN and a global slip of 0.57 mm, after which the load dropped slightly. The load kept increasing briefly at a lower rate until full rupture occurred at 15.8 kN at a slip of 0.76 mm which initiated at 1.0 kN.

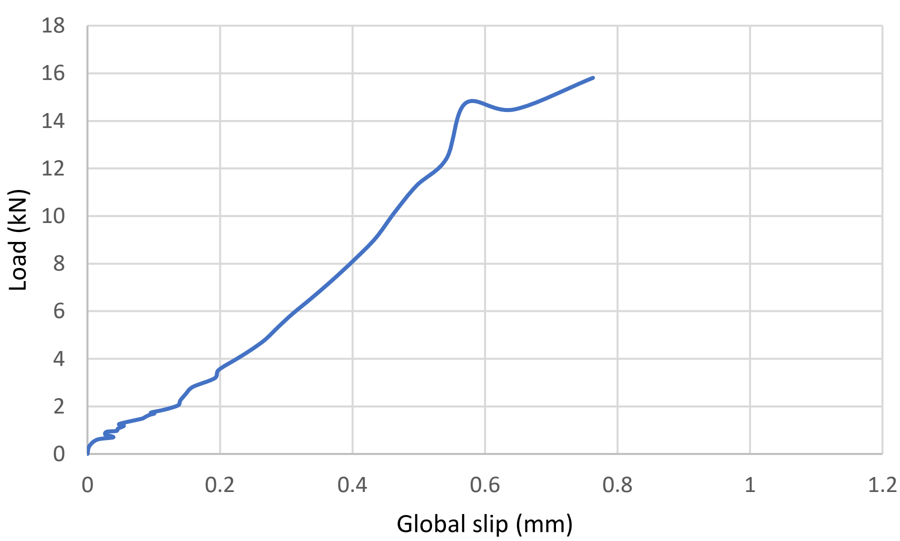

Figure 4.34: load-slip curve obtained using DIC

Unfortunately, no strain profile could be obtained using DIC due to a software related issue during the analysis. Strain data acquired directly from the fabric is still available with the strain gauges. A strain profile was created for every 5 kN load interval to the maximum load, and at the maximum strain as shown in Figure 4.35.

At 5 kN load, strain was measured to be very low at 0.04%, 20 mm from the loaded end of the composite, and no strain was detected beyond 70 mm along the specimen. The strain increased at the 10 kN load checkpoint although it was still as low as 0.28% at a depth of 20 mm, with no strain beyond 70 mm. The strain at 15 kN and 15.6 kN were measured to be 0.92% and 0.93% at a depth of 20 mm from the loaded end, respectively. Moreover, the strain at those last two load points was measured to be 0.03% at a depth of 70 mm from the loaded end and almost no strain beyond 120 mm.

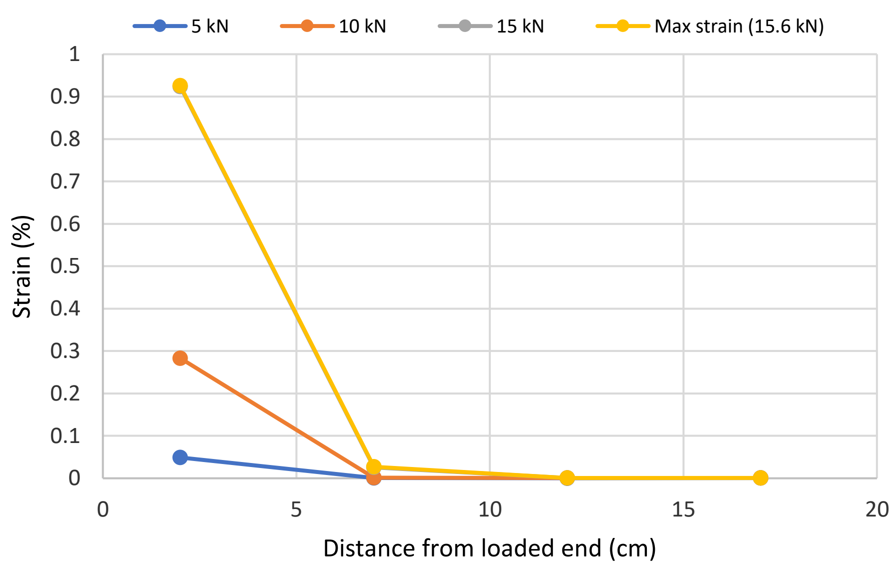

Figure 4.35: strain profile obtained from strain gauges

The load-strain curve for every strain gauge is plotted in Figure 4.36. This curve shows that the strain rose at an increasing rate with respect to the load until the fabric initially started wearing out at a strain of 0.88% at a load of 14.8 kN as recorded by strain gauge 1, and fully ruptured at a strain and a load of 0.93% and 15.8 kN, respectively. Other strain gauges did not record any significant strain.

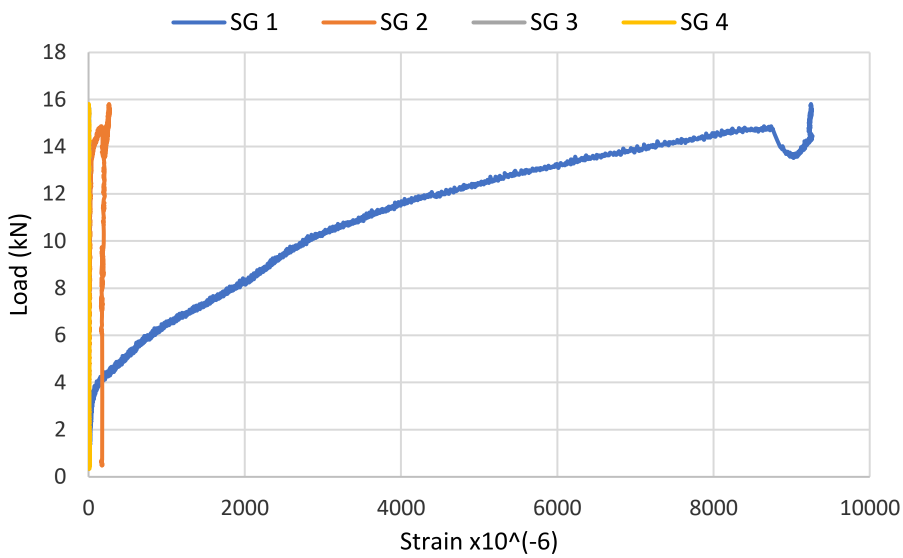

Figure 4.36: Load-strain curve for every strain gauge

The 2D strain map of this specimen created using DIC is presented in Figure 4.37. This supports the visual observations as there is no significant strain on the surface of the composite with the whole surface covered in green indicating 0% strain.

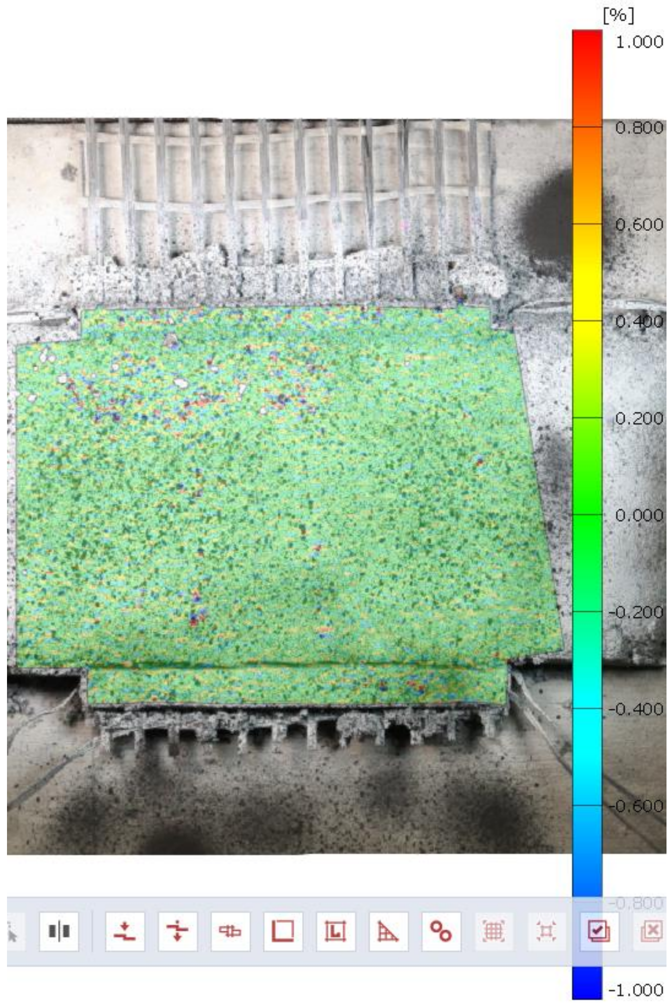

Figure 4.37: DIC generated 2D strain contour map

4.10 U_1_30_20_N

This specimen was fabricated using one layer of non-anchored unidirectional carbon fabric, with a composite length and width of 300 mm and 200 mm, respectively. No cracking nor delamination were observed on the composite surface during the test. However, the fabric strands ruptured at two different locations: the first rupture happened at the top edge of the composite and the second was at the opposite edge at the rod part of the test setup as seen in Figure 4.38. This specimen showed the highest stress at failure in the fabric among all specimens although failure stress was still lower than the expected theoretical one. The failure stress of this specimen was 504.7 MPa at a load of 15.81 kN.

(a) (b)

Figure 4.38: fabric rupture near the composite edge (a) and fabric rupture near the grip (b)

Due to a malfunction with the strain gauges on this specimen, no strain profile could be created other than that of the DIC. Unfortunately, the load slip curve also could not be obtained because the software failed to track the tape movement.

The strain profile obtained from the DIC of the specimen as shown in Figure 4.39 shows no noticeable strain nor cracking on the surface of the composite as the strain is almost 0% along the length except for the top edge of the specimen, which is a result of the out of plane curvature of the specimen at the top edge.

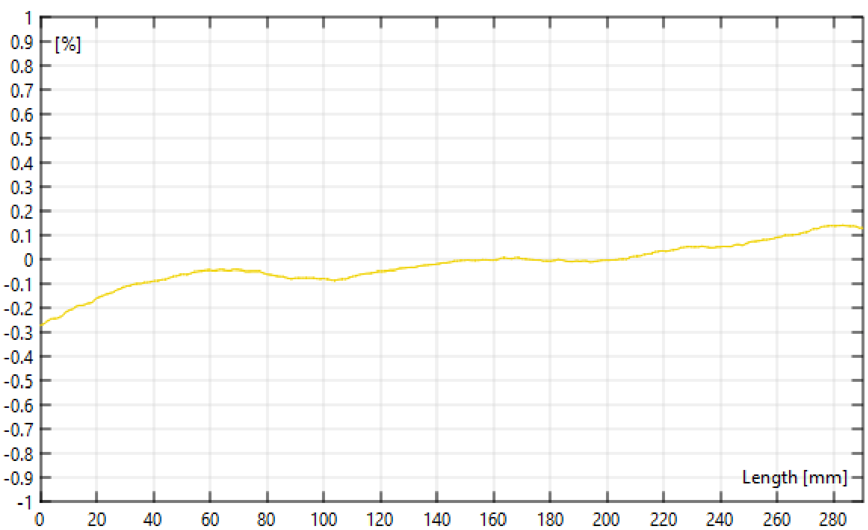

Figure 4.39: surface strain profile obtained from DIC

The 2D strain map of this specimen created using DIC is displayed in Figure 4.40. It matches the strain profile as there is no significant strain on the surface of the composite with the whole surface covered in green indicating 0% strain.

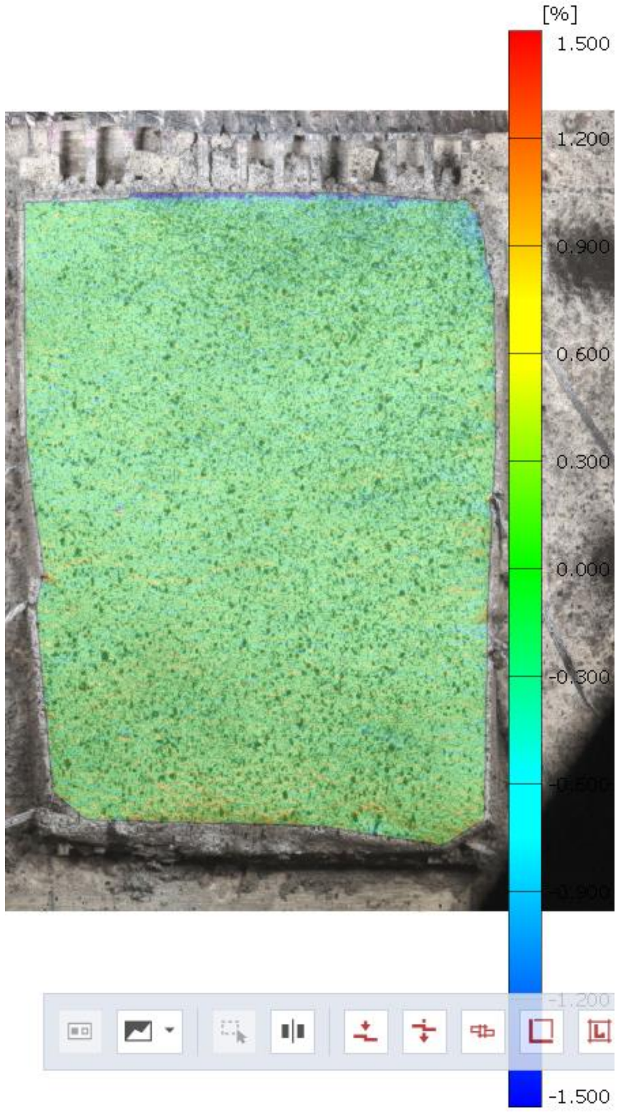

Figure 4.40: DIC generated 2D strain contour map

4.11 U_1_30_20_S1

This specimen was fabricated using one layer of unidirectional carbon fabric anchored using one spike anchor, with a composite length and width of 300 mm and 200 mm, respectively. No cracking nor delamination were observed on the composite surface during the test. However, the fabric strands near the edges ruptured at both sides of the fabric as presented in Figure 4.41. As most of the other specimens, the failure stress was significantly lower than the theoretical one. The failure stress of this specimen was 341.9 MPa at a load of 10.71 kN.

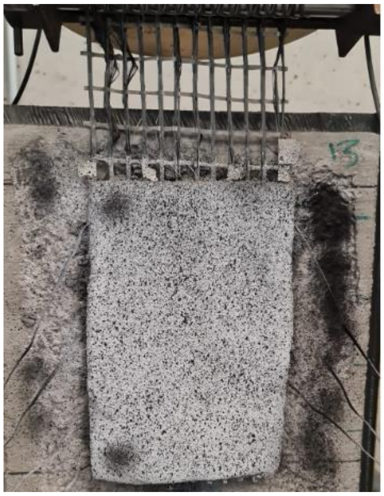

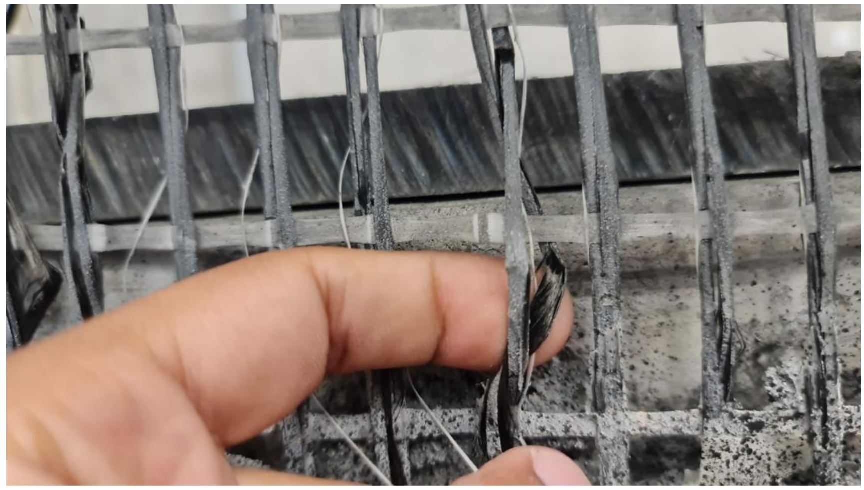

(a) (b)

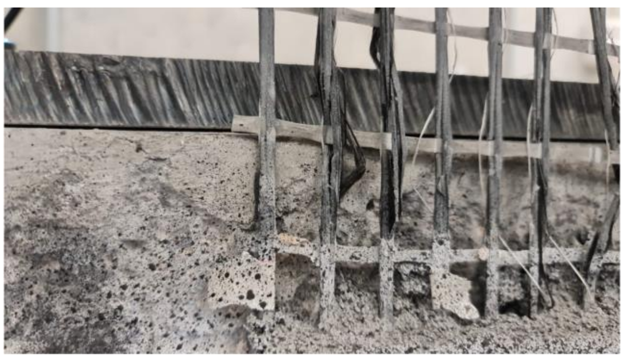

(c) (d)

Figure 4.41: front view (a), fabric rupture near the composite (b), fabric rupture near the edge (c), fabric rupture near the grip (d)

The load-slip curve presented in Figure 4.42 shows an exponential increase of the load with respect to the global slip up to approximately 10 kN when two fibre strands ruptured sequentially. The initial rupture occurred at a load of 10.4 kN followed by another major one at a load of 10.7 kN and a slip of 1.8 mm, after which the fabric could not recover and fully ruptured shortly thereafter at a slip of 2 mm which initiated at 0.4 kN.

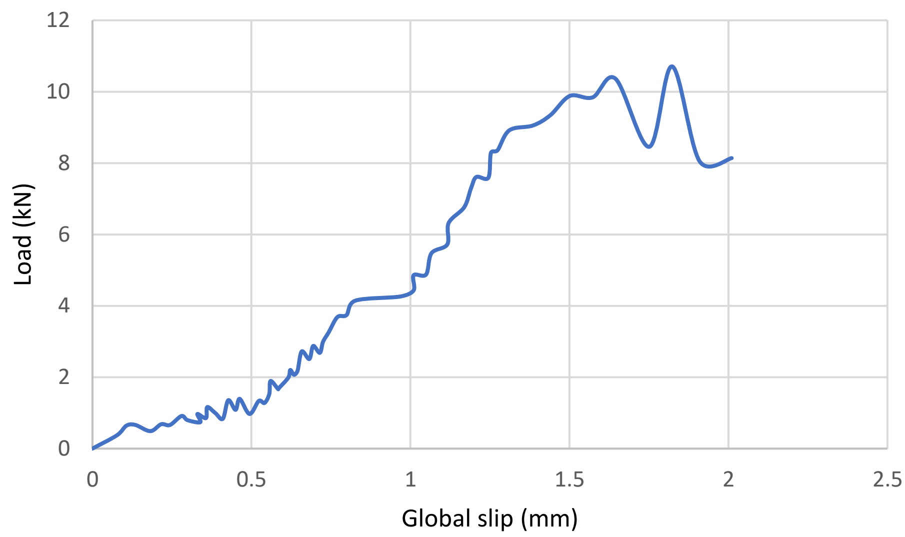

Figure 4.42: load-slip curve obtained using DIC

The external strain profile obtained from the DIC of the specimen seen in Figure 4.43a shows no noticeable strain nor cracking on the surface of the composite as the strain is approximately 0% along the length of the composite. In comparison, the strain data acquired directly from the fabric inside the composite using strain gauges shown in Figure 4.43b, demonstrate significantly more noticeable strain values. A strain profile is created for every 5 kN load interval to the maximum load, and at the maximum strain.

At 5 kN load, strain was measured to be very low at 0.04%, 30 mm from the loaded end of the composite, and no strain was detected beyond 117 mm along the specimen. The strain then jumped remarkably to reach the maximum of 0.92% at a load of 8.96 kN. Although the load kept increasing beyond this point, no strain data is available due to damaged strain gauges during the test. No noticeable strain was recorded beyond 117 mm from the loaded end at any load.

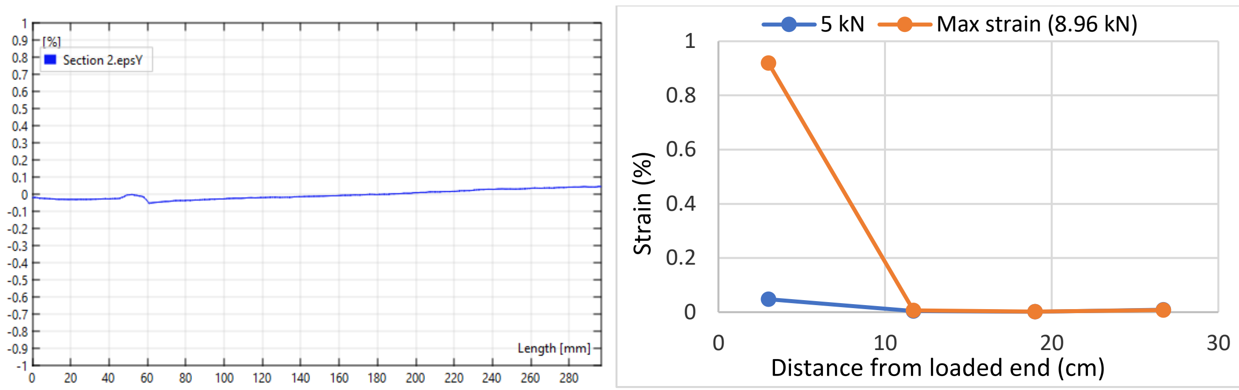

(a) (b)

Figure 4.43: surface strain profile obtained from DIC (a) and strain profile obtained from strain gauges (b)

The load-strain curve for every strain gauge is plotted in Figure 4.44. This curve indicates that the strain didn't start to become noticeable until a load of 4.1 kN is reached. The strain then increased rapidly to a maximum of 0.92% before Strain Gauge 1 got detached from the fabric during the test. Therefore, no strain data is available at this depth after 8.96 kN. Moreover, other strain gauges didn't record any strain at other depths.

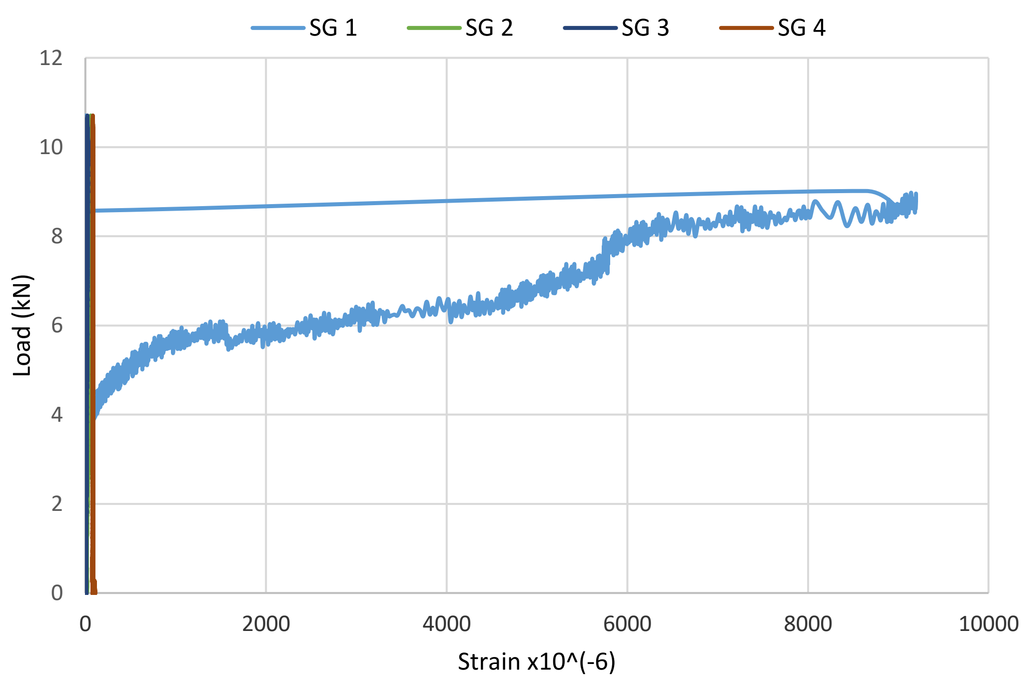

Figure 4.44: Load-strain curve for every strain gauge

The 2D strain map of this specimen created using DIC is shown in Figure 4.45. This map shows that there is no cracking or any significant strain on the surface of the composite with the whole surface covered in green indicating 0% strain.

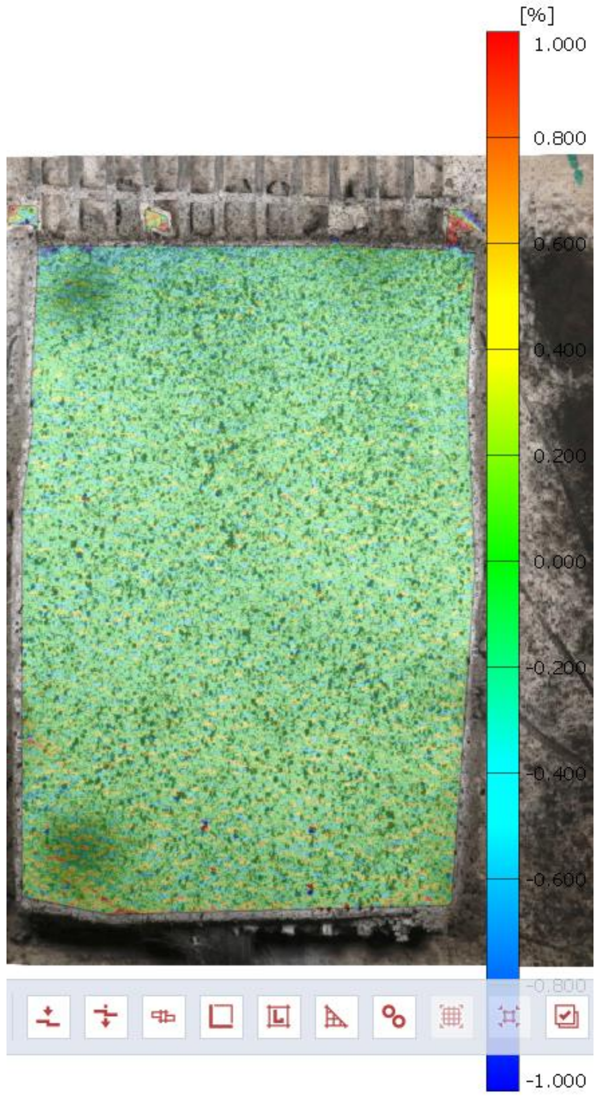

Figure 4.45: DIC generated 2D strain contour map

4.12 U_2_20_20_N

This specimen was fabricated using two layers of non-anchored unidirectional carbon fabric, with a composite length and width of 200 mm. No cracking nor delamination were observed on the composite surface before the composite-substrate debonding took place as shown in Figure 4.46. Moreover, the fabric strands did not rupture. This specimen did not perform well compared to other specimens as the failure stress was amongst the lowest. The failure stress of this specimen was 225 MPa in the fabric and 0.35 MPa at the composite-substrate interface at a load of 14.1 kN.

Figure 4.46: debonded composite

The load-slip curve presented in Figure 4.47, shows a linear increase of the load with respect to the global slip all the way to the composite – substrate debonding at the maximum load, which was a brittle failure. The maximum global slip was 1.9 mm at the failure load and it initiated at 1.0 kN. The strain gauges used for this specimen failed to record strains during the test which caused creating a strain profile and a load-strain plot to be unfeasible.

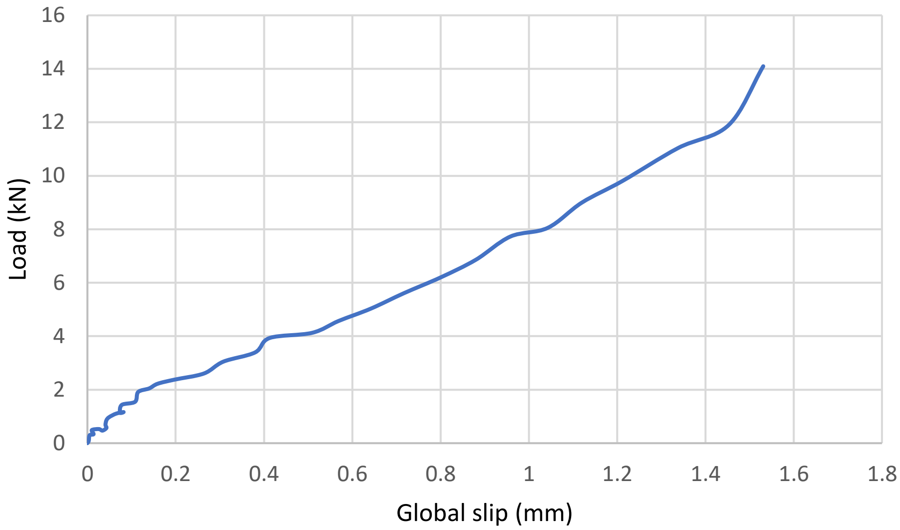

Figure 4.47: load-slip curve obtained using DIC

Although the strain profile of the surface of the composite is not available, the 2D strain map of this specimen created using DIC shows that there is no cracking or any significant strain on the surface of the composite with the whole surface covered in green indicating 0% strain as shown in Figure 4.48.

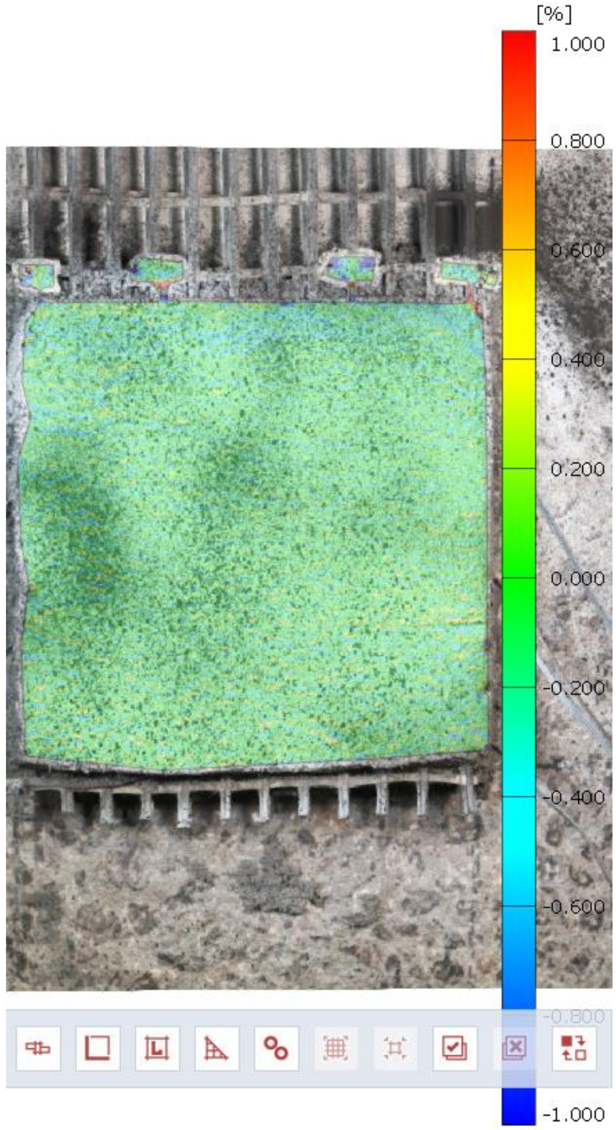

Figure 4.48: DIC generated 2D strain contour map

4.13 U_2_20_20_S1

This specimen was fabricated using two layers of unidirectional carbon fabric, anchored using spike anchors, with a composite length and width of 200 mm. Neither cracking nor delamination were observed on the composite surface before the composite-substrate debonding took place as shown in Figure 4.49. Moreover, the fabric strands did not rupture initially. After the first debonding failure, the specimen was only anchored to the substrate through the spike anchor with no bond stress between the composite and the substrate, so the load was transferred through the fabric to the spike anchor directly and then to the substrate through the anchor. The fabric continued to take the load until the fabric strands on the edges started to slip and finally the fabric ruptured shortly thereafter. This specimen was the worst performing in terms of failure stress in the fabric and at the composite-substrate interface. The initial failure stress of this specimen was 0.12 MPa when the composite-substrate debonding occurred at a load of 4.9 kN and 182.9 MPa in the fabric at the rupture load which was 11.46 kN.

(a) (b)

(c) (d)

Figure 4.49: front view (a),debonded composite (b), ruptured fabric close-up (c) and (d)

The load-slip curve shown in Figure 4.50, shows a linear increase of the load with respect to the global slip all the way to the composite – substrate debonding at the initial failure. The fabric then picked up the load again after the specimen repositioned and stretched causing a shift in the tapes position of approximately 1.8 mm upwards. After that, the load in the fabric increased linearly until the final brittle failure when the fabric finally ruptured at maximum global slip of 10 mm which initiated around 0.7 kN. The global slip was exceptionally large due to a combination of factors including the composite-substrate debonding, stretching/tightening of the loose spike anchor after the debonding and the tensile strain in the spike anchor.

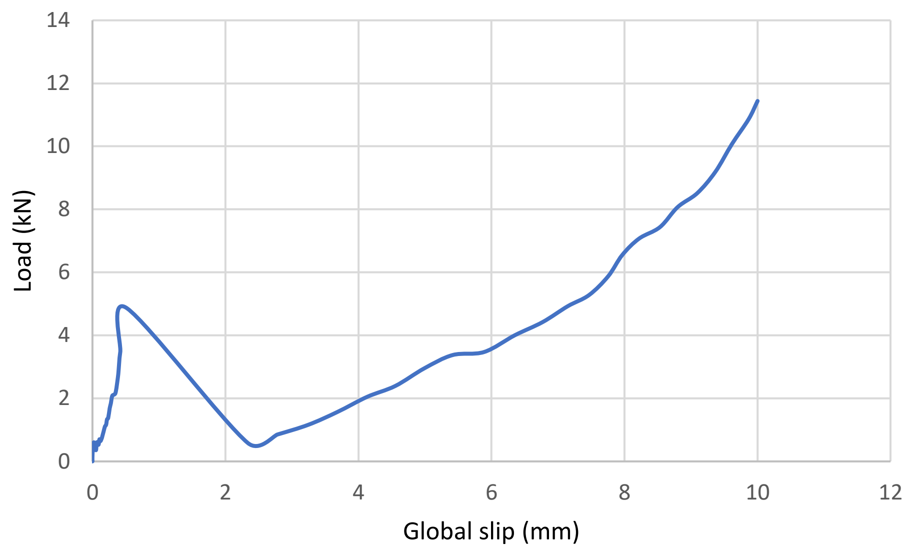

Figure 4.50: load-slip curve obtained using DIC

No strain profile could be obtained using DIC due to a software related issue during the analysis. However, strain data acquired directly from the fabric is still available with the strain gauges. A strain profile was created for every 5 kN load interval to the maximum load, and at the maximum strain as shown in Figure 4.51. It is important to mention that all these strain profiles are acquired after the debonding, since it happened at a low load. Nonetheless, the strain profile at 5 kN load is similar to that of the strain at the debonding because the difference in load is only 0.1 kN.

At 5 kN load, strain was measured to be very low at 0.07%, 20 mm from the loaded end of the composite, then dropped to 0.02 % at a depth of 70 mm from the loaded end. The strain increased at the 10 kN load checkpoint although it was still as low as 0.22% at a depth of 20 mm and 0.06% at a depth of 70 mm. The strain at 11 kN was measured to be 0.24% and 0.09% at 20 mm and 70 mm from the loaded end, respectively. Furthermore, the strain at all load points were negligible beyond a depth of approximately 120 mm from the loaded end.

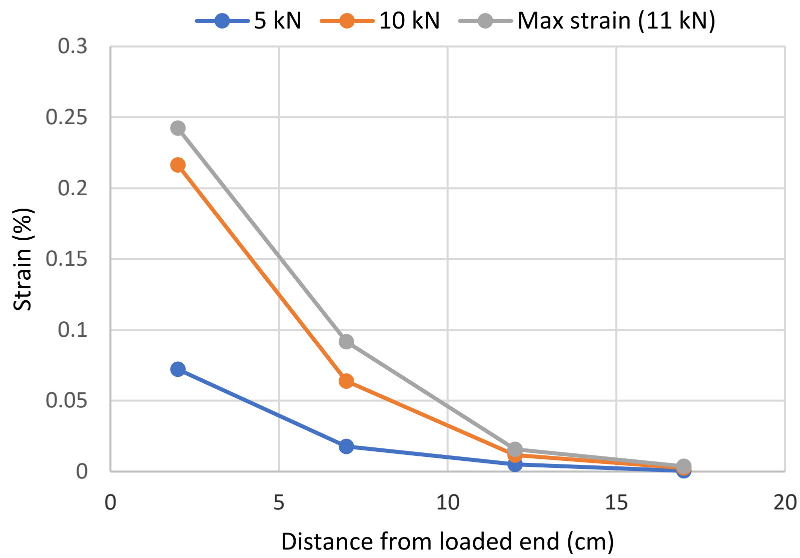

Figure 4.51: strain profile obtained from strain gauges

The load-strain curve for every strain gauge is plotted in Figure 4.52. This curve indicates that the strain did not increase until a load of 2.1 kN was reached after the debonding. The strain then increased rapidly to a maximum of 0.24% before the specimen reached the second failure. Strain Gauge 2 showed a similar strain behaviour at 70 mm from the loaded end. Although the strain started increasing significantly at the same load at both depths, it increased at a higher rate closer to the loaded end as expected.

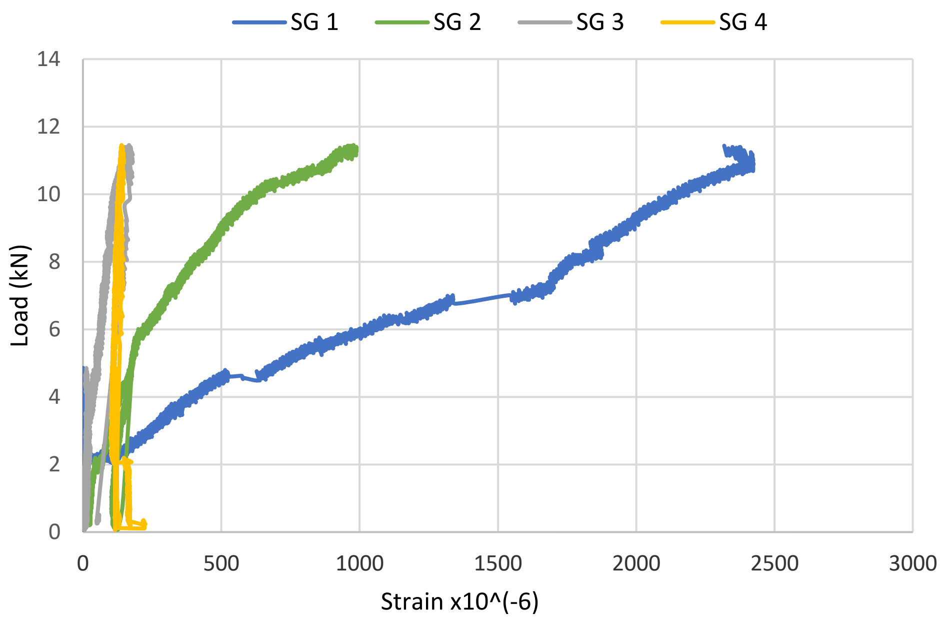

Figure 4.52: Load-strain curve for every strain gauge

The 2D strain map of this specimen created using DIC is presented in Figure 4.53. This map shows that there is no cracking or any noticeable strain on the surface of the composite with the whole surface covered in green indicating 0% strain, except for an arch of significant strain with a centre matching the embedded part of the spike anchor. This strain started propagating after the debonding which means that the spike anchor was engaged inside the composite. This also explains why the strain was distributed remarkably deeper into the composite compared to other specimens despite the relatively low strain measured by the strain gauges.

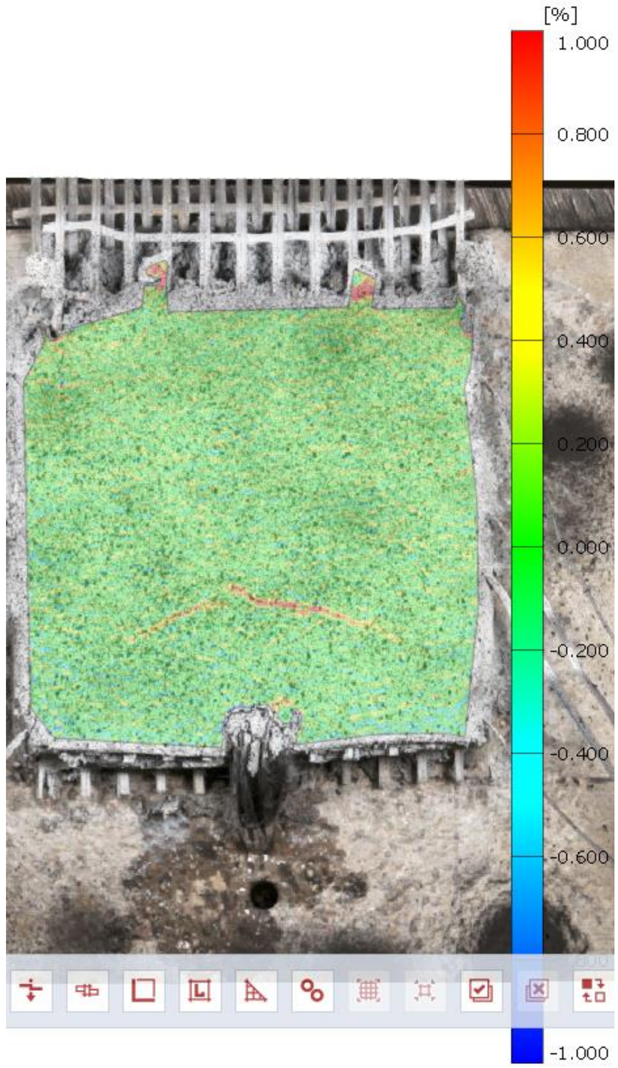

Figure 4.53: DIC generated 2D strain contour map

4.14 U_2_20_20_W

This specimen was fabricated using two layers of unidirectional carbon fabric, anchored using a wrap anchor, with a composite length and width of 200 mm. Neither cracking nor delamination were observed on the composite surface before the fabric ruptured as can be seen in Figure 4.54. Most of the ruptured fabric was in one layer which means the two fabric layers were not loaded equally. The failure stress of this specimen was 233.6 MPa in the fabric at a load of 14.6 kN.

Figure 4.54: ruptured fabric

The load-slip curve shown in Figure 4.55 shows a linear increase of the load with respect to the global slip all the way to the fabric rupture at a global slip of 1.7 mm which was brittle. A small drop in the load can be observed at 10 kN and 1.3 mm, when one of the fabric strands started wearing out though it did not affect the performance of the specimen. The slip initiated at 0.6 kN.

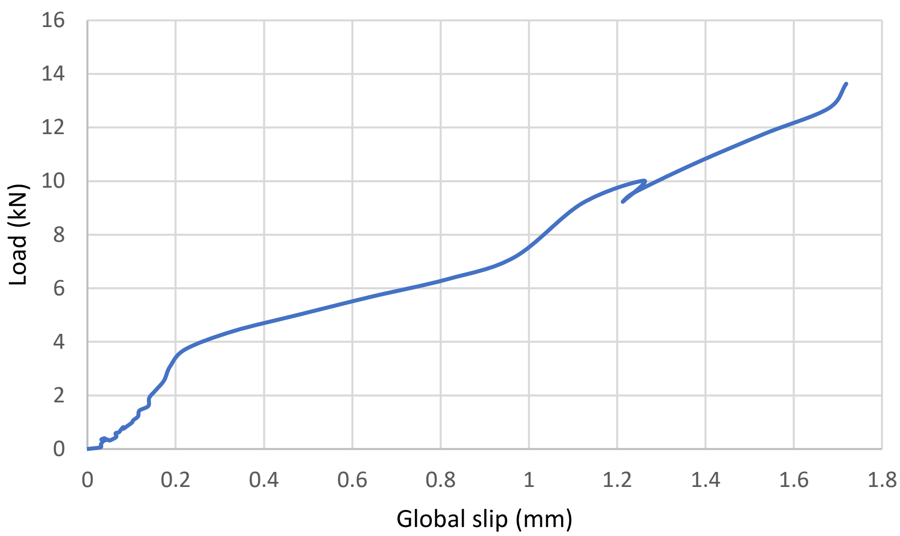

Figure 4.55: load-slip curve obtained using DIC

Due to an error with the strain gauges on this specimen, no strain profile could be created other than that of the DIC. As a result, the load-strain curve cannot be plotted either. The external strain profile obtained from the DIC of the specimen is presented in Figure 4.56 and shows no noticeable strain nor cracking on the surface of the composite as the strain is fluctuating around 0% along the length except for the top and bottom edges of the wrap anchor, which is a result of the out of plane curvature of the surface at these edges as discussed earlier.

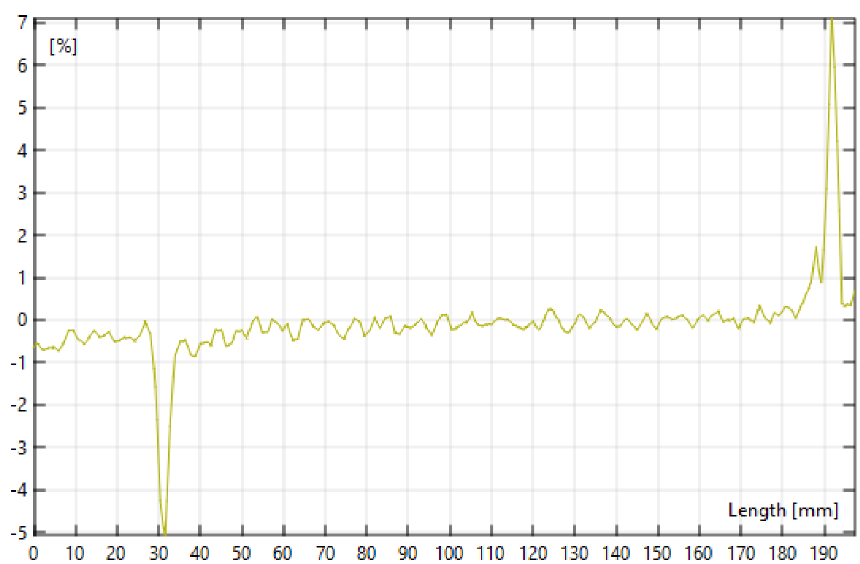

Figure 4.56: surface strain profile obtained from DIC

The 2D strain map of this specimen created using DIC is shown in Figure 4.57. Similar to the strain profile, this map shows no cracking or any significant strain on the surface of the composite with the whole surface covered in green indicating 0% strain except for the two edges of the wrap anchor.

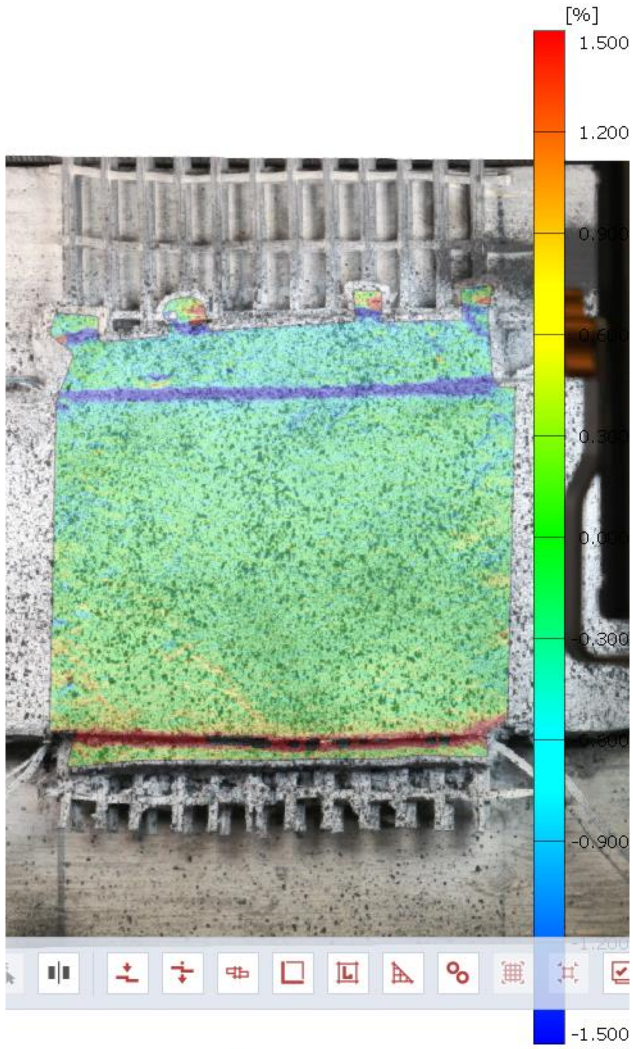

Figure 4.57: DIC generated 2D strain contour map

4.15 U_2_30_20_N

This specimen was fabricated using two layers of non-anchored unidirectional carbon fabric, with a composite length and width of 300 mm and 200 mm, respectively. Cracking and delamination were observed at the top corners of the composite surface just before the composite-substrate debonding took place as shown in Figure 4.58. Moreover, the fabric strands did not rupture and no visible fabric slip was observed in spite of the surface cracking. This specimen was one of the worst performing in terms of fabric stress due to the premature debonding. The failure stress of this specimen was 203.2 MPa in the fabric and 0.21 MPa at the composite-substrate interface at a load of 12.7 kN.

(a) (b)

Figure 4.58: side view (a) and front view of the debonded composite (b)

The load-slip curve presented in Figure 4.59 demonstrates a linear increase of the load with respect to the global slip all the way to the brittle composite debonding from the substrate at a global slip of 1.5 mm. This value of global slip is calculated based on the behaviour of the specimen prior to the lost part of the curve. The dashed orange part of the curve displays the predicted part which was lost due to the DIC software failure to track the dotted tapes after a certain point during the test. The slip initiated at 0.5 kN.

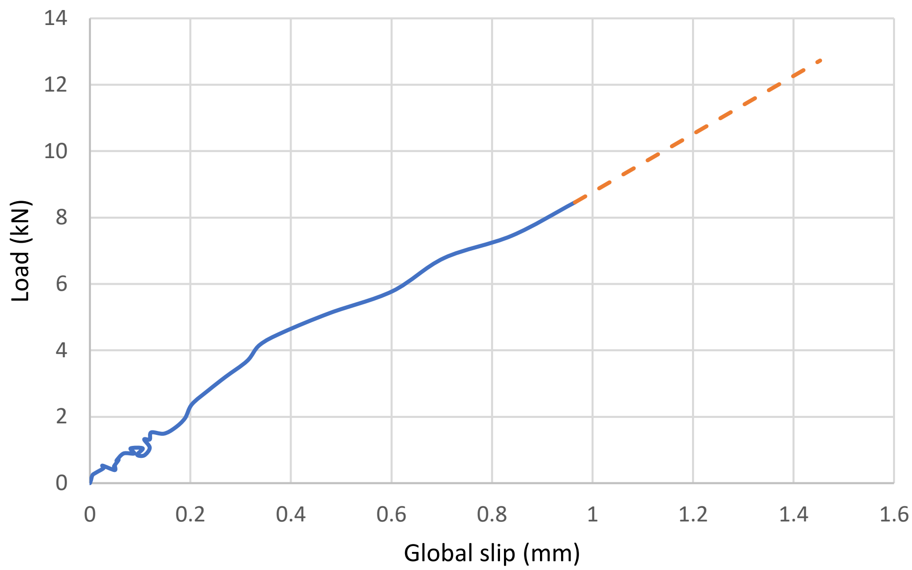

Figure 4.59: load-slip curve obtained using DIC

The external strain profile obtained from the DIC of the specimen that can be seen in Figure 4.60a shows the major crack at a depth of 33 mm from the loaded end of the composite as a spike in the strain profile. The strain at this point is measured by DIC to be 2% because this profile was taken just before the debonding after the cementitious matrix had already cracked, which means the cracking started to propagate much earlier.

In comparison, the internal strain data acquired directly from the fabric inside the composite using strain gauges shown in Figure 4.60b demonstrate significantly lower strain values at a depth of 30 mm as it was 0.74% at the same stress. At 5 kN load, strain was measured to be 0.39%, 30 mm from the loaded end of the composite, and no strain was detected beyond 110 mm along the specimen. The strain then increased to reach 0.61% and the maximum of 0.74% at 10 kN and at the failure load, respectively, at a depth of 30 mm. Furthermore, the strain was as low as 0.1% and 0.12% at a depth of 110 mm at these two load points, respectively.

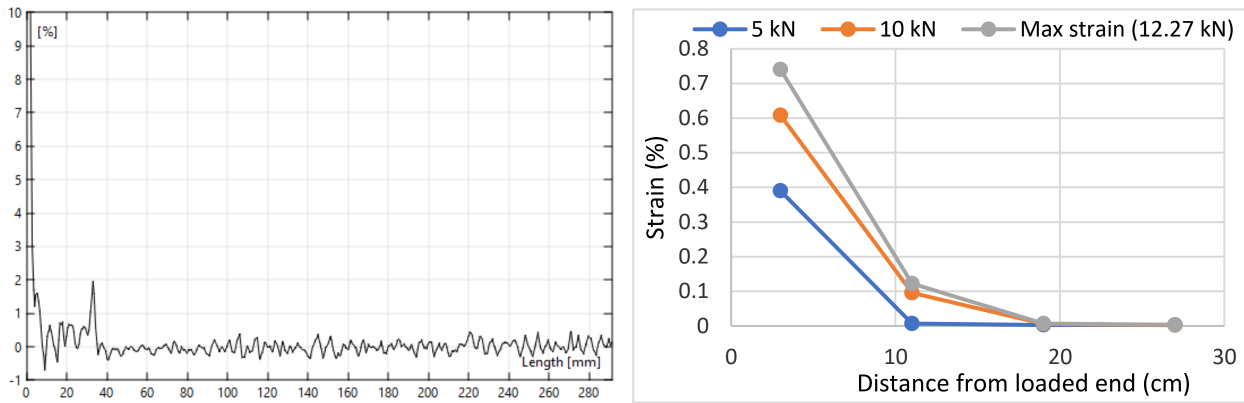

(a) (b)

Figure 4.60: surface strain profile obtained from DIC (a) and strain profile obtained from strain gauges (b)

The load-strain curve for every strain gauge is plotted in Figure 4.61. This curve shows that the strain started to increase as soon as the fabric was loaded and kept increasing almost linearly until the failure of the specimen at 12.7 kN. Moreover, the strain at a depth of 110 mm started to become noticeable at a load of 4.4 kN and started to increase at a higher rate after a load of 7 kN all the way to the failure.

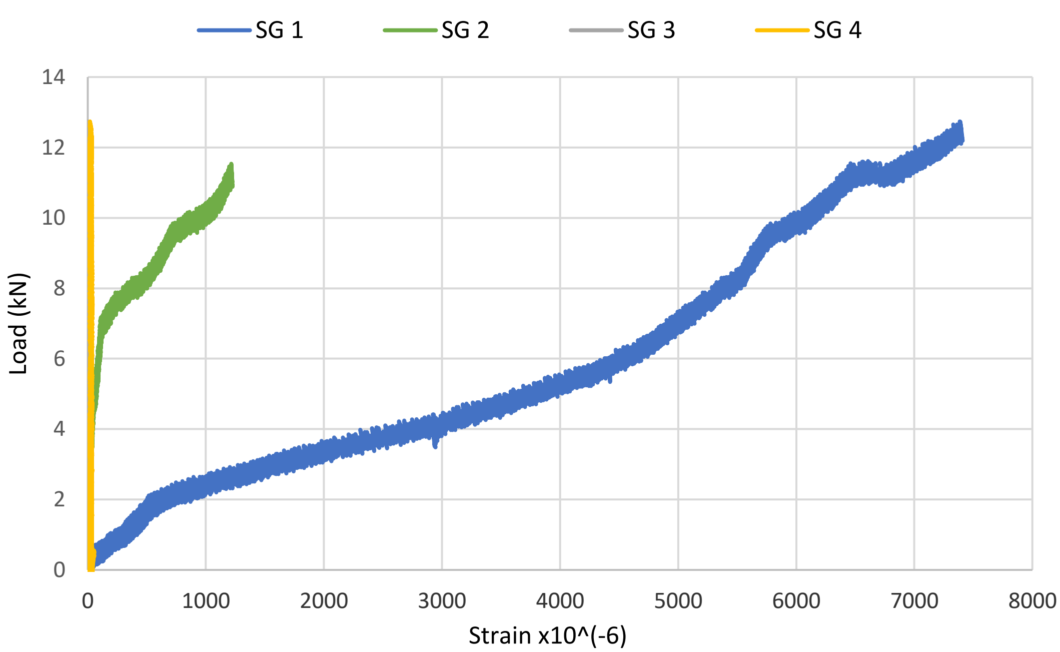

Figure 4.61: Load-strain curve for every strain gauge

The 2D strain map of this specimen created using DIC is displayed in Figure 4.62, showing the horizontal distribution of vertical strain across the width of the composite. The largest strains and deepest strain penetration tended to appear near the edges in almost all the specimens that cracked.

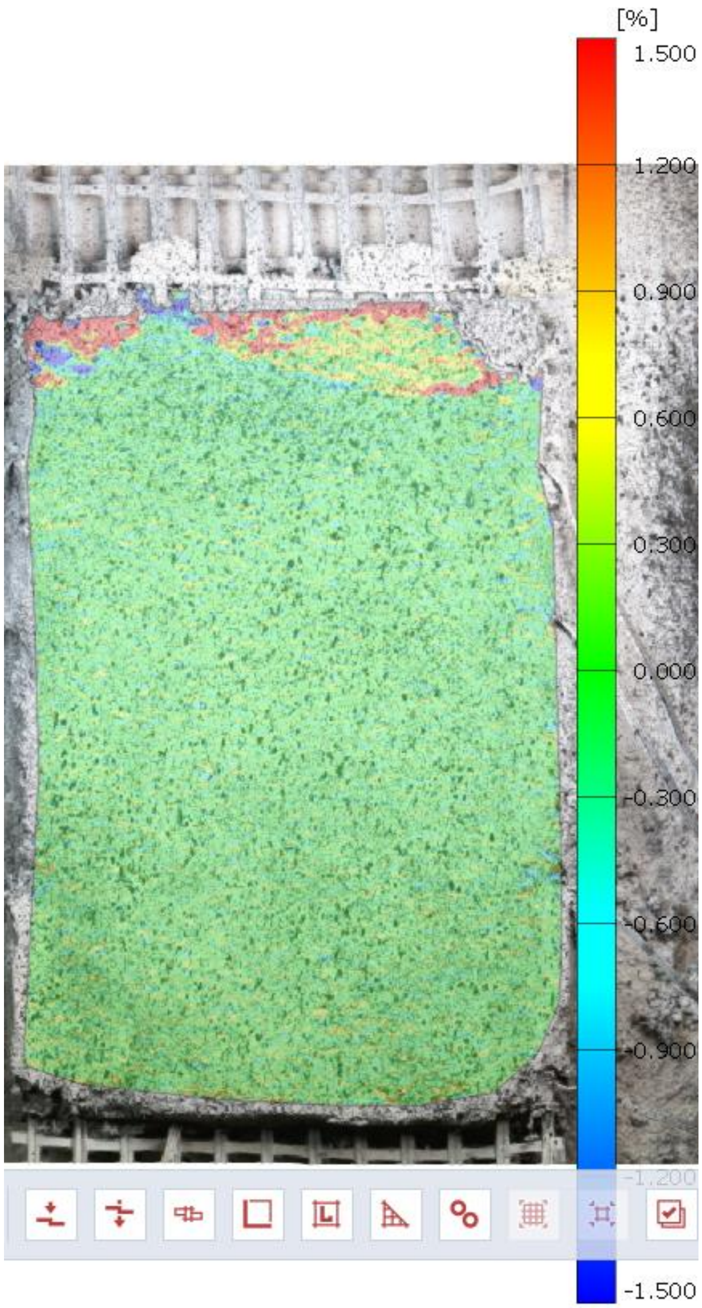

Figure 4.62: DIC generated 2D strain contour map

4.16 U_3_20_20_N

This specimen was fabricated using three layers of non-anchored unidirectional carbon fabric, with a composite length and width of 200 mm. No cracking nor delamination were observed on the surface of the composite during the test as presented in Figure 4.63. However, the fabric strands ruptured at the failure load. The failure stress of this specimen was 199.2 MPa in the fabric at a load of 18.7 kN.

Figure 4.63: ruptured fabric

The load-slip curve of this specimen is shown in Figure 4.64. After the load reached 2 kN, it continued escalating exponentially at an increasing rate with respect to the global slip, until the brittle rupture of the fabric at a maximum global slip of 0.83 mm. The strain gauges used for this specimen failed to record strains during the test which caused creating a strain profile and a load-strain plot to be unfeasible. In addition, no strain profile could be plotted for the surface of the specimen using DIC due to an error in the software during the analysis.

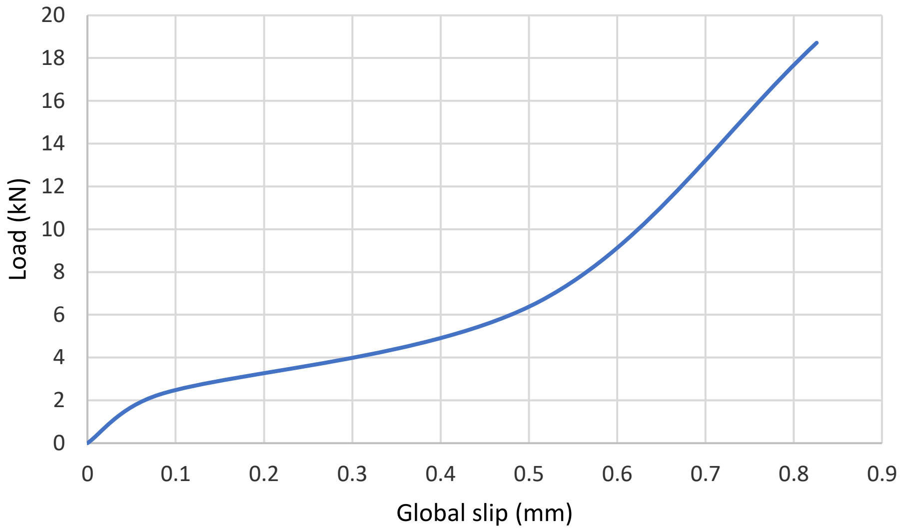

Figure 4.64: load-slip curve obtained using DIC

4.17 U_3_20_20_S2

This specimen was fabricated using three layers of unidirectional carbon fabric, anchored with two spike anchors, with a composite length and width of 200 mm. Cracking was observed near the top corners of the composite surface during the test, in addition to the matrix splitting from the sides at the closest fabric layer to the external surface of the composite, before the final rupture as shown in Figure 4.65. Moreover, few minor ruptures in the fabric were observed throughout the test before the final major one. The failure stress of this specimen was 409.9 MPa in the fabric at a load of 38.5 kN.

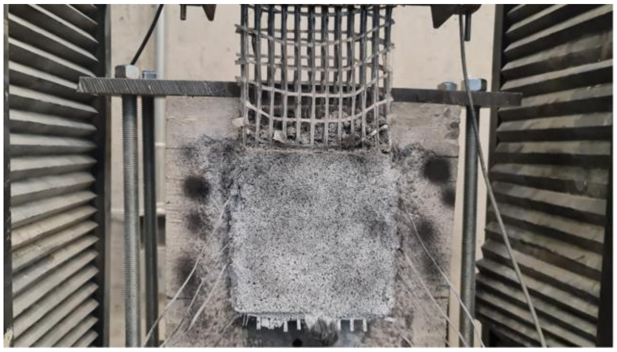 

(a) (b)

 

(c) (d)

Figure 4.65: front view (a), cracking (b), splitting (c) and fabric rupture (d)

The load-slip curve that can be seen in Figure 4.66 demonstrates an approximately linear increase of the load with respect to the global slip all the way to the first rupture where the load dropped 5.8 kN at a slip of 2.86 mm. The load was redistributed to other fabric strands after that and increased at a higher rate. This is mainly because other strands started to take more load as the fabric strands near the edges slipped more. This difference in behaviour between different fabric strands can be only noticed through DIC as shown in the 2D strain contour map which is an important advantage. The maximum recorded global slip at the brittle final rupture was 3.58 mm and it initiated at 0.7 kN. This indicates that the fabric had fully slipped, which is only the case for the edge strands where the tracked tape was attached. The fabric strands further away from the edges did not slip as much as the edge strands and other tapes were not recognized by the software.

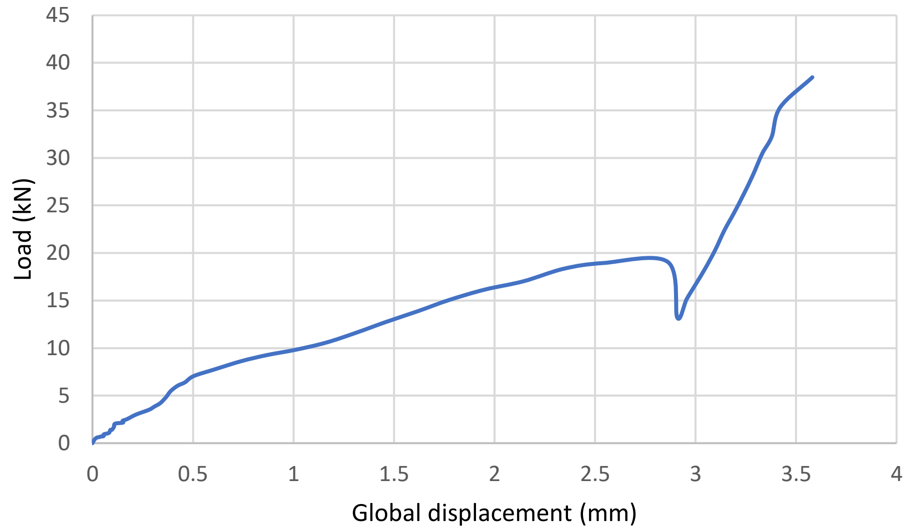

Figure 4.66: load-slip curve obtained using DIC

No external strain profile could be obtained using DIC due to a software related issue during the analysis. However, internal strain data acquired directly from the fabric is still available with the strain gauges. A strain profile was created for every 5 kN load interval up to the maximum strain recorded as presented in Figure 4.67.

At a depth of 36 mm from the loaded edge and beyond, there was no noticeable strain in the fabric at a load of 5 kN. However, the strain was measured at the same depth to be 0.01%, 0.09%, 0.11%, 0.13%, 0.15%, 0.19% and 0.2% at 10 kN, 15 kN, 20 kN, 25 kN, 30 kN, 35 kN and 38.1 kN, respectively. Although this specimen was relatively one of the best performing in terms of fabric stress, the strain was far lower than that of other specimens that ruptured because the strands where the strain gauges were attached carried only a small portion of the applied load. The strain at a depth of 90 mm was barely measurable as it was recorded to be approximately 0.01% at higher loads and no strain was detected beyond 141 mm from the loaded end of the composite.

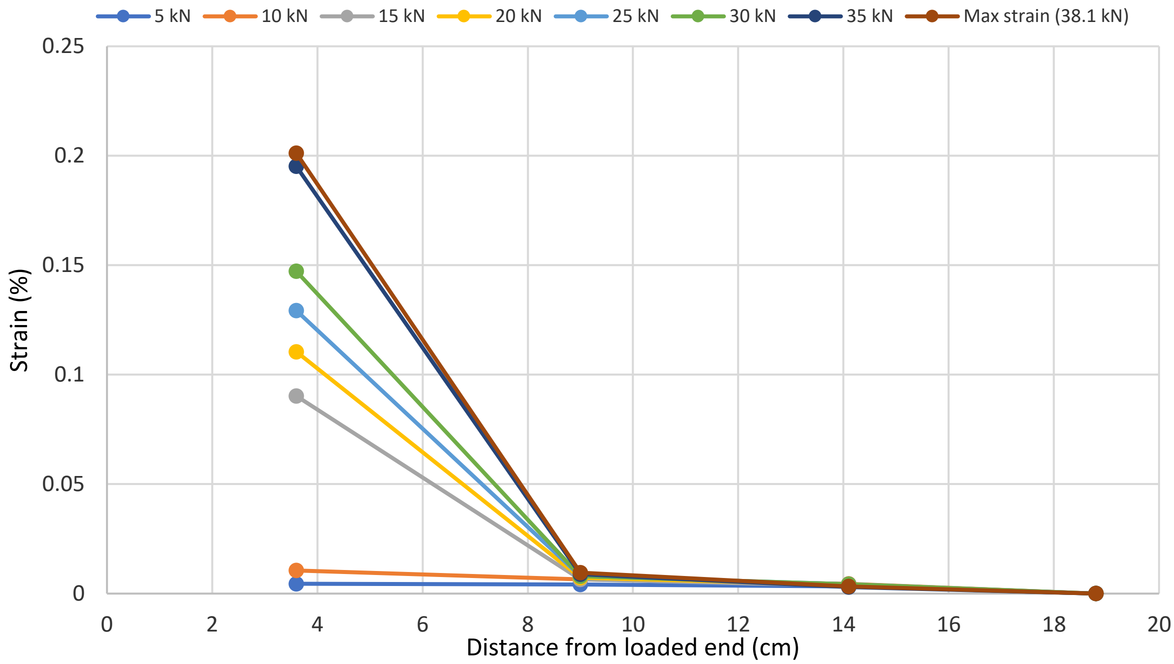

Figure 4.67: strain profile obtained from strain gauges

The load-strain curve for every strain gauge is plotted in Figure 4.68. This curve indicates that the strain started to be recognizable at a load of 7.5 kN. The load dropped slightly twice but kept increasing to reach the maximum before the final rupture at a maximum strain of 0.2%. Strain Gauge 2 was damaged during the test, so no strain data is available at that depth beyond 32 kN.

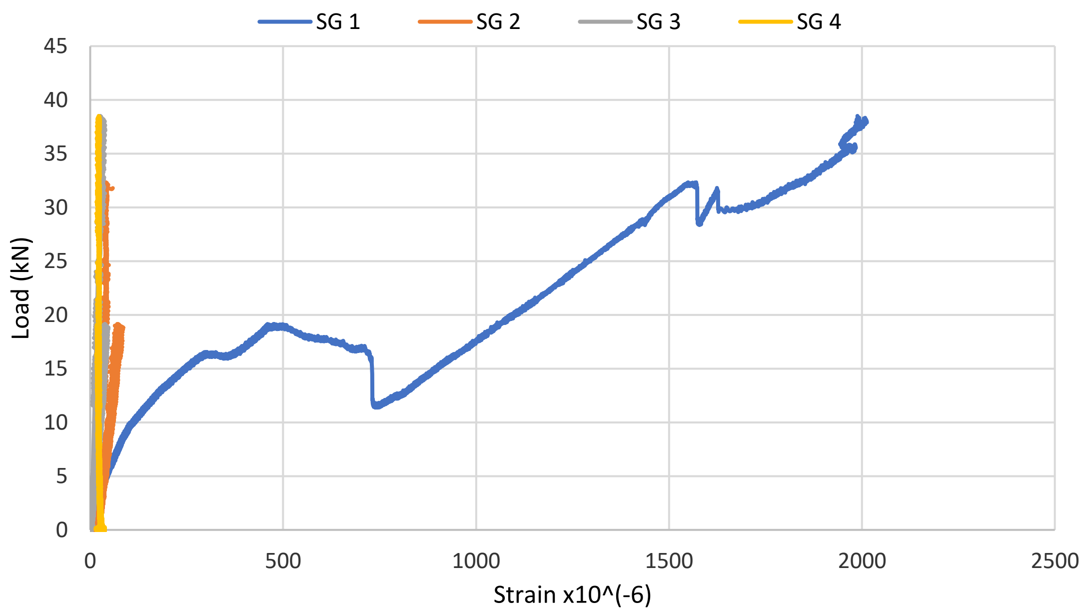

Figure 4.68: Load-strain curve for every strain gauge

The 2D strain map of this specimen created using DIC is shown in Figure 4.69. The 2D strain distribution indicates that the surface matrix was subjected to tension at the top and outside parts. As the fibres pull out and the matrix is restrained it results in bond stresses at their interface and compression in the mortar. This is the reason why the top and outside parts that are less confined can be seen in tension while the inner portion that is confined appears to be in compression against what is expected.

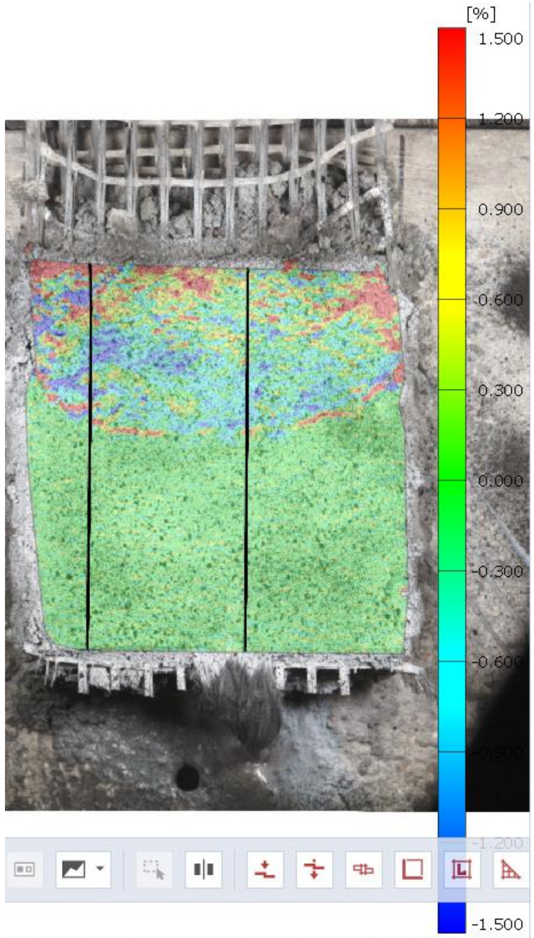

Figure 4.69: DIC generated 2D strain contour map

4.18 U_3_20_20_W

This specimen was fabricated using three layers of unidirectional carbon fabric, anchored using a wrap anchor, with a composite length and width of 200 mm. No cracking or delamination were observed on the surface of the composite during the test before the final rupture in the dry fabric as shown in Figure 4.70. The failure stress of this specimen was 250.6 MPa in the fabric at a load of 23.5 kN.

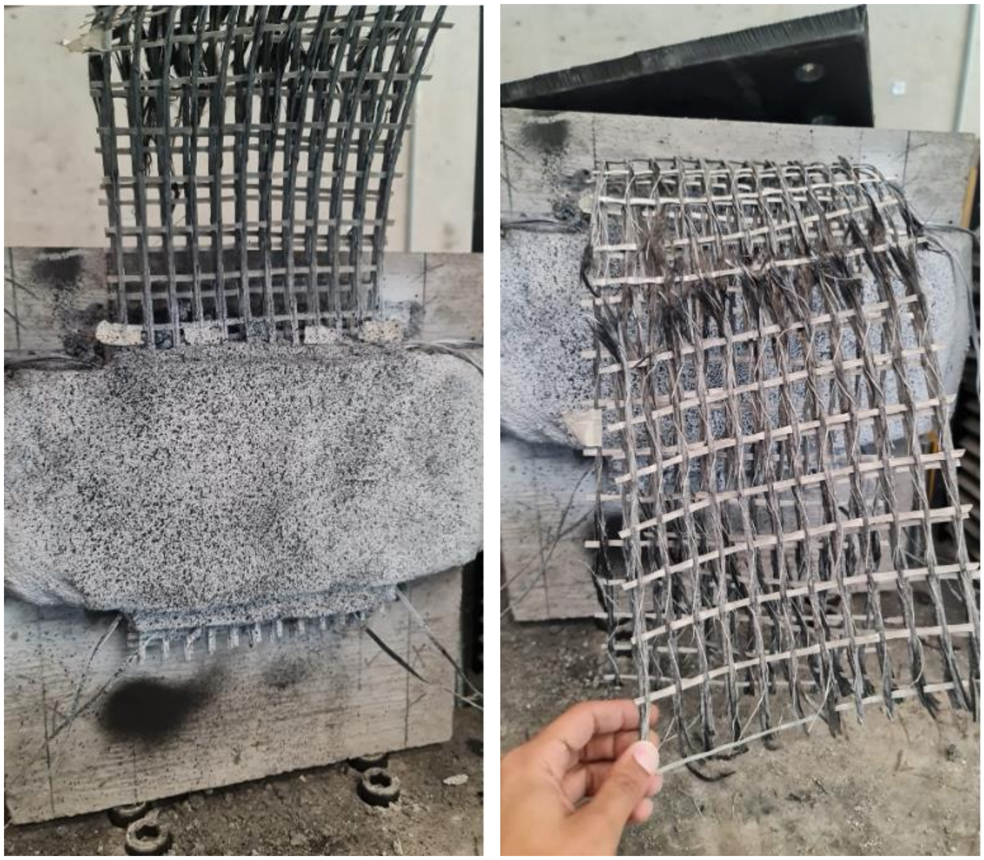

(a) (b)

Figure 4.70: front view (a) and ruptured fabric (b)

The load-slip curve of this specimen is shown in Figure 4.71. The curve is exponential as the load kept increasing at a higher rate compared to the global slip due to more strands carrying the load with higher slip. The brittle rupture of the fabric took place at a maximum global slip of 0.74 mm which initiated at 0.6 kN.

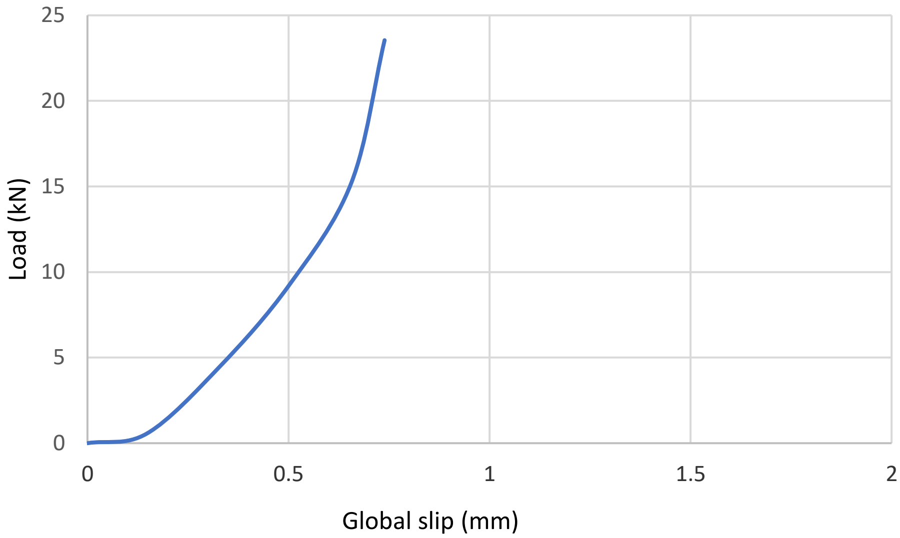

Figure 4.71: load-slip curve obtained using DIC

Due to an error with the strain gauges on this specimen, no strain profile could be created other than that of the DIC. As a result, the load-strain curve cannot be plotted either. The external strain profile obtained from the DIC of the specimen presented in Figure 4.72 shows no noticeable strain nor cracking on the surface of the composite as the strain is fluctuating around 0% along the length except for the strain spikes at the top and bottom edges of the wrap anchor, which is a result of the out of plane curvature of the surface at these edges as discussed earlier.

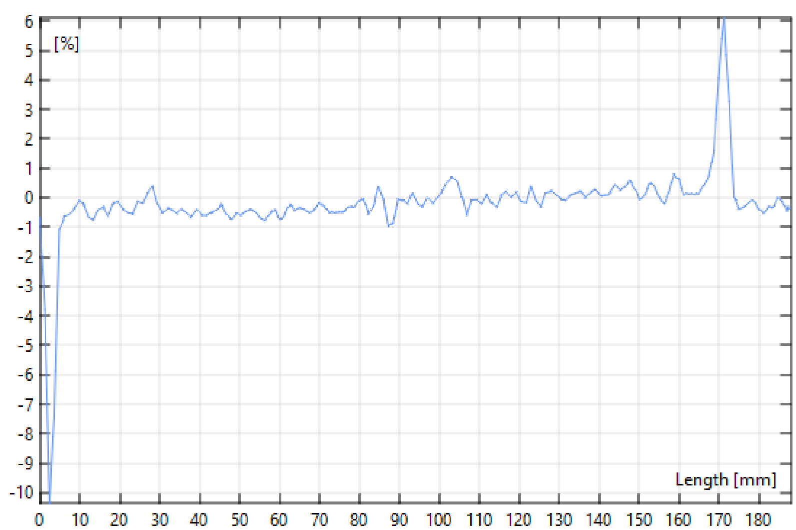

Figure 4.72: surface strain profile obtained from DIC

The 2D strain map of this specimen created using DIC is shown in Figure 4.73. Similar to the strain profile, this map shows no cracking or any significant strain on the surface of the composite with the whole surface covered in green indicating 0% strain except for the two edges of the wrap anchor.

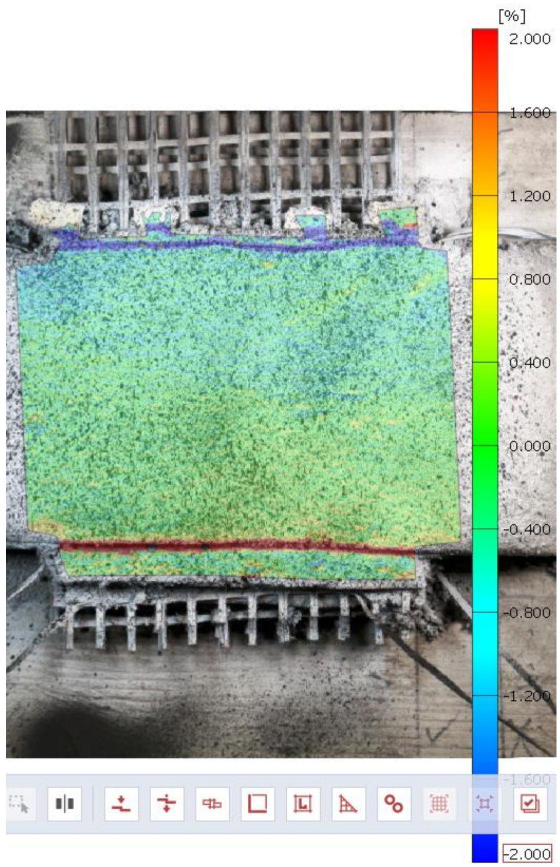

Figure 4.73: DIC generated 2D strain contour map

4.19 U_3_30_20_N

This specimen was fabricated using three layers of non-anchored unidirectional carbon fabric, with a composite length and width of 300 mm and 200 mm, respectively. No cracking or delamination were observed on the surface of the composite during the test. However, a series of ruptures in the fabric took place during the test, in addition to slip of the fabric strands near the edges as shown in Figure 4.74. Just like specimen U_3_20_20_S2, the difference in slip between the fabric strands closer to the edges of the composite and the middle ones was significant. The failure stress of this specimen was 314.5 MPa in the fabric at a load of 29.5 kN.

(a) (b)

Figure 4.74: front view (a) and edge strands (b)

The load-slip curve of this specimen is plotted in Figure 4.75. The load increases linearly with respect to the slip up to the maximum load at a global slip of 0.1 mm with one paltry rupture that caused the load to drop 1.4 kN. After reaching the maximum load, the specimen started failing with a complex mechanism that was a mix of fabric slip and a series of minor fabric ruptures occurring sequentially until the maximum slip of 0.24 mm. Unfortunately, this specimen was the first and the only one with no tapes attached to the fabric strands at the edges of the composite, hence the lack of global slip data of these strands where most of the slip happened. Tapes were added on the edges for specimens that followed.

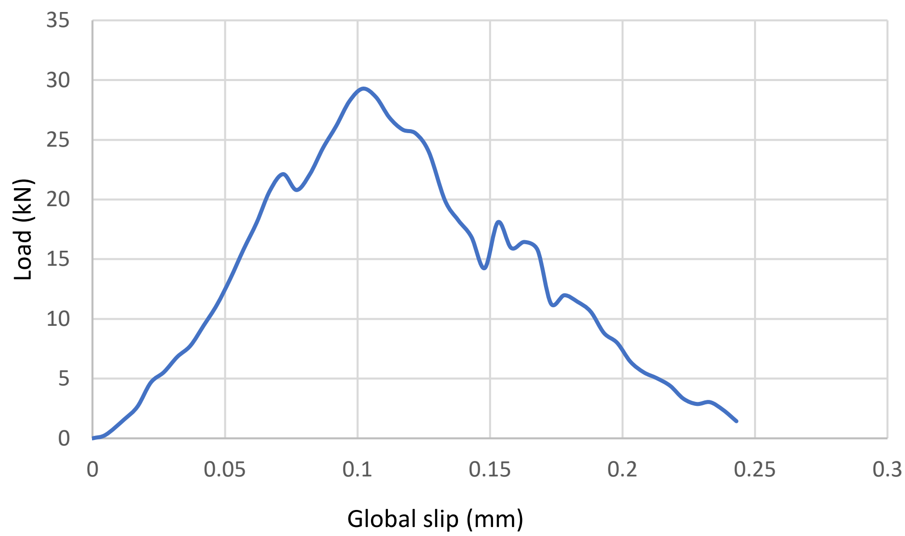

Figure 4.75: load-slip curve obtained using DIC

The external strain profile obtained from the DIC of the specimen that can be seen in Figure 4.76a shows the strain fluctuating between 0.25% and -0.2% although no cracking was observed on the surface of the composite. This is mostly a result of external noise during the test which affected the DIC analysis.

In contrast, the internal strain data acquired directly from the fabric inside the composite using strain gauges shown in Figure 4.76b demonstrate significantly different strain values. At a depth of 30 mm, the strain was measured to be 0.01 % at 15 kN. The strain was insignificant at lower load points and no strain data is available at this depth at loads higher than 20 kN since the strain gauge got detached during the test. At a depth of 110 mm, the strain was measured to be 0.17%, 0.15% and 0.03% at 28.5 kN, 25 kN and 20 kN, respectively. The strain at this depth was insignificant at loads below 15 kN, which is the same for strains beyond 190 mm from the loaded end at any load.

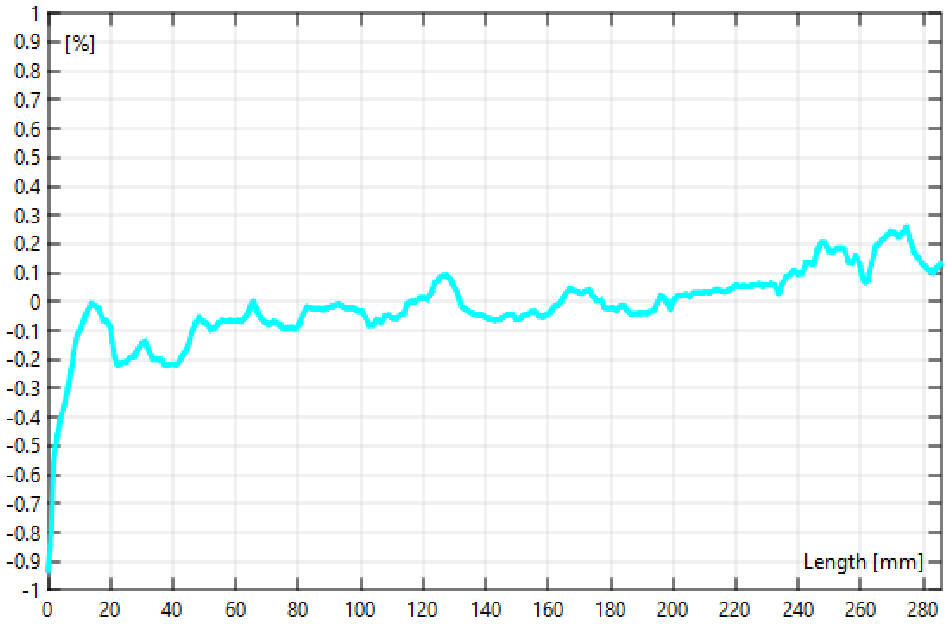

(a)

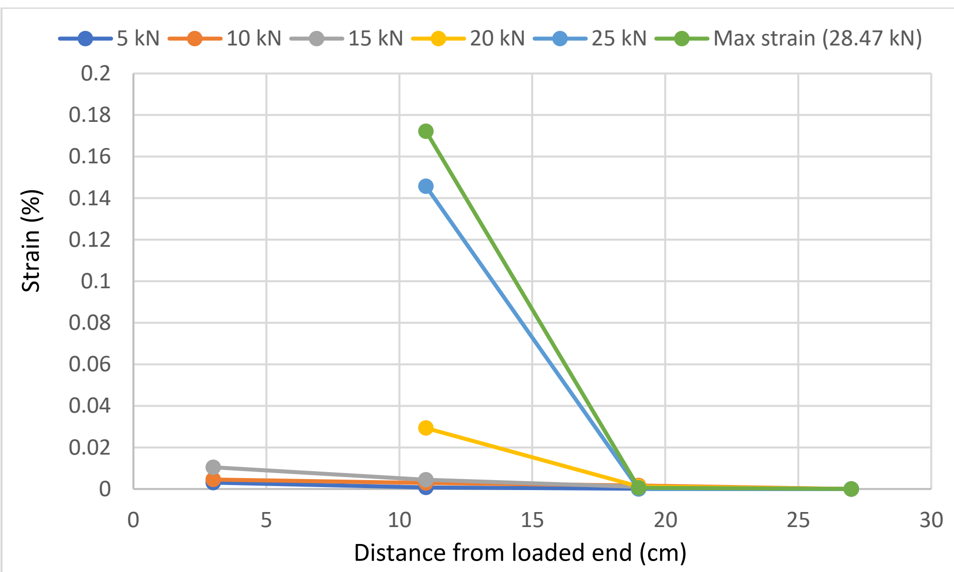

(b)

Figure 4.76: surface strain profile obtained from DIC (a) and strain profile obtained from strain gauges (b)

The load-strain curve for every strain gauge is shown in Figure 4.77. This curve indicates that the strain started to be recognizable at a load of 11.5 kN, 30 mm from the loaded end. The strain kept increasing with the load until strain gauge SG1 got detached. On the other hand, the strain did not start to become noticeable until a load of 14.6 kN was reached. It increased rapidly after the first rupture until it got to a maximum of 0.17%. This strain is very low compared to the theoretically expected one due to the difference in loading between the fabric strands, especially with three layers of fabric.

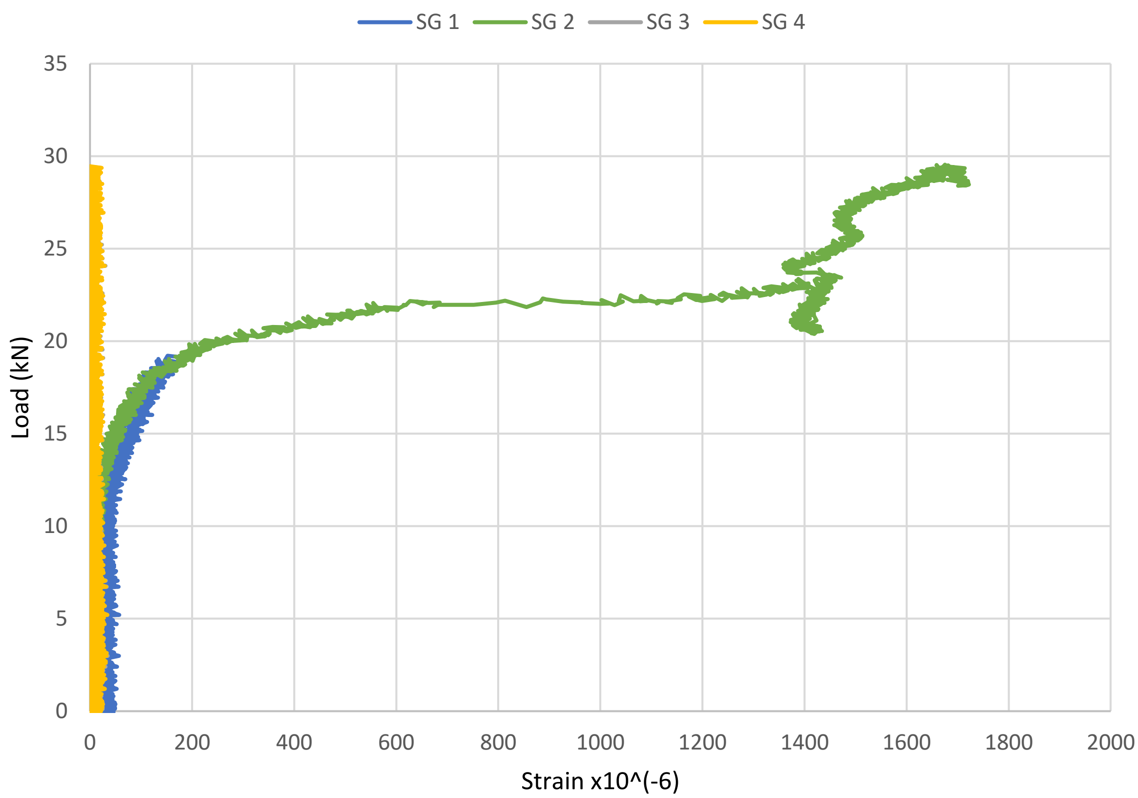

Figure 4.77: Load-strain curve for every strain gauge

The 2D strain map of this specimen created using DIC is shown in Figure 4.78. Similar to the strain profile, this map shows no cracking or any significant strain on the surface of the composite with the whole surface covered in green indicating 0% strain except for the top edge of the composite.

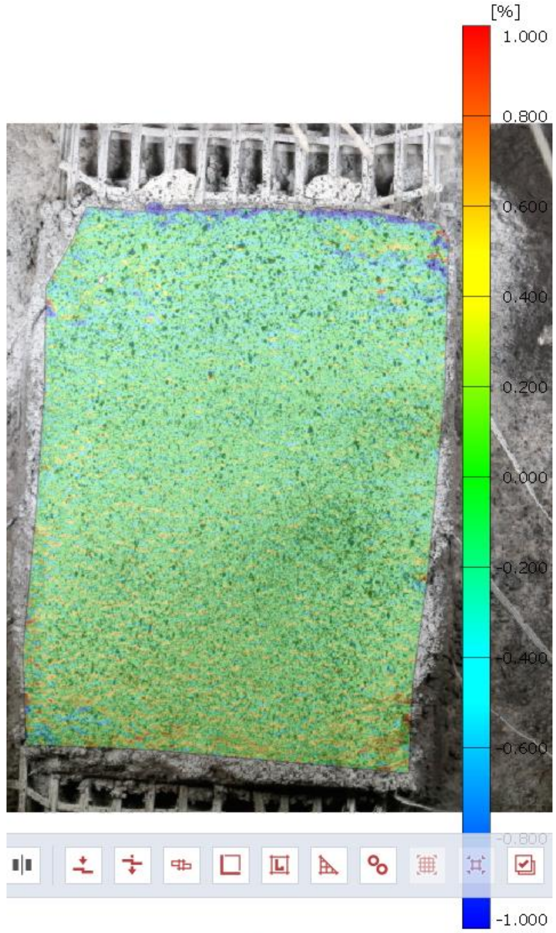

Figure 4.78: DIC generated 2D strain contour map

4.20 U_3_30_20_S2

This specimen was fabricated using three layers of unidirectional carbon fabric, anchored with two spike anchors, with a composite length and width of 300 mm and 200 mm, respectively. Cracking that propagated from the top left corner of the composite was observed which led to delamination and spalling later during the test. Moreover, fabric strands near the edge started slipping before the fabric rupture took place at the failure load as shown in Figure 4.79. The failure stress of this specimen was 310.6 MPa in the fabric at a load of 29.2 kN, which is close to that of unanchored specimen U_3_30_20_N.

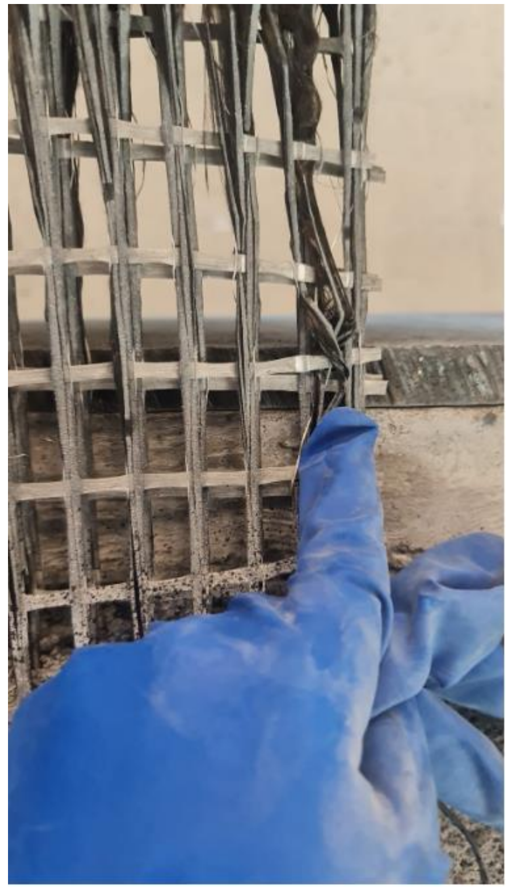

(a) (b)

(c)

Figure 4.79: fabric rupture close-up (a) and (b) and matrix cracking (c)

The load-slip curve that can be seen in Figure 4.80 demonstrates an approximately linear increase of the load with respect to the global slip all the way to a load of 20 kN where a load redistribution occurred which caused the load to increase at a higher rate until failure. This behaviour is very similar to that of specimen U_3_20_20_S2 which was also anchored with two spike anchors. The maximum recorded global slip at the brittle final rupture was 2.95 mm. The fabric strands further away from the edges did not slip as much as the edge strands and other tapes were not recognized by the software. The slip initiated at 0.6 kN.

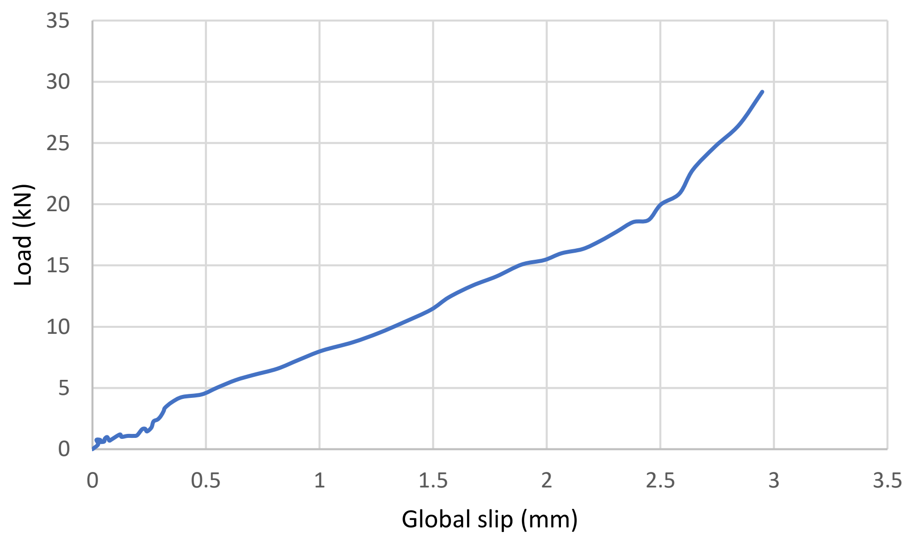

Figure 4.80: load-slip curve obtained using DIC

No external strain profile could be obtained using DIC due to a software related issue during the analysis. However, internal strain data acquired directly from the fabric is still available with the strain gauges. A strain profile was created for every 5 kN load interval up to the maximum strain recorded as presented in Figure 4.81.

At a depth of 30 mm from the loaded edge, the strain in the fabric started picking up early as it was measured at a load of 5 kN to be 0.01%. The same strain gauge recorded the strain to be 0.04%, 0.07%, 0.13%, 0.27% and 0.7% at 10 kN, 15 kN, 20kN, 25 kN and 28.7 kN, respectively. Furthermore, the maximum strain at 110 mm from the loaded end was measured to be 0.01% before the specimen fully ruptured.

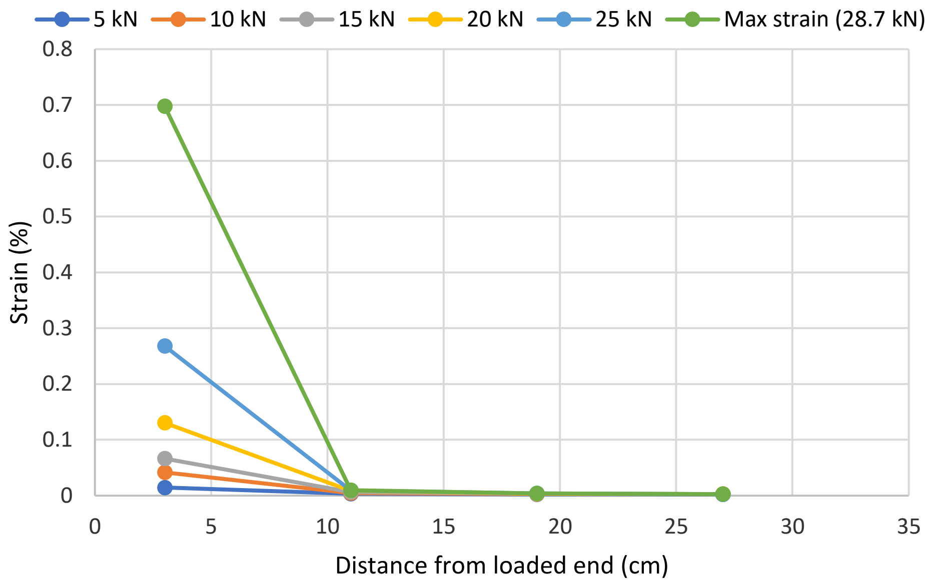

Figure 4.81: strain profile obtained from strain gauges

The load-strain curve for every strain gauge is presented in Figure 4.82. This curve shows that the strain started to be recognizable at a load of 3 kN, 30 mm from the loaded end. The strain kept increasing with the load until the strain reached 0.14% at 20.4 kN when the load redistribution happened. The strain increased at a higher rate until the rupture occurred at the maximum strain of 0.7%.

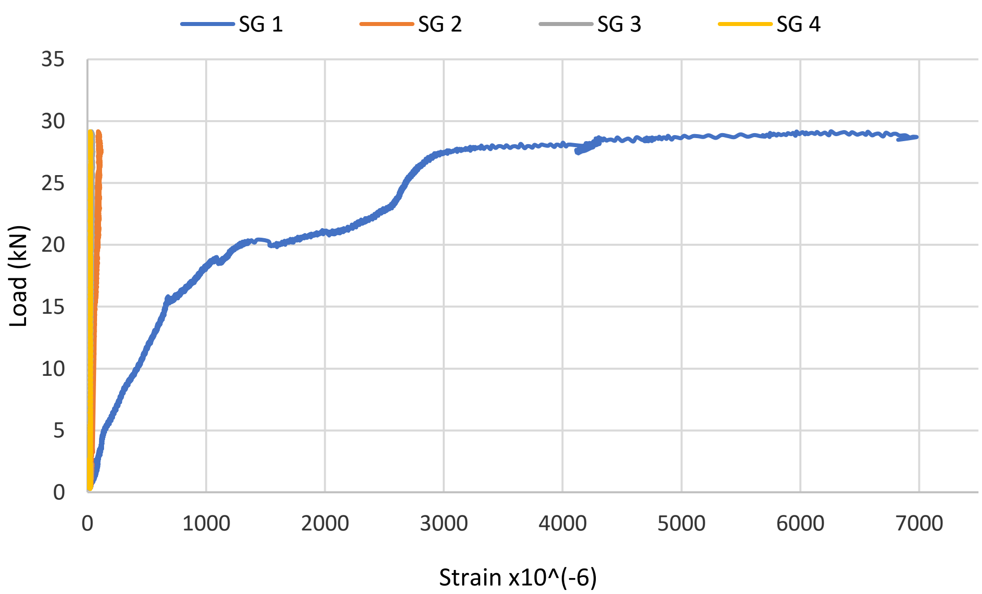

Figure 4.82: Load-strain curve for every strain gauge

5.0 Discussion

5.1 Non-anchored specimens

The results of the non-anchored specimens were compared to each other to better understand the effect of the number of layers and the bonded length of the composite while other factors are fixed. The failure stress of each specimen can be used to indicate the activation percentage of the total strands that carry the load. Figure 5.1 compares the failure stress of all the non-anchored specimens. Specimens with bidirectional fabric are displayed in brown colour and the ones with unidirectional fabric are displayed in blue.

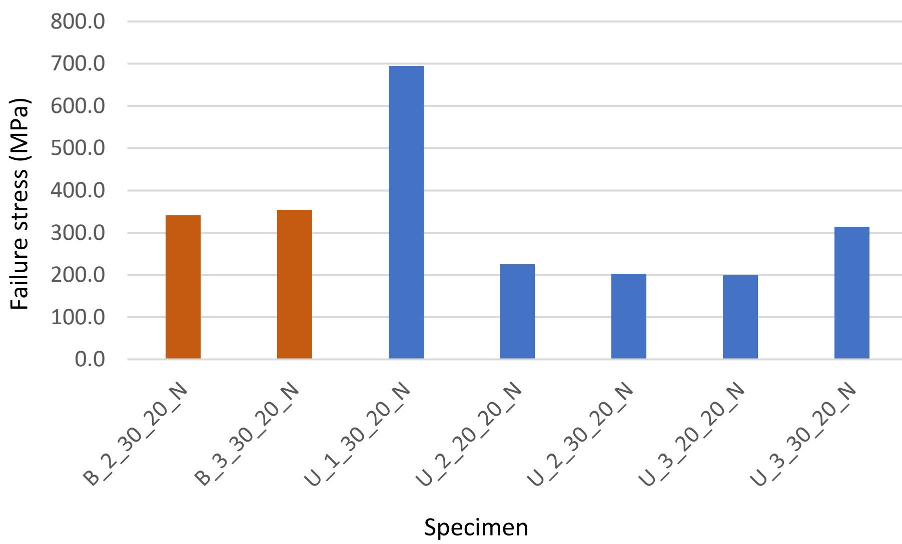

Figure 5.1: failure stress of all the non-anchored specimens

Specimens with non-anchored unidirectional fabric demonstrated a significant difference in failure stress depending on the number of layers. The specimen with one layer failed due to fabric rupture at 695.2 MPa which is more than double that of other non-anchored unidirectional specimens although it was 78.6% of the ultimate strength specified by the manufacturer. Moreover, specimens with two layers failed at a higher stress when compared to specimen U_3_20_20_N and slightly lower than that of specimen U_3_30_20_N although the 2-layered specimens failed due to composite-substrate debonding while the 3-layered specimens failed due to fabric rupture, which means that the fabric in the 2-layered specimens could withstand higher stress compared to the 3-layered specimens. This result can be attributed to the difficulty experienced while trying to ensure equal loading of the fabric strands for specimens with multiple layers during installation.

Specimens with non-anchored bidirectional fabric had a similar failure stress although they withstood higher stresses than the unidirectional ones with the same number of layers due to the higher material strength of the bidirectional fabric. Nonetheless, specimens with bidirectional fabric also failed prematurely with failure stresses corresponding to 34.6% and 36% of the theoretical one for specimens B_2_30_20_N and B_3_30_20_N, respectively.

The length of the bonded region was not correlated with the failure stress since the failure modes for most of these specimens were not governed by debonding. There is no pattern to be recognized when comparing the failure stress of non-anchored specimens with the same number of layers and different composite length.

The failure mode for most of the non-anchored specimens was fabric rupture. Moreover, only specimens with multiple layers failed due to composite-substrate debonding. In addition, there seems to be no significant effect of the bonded length when comparing specimens with different bonded lengths which is expected since the failures were premature. Other studies have reported premature failures of FRCM to be associated with multiple layers and the thickness of the composite. This will be addressed in more detail after the comparison between the anchorage systems later in this section.

The strain profiles of the fabric at failure of non-anchored specimens are compared in Figure 5.2. The specimens with unidirectional fabric experienced a similar strain penetration into the composite to a depth of 190 mm, regardless of the number of layers with a difference in strain as little as 0.05% at a depth of 110 mm. This was not expected since specimen U_3_30_20_N ruptured at a higher stress. However, it is possible that the instrumented strands in that specimen were not the critical ones. It is important to take into consideration that the strain profiles used for the comparison are obtained at the failure stress of the specimens which differs from one specimen to another. This was done because the highest common load at which a strain profile is available for most specimens is 5 kN. At such low load the strain is low and the strain profiles are not defined enough for a meaningful comparison between the specimens. The reasons behind the lack of strain data at higher loads for a lot of the specimens are discussed later in this section.

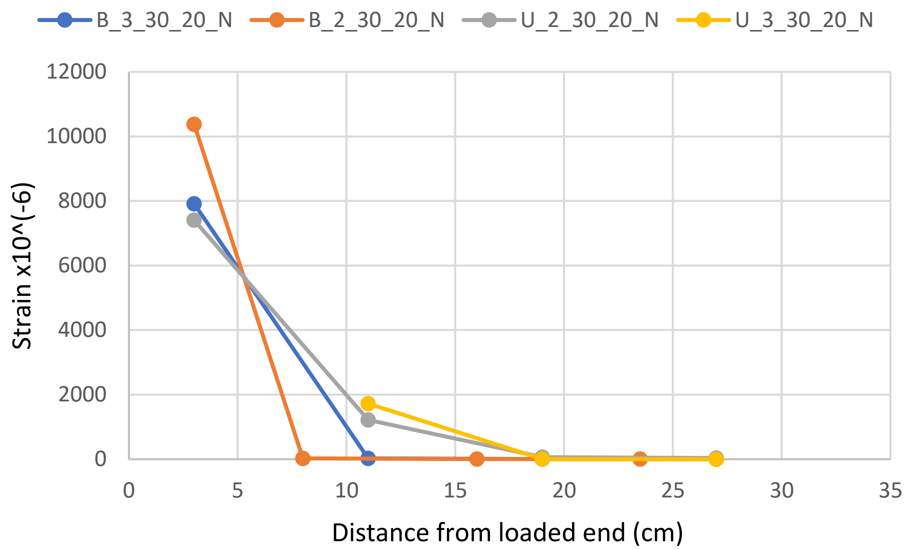

Figure 5.2: strain profiles of the fabric at failure of non-anchored specimens

In comparison, specimens with bidirectional fabric demonstrated shallower penetration of the strain into the composite by 80 mm and 110 mm for specimens B_3_30_20_N and B_2_30_20_N, respectively, despite reaching a higher tensile stress. A possible explanation for this observation is that the horizontal fabric strands provide some anchorage for the longitudinal strands (Azam et al., 2019; Azam et al., 2018). It is possible that the instrumented strands were not the critical ones. However, the maximum strain values reached were close to the expected failure strains which suggests the behaviour was properly captured. Specimens B_2_30_20_N and B_3_30_20_N did not experience any significant strain beyond a depth of 80 mm and 160 mm, respectively.

In addition, non-anchored specimens were compared in terms of the stress at slip initiation, average slip rate and the maximum recorded slip which are summarized in table 5.1. Specimens with bidirectional fabric demonstrated slip initiation at a higher stress compared to unidirectional specimens. This can also be due to the horizontal fabric strands providing some anchorage for the longitudinal strands which agrees with the shallow strain penetration into the bidirectional specimens. However, bidirectional specimens slipped at a higher rate on average than unidirectional ones and showed a higher maximum global slip as well. The maximum global slip was expected to be higher for the non-anchored bidirectional specimens as they failed at a significantly higher stress than the unidirectional ones included in table 5.1, and it was found to be correlated.

Table 5.1: slip measurements of non-anchored specimens

Specimen	Slip initiation load (kN)	Slip initiation stress (MPa)	Average slip rate (mm/kN)	Maximum slip (mm)
B_2_30_20_N	0.8	45.5	0.33	2.44
B_3_30_20_N	0.6	22.7	0.22	2.05
U_2_20_20_N	1.0	16.0	0.11	1.53
U_2_30_20_N	0.5	8.0	0.11	1.45

5.2 Spike anchor specimens

The failure stress of every specimen anchored using spike anchors is presented in Figure 5.3. Specimens with bidirectional fabric are displayed in brown colour and the ones with unidirectional fabric are displayed in blue. Specimens B_2_30_20_S1, B_3_30_20_S2, U_1_30_20_S1, U_2_20_20_S1, U_3_20_20_S2 and U_3_30_20_S2 demonstrated relatively low failure stresses at 35.3%, 68.8%, 38.6%, 20.7%, 46.3% and 35.1% of the theoretical strength of the composite, respectively. As expected, specimens with bidirectional fabric demonstrated higher strength compared to the ones with unidirectional fabric with the same number of layers. Unlike the non-anchored specimens, no direct correlation was observed between the failure stress and the number of layers. However, it can be noted that it is a combination of the number of spike anchors and the number of fabric layers that affect the actual failure stress in the fabric. The increase in the number of spike anchors and the decrease in the number of fabric layers increases the failure stress of the composite, with the effect of the number of spike anchors being more predominant.

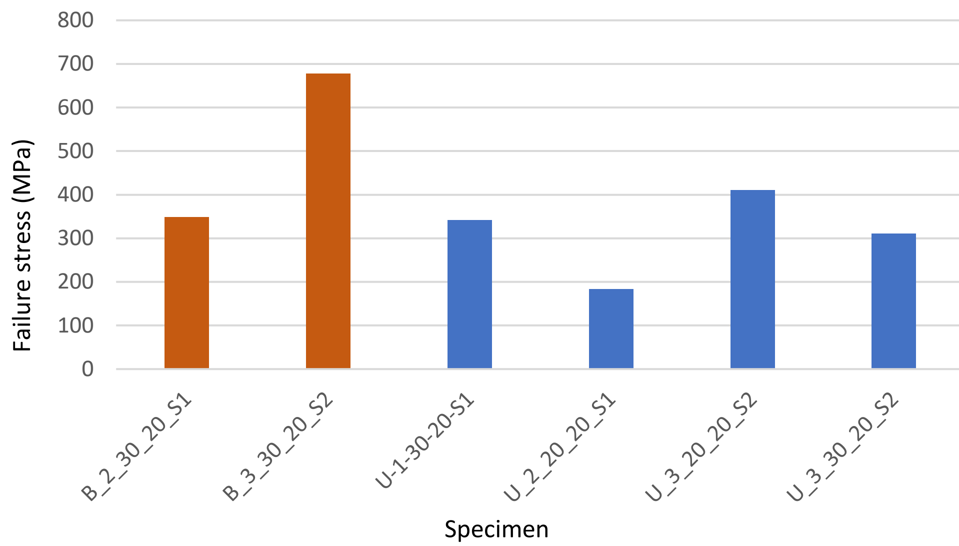

Figure 5.3: failure stress of all the spike anchored specimens

All specimens anchored using spike anchors failed due to fabric rupture apart from specimen U_2_20_20_S1 which debonded from the substrate initially before the fabric rupture took place. This was a result of not tightening and stretching the spike anchor properly while inserting it into the concrete block (substrate), unlike the spike anchors in other specimens which were stretched firmly. This means that the spike anchor did not actually bear any load until the composite debonded from the substrate. Only multi-layered specimens exhibited visible signs of fabric slip, and it was mostly the strands on the edges of the composite.

The strain profiles of the fabric at failure of specimens with spike anchors are compared in Figure 5.4. A slight increase in the depth of strain penetration into the composite was noticed with the increase of the number of fabric layers in the unidirectional fabric specimens. The relatively low strain at failure measured on the fabric of both specimens U_3_20_20_S2 and U_3_30_20_S2 at a depth of 30 mm, despite both failing due to fabric rupture, suggests that the strands were not evenly loaded and the strands where the strain gauges were attached did not carry as much load as other overloaded strands. This also implies that the actual strain penetration into the composite was significantly deeper than displayed in this strain profile, especially with the matrix cracking. Specimen U_2_20_20_S1 is an exception since the fabric was only attached to the substrate by the spike anchor pulling the fabric directly from the bottom of the composite after the composite-substrate debonding, which caused the strain to penetrate significantly deeper into the composite compared to other specimens to a depth of more than 120 mm.

Similar to the case with non-anchored specimens, specimens with bidirectional fabric demonstrated shallower penetration of the strain into the composite compared to specimens with unidirectional fabric with the same number of fabric layers although it was less significant. Both specimens with bidirectional fabric did not experience any significant strain beyond a depth of 114 mm.

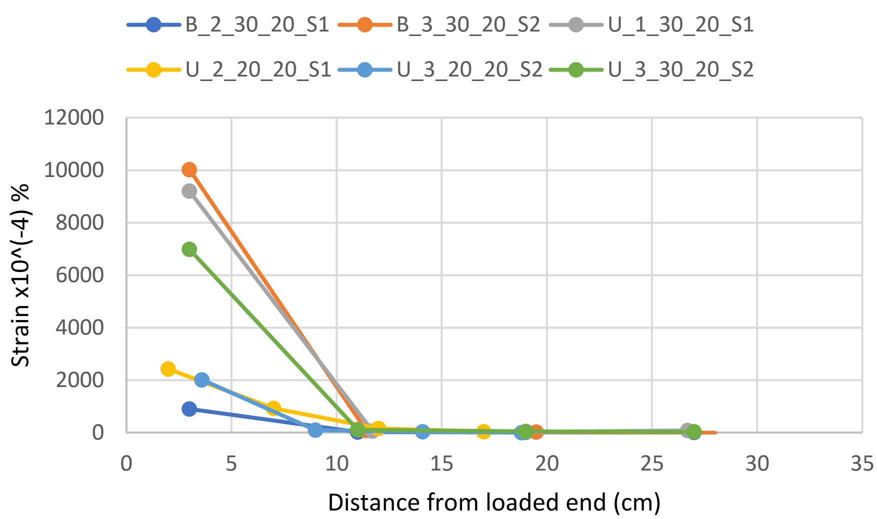

Figure 5.4: strain profiles of the fabric at failure of spike anchored specimens

Furthermore, spike anchored specimens were compared in terms of the stress at slip initiation, average slip rate and the maximum recorded slip which are summarized in table 5.2. Similar to what was observed in non-anchored specimens, spike anchored specimens with bidirectional fabric exhibited slip initiation at higher stresses than unidirectional specimens. Specimen B_3_30_20_S2 started to slip at a stress of 70.5 MPa which is 9.5 and 11 times that of specimens U_3_20_20_S2 and U_3_30_20_S2, respectively, that had the same number of fabric layers. Moreover, the average slip rate was observed to be lower for specimens with more fabric layers regardless of fabric type while the maximum global slip was more correlated to failure stress. In addition, it was observed that slip initiation stress of the spike anchored unidirectional specimens decreased with more fabric layers which may indicate that the additional layers have a lower bond efficiency.

Table 5.2: slip measurements of spike anchored specimens

Specimen	Slip initiation load (kN)	Slip initiation stress (MPa)	Average slip rate (mm/kN)	Maximum slip (mm)
B_2_30_20_S1	0.8	45.5	0.22	1.26
B_3_30_20_S2	1.9	70.5	0.13	2.19
U_1_30_20_S1	0.4	12.8	0.25	2.01
U_3_20_20_S2	0.7	7.4	0.13	3.58
U_3_30_20_S2	0.6	6.4	0.13	2.95

5.3 Wrap anchor specimens

The failure stress of every specimen anchored using wrap anchors is presented in Figure 5.5. Specimens with bidirectional fabric are displayed in brown colour and the ones with unidirectional fabric are displayed in blue. Specimens B_2_30_20_W, B_3_30_20_W, U_1_20_20_W, U_2_20_20_W, U_2_30_20_W and U_3_20_20_W showed failure stresses corresponding to 53.1%, 36.9%, 57%, 26.4%, 26.6% and 28.3% of the theoretical strength of the fabric, respectively. Similar to other anchor types, specimens with bidirectional fabric demonstrated higher strength compared to the ones with unidirectional fabric with the same number of layers. Moreover, the negative correlation between the number of fabric layers and failure stress is more obvious here although the specimen with three fabric layers showed slightly higher failure stress compared to the two-layered ones with a failure stress higher by only 14.8 MPa.

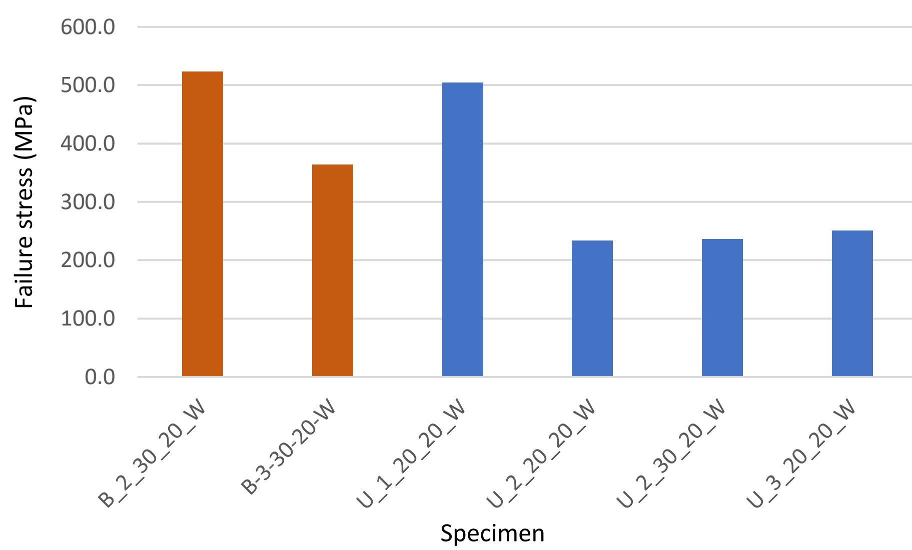

Figure 5.5: failure stress of all the wrap anchored specimens

All specimens anchored using wrap anchors failed due to fabric rupture, regardless of fabric type, composite length or the number of fabric layers. Moreover, no significant slip was observed on any wrapped specimen although specimen B_3_30_20_W exhibited some cracking at the surface.

The strain profiles of the fabric at failure of specimens with wrap anchors are compared in Figure 5.6. Unfortunately, only one strain profile is available for unidirectional specimens with wrap anchors, since the strain gauges got detached and/or got tangled up in the matrix layer during fabric slip which led to wrong strain data or sometimes no readings, so no correlation between the strain and the factors under consideration can be deducted. Although the difference in strain penetration between specimens with unidirectional and bidirectional fabric is relatively small, it is likely that the actual strain penetration of the specimen with unidirectional fabric is actually deeper than what is shown by the strain gauges since the measured strain of 0.9% at a depth of 20 mm is lower than the rupture strain. This is a result of unequal loading of the fabric strands. No significant strain was observed beyond 110 mm, 116 and 120 mm for specimens B_2_30_20_W, B-3-30-20-W and U_1_20_20_W respectively, which matches the trend noticed in specimens with other anchor types.

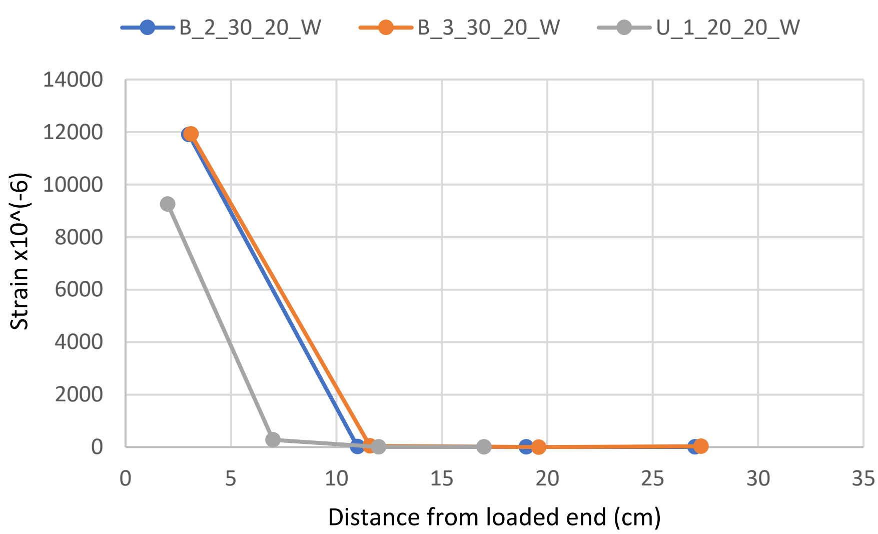

Figure 5.6: strain profiles of the fabric at failure of wrap anchored specimens

Additionally, wrap anchored specimens were compared in terms of the stress at slip initiation, average slip rate and the maximum recorded slip which are summarized in table 5.3. Like previous observations with other anchorage types, specimens with bidirectional fabric exhibited slip initiation at a higher stress compared to unidirectional specimens. Specimen B_3_30_20_W started to slip at a stress of 60.6 MPa which is 9.5 times that of specimen U_3_20_20_W that had the same number of fabric layers. Moreover, Specimens U_1_20_20_W and U_3_20_20_W demonstrated significantly low average slip rates compared to other specimens, at 0.05 mm/kN and 0.03 mm/kN, respectively, but this was expected since the maximum slip obtained from both specimens was low too. In addition, it was observed that slip initiation stress of the wrap anchored unidirectional specimens decreased with more fabric layers.

Table 5.3: slip measurements of wrap anchored specimens

Specimen	Slip initiation load (kN)	Slip initiation stress (MPa)	Average slip rate (mm/kN)	Maximum slip (mm)
B_3_30_20_W	1.6	60.6	0.28	2.47
U_1_20_20_W	1.0	31.9	0.05	0.76
U_2_20_20_W	0.6	9.6	0.13	1.72
U_3_20_20_W	0.6	6.4	0.03	0.74

5.4 Effect of anchor types on composite behaviour

The results of all anchor types were compared to each other to better understand their impact while other factors are fixed. The failure stress of all specimens with one or two fabric layers are plotted in Figure 5.7a and those of all three-layered specimens are shown in Figure 5.7b All specimens anchored using wrap anchors failed due to fabric rupture, regardless of fabric type, composite length or the number of fabric layers with one specimen showing some cracking at the surface. Moreover, all specimens anchored using spike anchors failed due to fabric rupture except for specimen U_2_20_20_S1 that experienced composite-substrate debonding prior to the fabric rupture which was a result of not connecting the spike anchor properly. Additionally, only multi-layered specimens exhibited visible signs of fabric slip with a spike anchor. Specimen U_1_20_20_M which is the only specimen anchored using a mechanical anchor, failed due to composite-substrate debonding. Furthermore, the failure mode noticed the most among non-anchored specimens was fabric rupture after some slip, with a considerable number that failed due to composite-substrate debonding. Other studies that experimented with multiple layers of FRCM stated that the increase of the composite thickness as well as the number of layers is associated with the composite-substrate debonding mode as it lowers the composite - substrate bond capacity, while the use of NSE technique changed the failure mode to premature fabric rupture as it provided more area of contact on three faces and thus provided better anchorage to the concrete substrate (Wakjira & Ebead, 2018; Younis & Ebead, 2018). This is evident in this study since all the specimens that failed due to composite – substrate debonding are non-anchored multi-layered specimens except for specimen U_2_20_20_S1 that was not anchored properly and the mechanically anchored specimen. All other specimens that failed due to premature rupture, ruptured because they were anchored and/or due to the unequal loading of the strands which caused the few loaded strands to rupture before the composite – substrate bond capacity was reached. Therefore, it can be deduced that anchor type and the overall composite thickness are the main factors that control the failure mode of the composite.

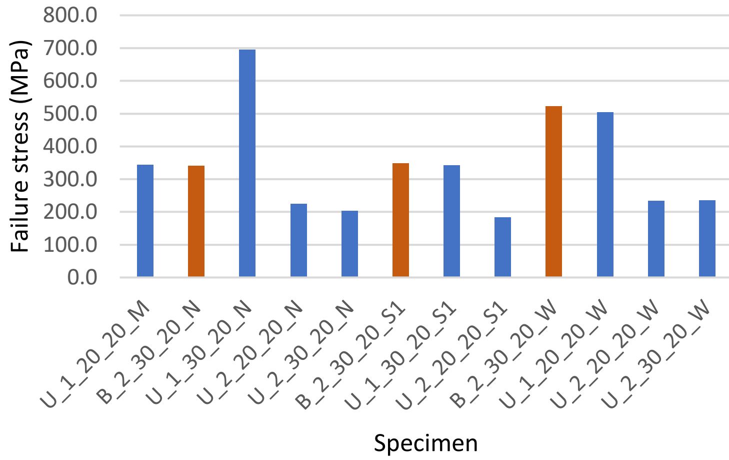

(a)

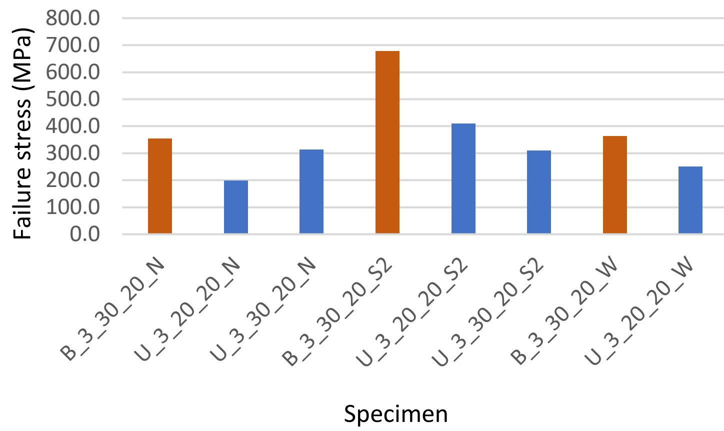

(b)

Figure 5.7: failure stress of all specimens with one or two fabric layers (a) and failure stress of all specimens with three fabric layers (b)

The strain profiles of all specimens with one or two fabric layers are plotted in Figure 5.8a and those of all three-layered specimens are shown in Figure 5.8b. Generally, it appears that specimens with three layers of fabric experienced deeper strain penetration into the composite than one-layered or two-layered specimens regardless of the anchor type. Like the case with slip initiation stress of unidirectional specimens, this may indicate that the additional layers have a lower bond efficiency. When comparing specimens with the same number of fabric layers, it can be noticed that in three-layered specimens, non-anchored specimens exhibited the deepest strain penetration while specimens with spike anchors showed the lowest. Specimens with a wrap anchor fell in between. Similar to the three-layered specimens, non-anchored specimens with two fabric layers exhibited the deepest strain penetration among the two-layered specimens. Despite experiencing shallower strain penetration, spike and wrap anchored specimens did not show a significant difference in the depth of strain penetration.

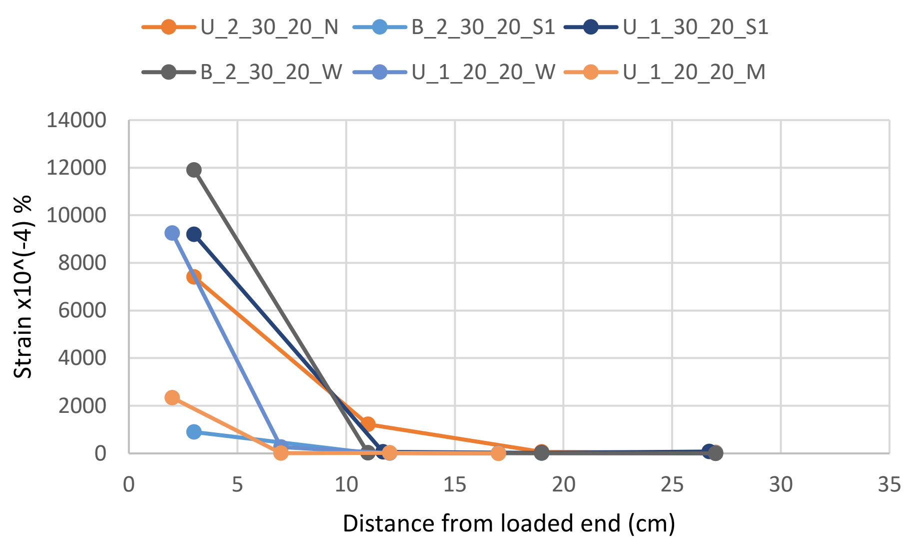

(a)

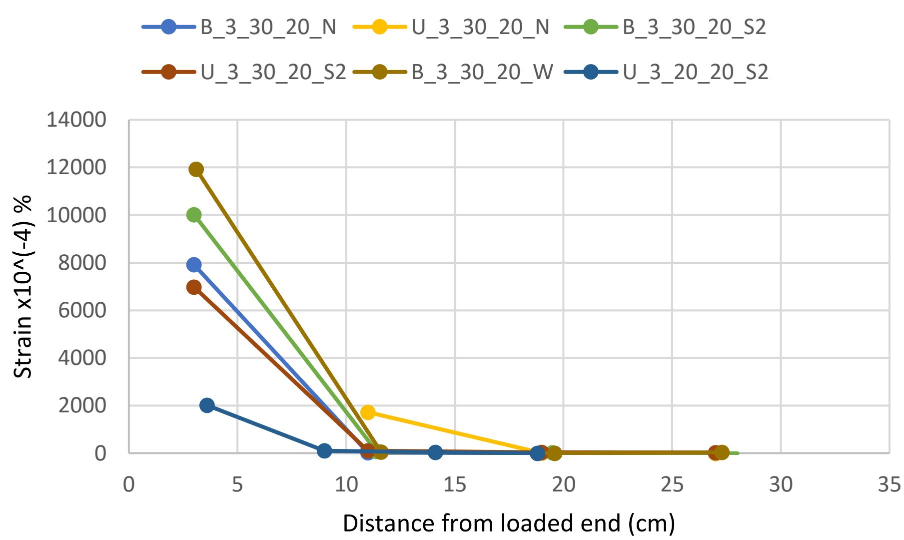

(b)

Figure 5.8: strain profiles of all specimens with one or two fabric layers (a) and strain profiles of all specimens with three fabric layers (b)

5.5 Bond behaviour modelling

Eligehausen et al. (1983) modified a widely accepted simple bond–slip relationship shown in Figure 5.9 and given by equations (1) and (2), corresponding to the first part of the curve and the second descending part, respectively, jointly with the equilibrium equation (3). The parameters τ_{max} (peak bond stress), s_m (slip at peak bond stress), p, and α are calibrated with experimental data.

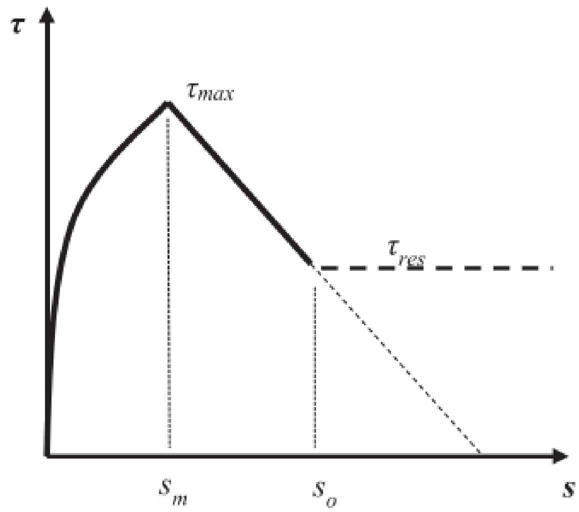

Figure 5.9: Eligehausen et al. (1983) modified bond–slip relationship

After defining the bond–slip relationship, the axial stress and slip profiles along the embedded length of the fabric can be plotted. Moreover, Pecce et al. (2001) proposed a method to calibrate the model using axial stress values calculated using experimental slip measurements in conjunction with equation (4).

For $s < s_m$,

$$\tau(s) = \tau_{\max} \left(\frac{s}{s_m}\right)^{\alpha} \quad (1)$$

For $s_m < s < s_0$

$$\tau(s) = \tau_{\max} \left(1 + p - p\frac{s}{s_m}\right) \quad (2)$$

$$A_c d\sigma = P_f \tau \mathrm{dx} \quad (3)$$

$$P_f A_\tau(s) = A_c A_\sigma(\sigma) \quad (4)$$

Where s = the slip value, τ(s) = the bond stress at the same slip value, Ac = cross-sectional area of the fabric, and Pf = perimeter of the fabric strands. The area underneath τ -s curve Aτ(s) and the area underneath the σ-ε curve Aσ(σ) are given by equations (5) and (6), respectively. The model is then calibrated by minimizing the error function given by equation (7).

$$A_{\tau}(s) = \frac{\tau s}{1+\alpha} \tag{5}$$

$$A_{\sigma}(\sigma) = \frac{\sigma^2}{2E} \tag{6}$$

$$e = \sqrt{\frac{\sum_{j=1,n}\left(\frac{\sigma_l^{th}-\sigma_l^{e}}{\sigma_l^{e}}\right)^2}{n}} \tag{7}$$

Where $\sigma_l^{th}$and σ_l^{e}= predicted and experimental stress values, n = number of data points, and E = Young's modulus. The 5 specimens modeled in this study are chosen to cover both fabric types with all variations of the number of fabric layers. The specimens selected for the modelling are B_2_30_20_W, B_3_30_20_S2, U_1_20_20_W, U_2_30_20_N, and U_3_30_20_S2. The specimens were calibrated individually employing the procedure above. Two of the calibrated axial stress curves are shown in Figure 5.10 as an example of the curve fitting, along with the bond stress–slip relationship obtained for every specimen. It is evident that the calibrated models of these specimens are missing the second descending part. The reason behind that is the failure mode of these specimens which was either a fabric rupture or a substrate – composite debonding that lead to a premature failure without the full development of the bond stress, which would happen in a matrix – fabric debonding failure.

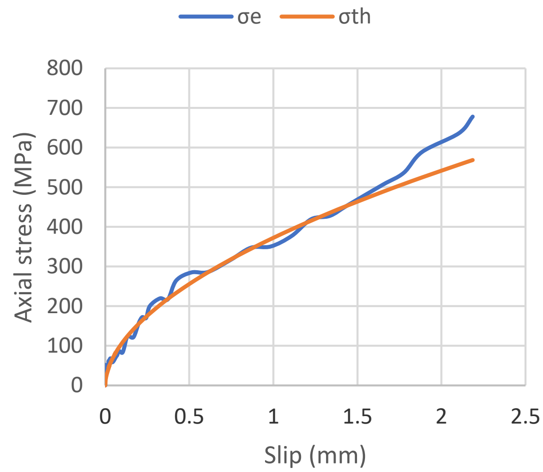

(a)

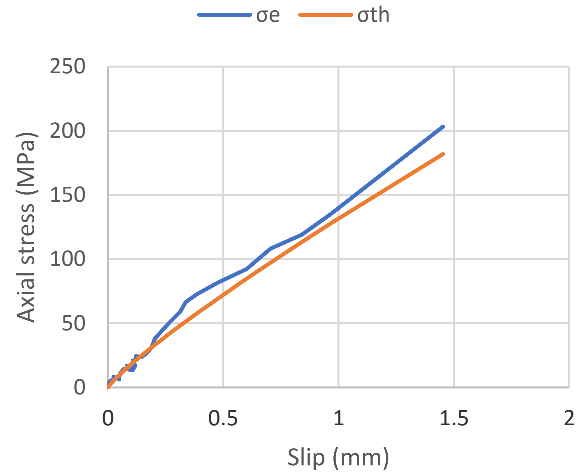

(b)

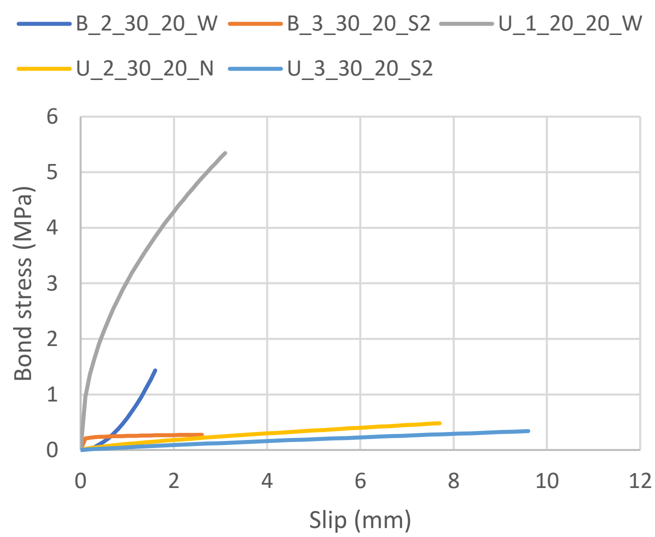

(c)

Figure 5.10: Calibrated stress–slip curves for specimens B_3_30_20_S2 (a) and U_2_30_20_N (b); and bond stress–slip curves for all modelled specimens (c)

The calibrated model parameters obtained from each beam are summarized in Table 5.4. When comparing the peak bond stress of these specimens, it can be observed that τ_{max} decreases with the increase of the number of fabric layers. This observation seems to agree with previous remarks in this study when comparing the strain penetration of different specimens. The specimens with higher number of fabric layers exhibited deeper strain penetration which also seems logical since lower bond strength requires deeper penetration to achieve equilibrium.

Table 5.4: Calibrated parameters for each specimen

	B_2_30_20_W	B_3_30_20_S2	U_1_20_20_W	U_2_30_20_N	U_3_30_20_S2
α	1.94	0.08	0.5	0.73	0.86
p	-	-	-	-	-
sm	1.59	2.64	3.13	7.73	9.61
τmax	1.42	0.27	5.37	0.48	0.34

As seen in Table 5.4, the high variability of parameter α affected the models significantly especially with only the first part of the bond-slip being available for the model, which made the effects even more prevalent. The slip value corresponding to the peak bond stress was generally lower for bidirectional specimens than the unidirectional ones and increased with more fabric layers regardless of the fabric type, which also supports previous trends observed with experimental results. Applying these parameters, the following equations are obtained.

When s < 1.59, for specimen B_2_30_20_W (2 layers of bidirectional fabric):

$$\tau(s) = 1.42 \left(\frac{s}{1.59}\right)^{1.94} \tag{8}$$

When s < 2.64, for specimen B_3_30_20_S2 (3 layers of bidirectional fabric):

$$\tau(s) = 0.27 \left(\frac{s}{2.64}\right)^{0.08} \tag{9}$$

When s < 3.13, for specimen U_1_20_20_W (1 layer of unidirectional fabric):

$$\tau(s) = 5.37 \left(\frac{s}{3.13}\right)^{0.5} \tag{10}$$

When s < 7.73, for specimen U_2_30_20_N (2 layers of unidirectional fabric):

$$\tau(s) = 0.48 \left(\frac{s}{7.73}\right)^{0.73} \tag{11}$$

When s < 9.61, for specimen U_3_30_20_S2 (3 layers of unidirectional fabric):

$$\tau(s) = 0.34 \left(\frac{s}{9.61}\right)^{0.86} \tag{12}$$

The slip profiles of the modelled specimens are presented in Figure 5.11. The profiles indicate that the fabric at the unloaded end of the composite of all the specimens experienced slip except for specimen U_1_20_20_W, which is not the case in the experimental data. This discrepancy between the predictive models and the experimental results is due to the use of localized data to describe overall behaviour, in addition to the premature failure that happened before the development of the bond-slip behaviour beyond the peak.

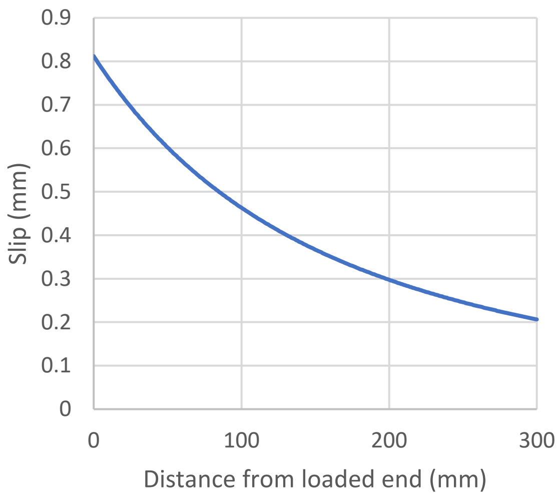

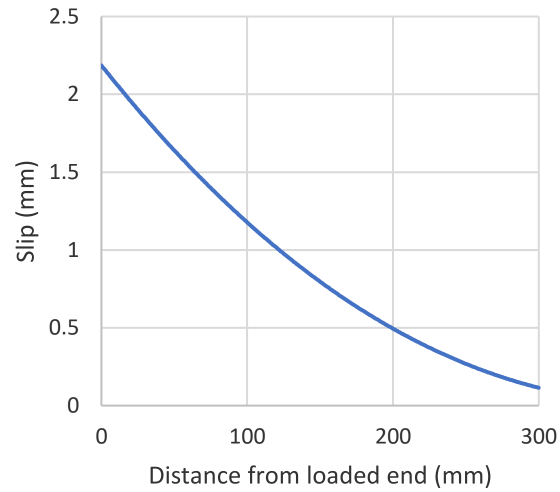

(a)

(b)

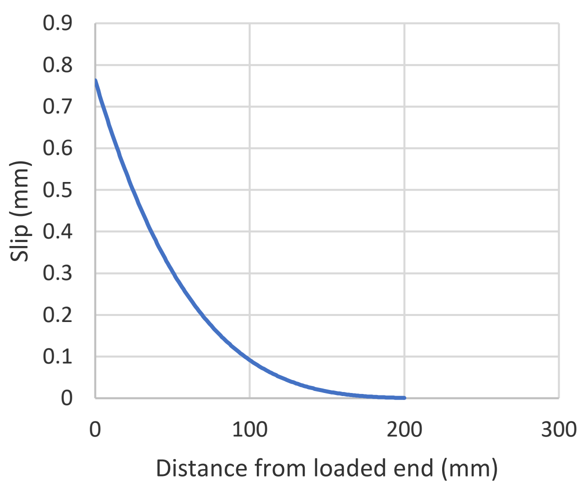

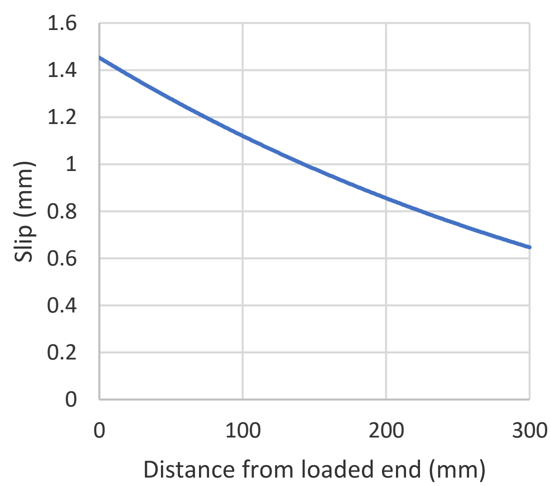

(c)

(d)

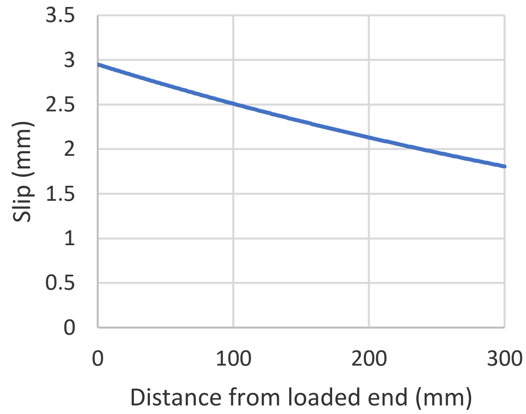

(e)

Figure 5.11: Slip profiles for specimens B_2_30_20_W (a), B_3_30_20_S2 (b), U_1_20_20_W (c), U_2_30_20_N (d), and U_3_30_20_S2 (e)

Moreover, the discrepancy is more evident in the axial stress profiles presented in Figure 5.12. The calibrated models do not show high reliability for design purposes. Nonetheless, these predictive models give a good idea on the trends associated with different variables and can provide a general perception on the composite behaviour for comparative purposes. The main limitation here is the experimental data which needs to be improved to calibrate more reliable models.

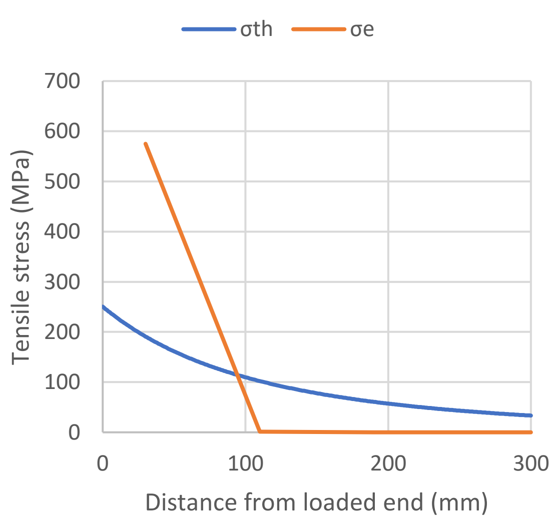

(a)

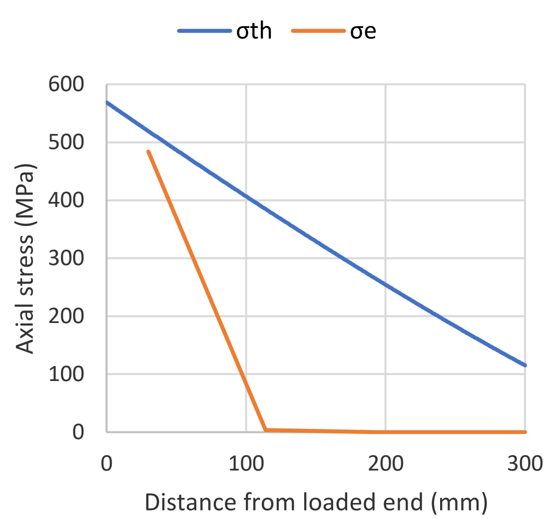

(b)

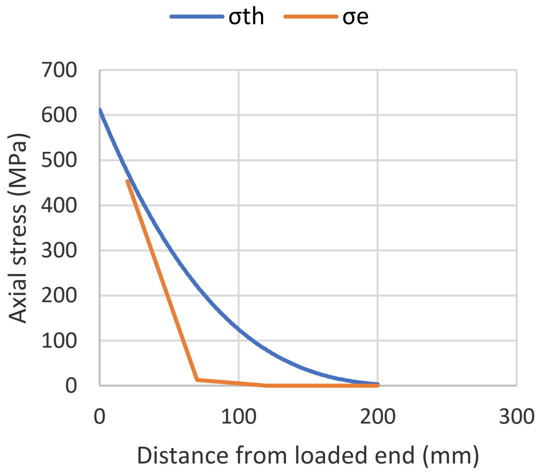

(c)

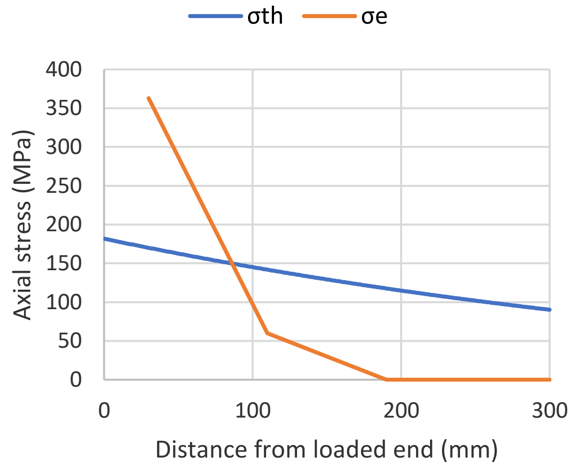

(d)

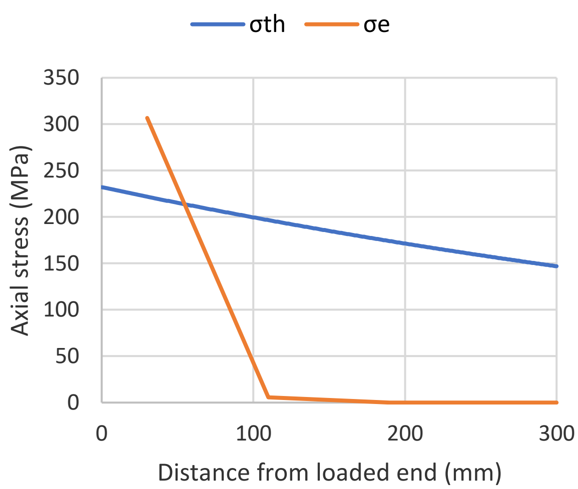

(e)

Figure 5.12: Axial stress profiles for specimens B_2_30_20_W (a), B_3_30_20_S2 (b), U_1_20_20_W (c), U_2_30_20_N (d), and U_3_30_20_S2 (e)

The bond stress profiles are shown in Figure 5.13. The average experimental bond stress was calculated between every two strain gauges using Equation (3). Since there is no strain gauge at the loaded end of the composite, calculating the experimental bond stress at the first portion of the profile was not possible. It is important to mention that with more strain gauges, the bond stress profile of the experimental data would be more accurate.

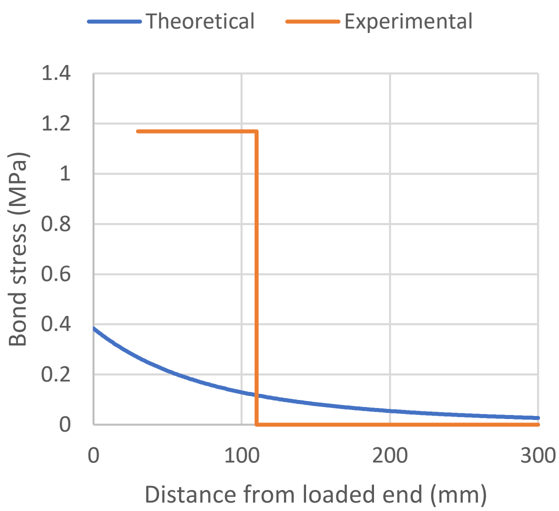
Theoretical
Experimental
Bond stress (MPa)
0
0.2
0.4
0.6
0.8
1
1.2
1.4
0
100
200
300
Distance from loaded end (mm)

(a)

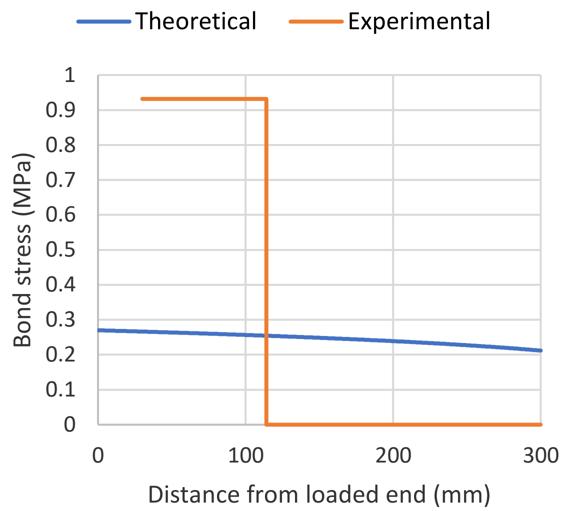
Theoretical
Experimental
Bond stress (MPa)
0
0.1
0.2
0.3
0.4
0.5
0.6
0.7
0.8
0.9
1
0
100
200
300
Distance from loaded end (mm)

(b)

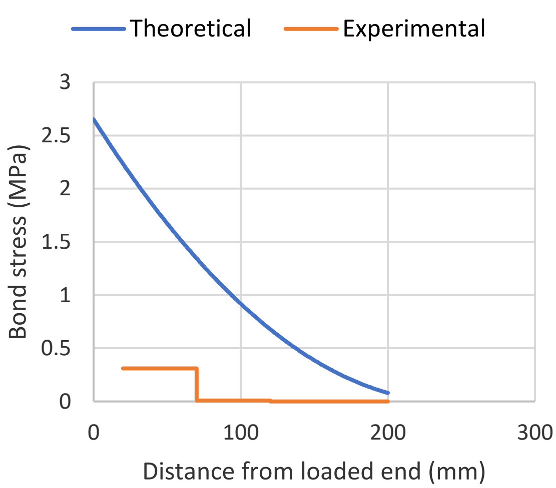
Theoretical
Experimental
Bond stress (MPa)
0
0.5
1
1.5
2
2.5
3
0
100
200
300
Distance from loaded end (mm)

(c)

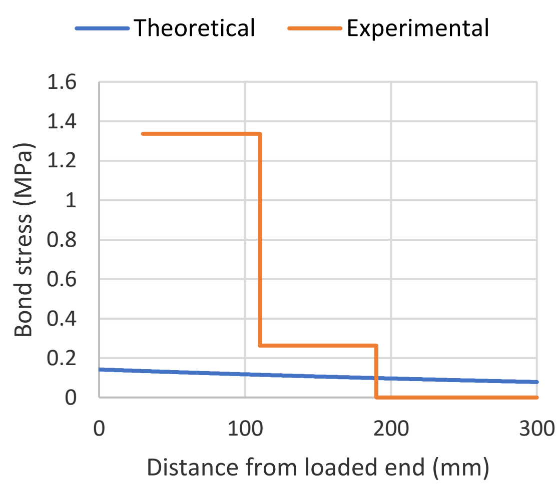
Theoretical
Experimental
Bond stress (MPa)
0
0.2
0.4
0.6
0.8
1
1.2
1.4
1.6
0
100
200
300
Distance from loaded end (mm)

(d)

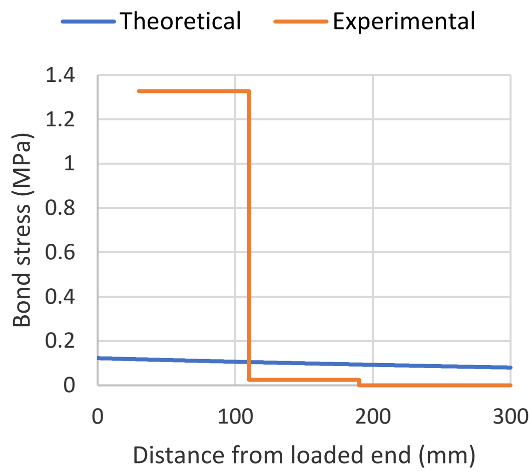

(e)

Figure 5.13:Bond stress profiles for specimens B_2_30_20_W (a), B_3_30_20_S2 (b), U_1_20_20_W (c), U_2_30_20_N (d), and U_3_30_20_S2 (e)

5.6 Effective length

Effective bond length of FRCM is the minimum length needed to develop the load-carrying capacity of the fabric – matrix interface just before the fabric starts debonding (D'Antino et al., 2014). The idealized load - slip curve for FRCM is shown in Figure 5.14a. Since most of the specimens ruptured in the free fabric and none displayed any debonding, it is difficult to make conclusions about the effective length based on the results of this study. Stress–transfer stages corresponding to different points of the idealized load - slip curve are presented in Figure 5.14b. All the specimens in this study failed between points O and B which correspond to the start of loading and the start of fabric – matrix debonding, respectively. However, since none of the specimens experienced debonding at the fabric – matrix interface, effective length will certainly be longer than the obtained values for strain penetration into the composite. The effective length is longer than 170 mm, 110 mm and 106 mm for non-anchored, wrap anchored and spike anchored specimens with unidirectional fabric on average, respectively. Moreover, the effective length is longer than 100 mm, 100 mm and 110 mm for non-anchored, wrap anchored and spike anchored specimens with bidirectional fabric on average, respectively. These values do not oppose Sabau's at al. (2017) findings that claimed the effective bond length to be between 200 mm and 330 mm. Furthermore, these values indicate that the use of bidirectional fabric and anchorage systems decreases the strain penetration into the composite and correspondingly, the effective length is shortened.

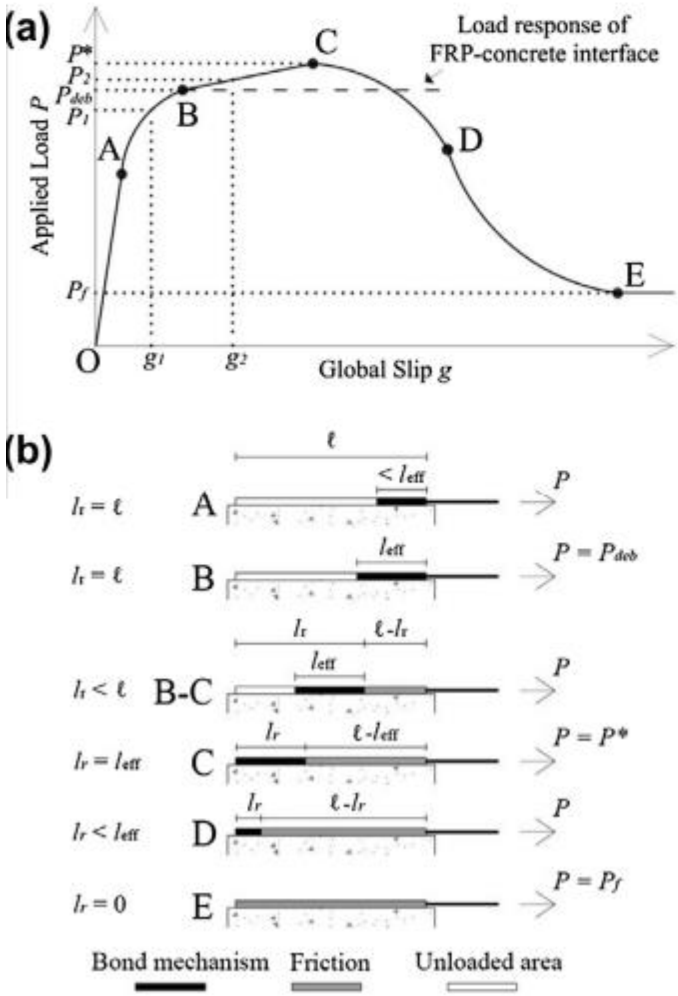

Figure 5.14: idealized load - slip curve for FRCM (a) and the corresponding stress–transfer stages (D'Antino et al., 2014)

5.7 Unexpected results and implications for design

The relatively low failure load was one of the main issues faced during experimentation. One of the main reasons behind the low failure load is that the fabric strands were not loaded equally. The design choice to make the specimens 200 mm wide amplified the issue and made the effects of the unequal loading more evident. Most other similar studies built the composite specimens with approximately 25% of the width of the specimens in this study (Sabau et al., 2017; D'Antino & Poggi, 2019; D'Antino & Papanicolaou, 2018). The bonded width was initially intended to be one of the studied parameters of this research which was not pursued due to time limitations. It is possible that a narrower bonded region would have provided more consistent results. In addition to the width, the new gripping system adopted in this experiment made it harder to assure equal distribution of the load among the fabric strands in multi-layered specimens, since the bar needed to be rolled after the fabric is clamped. This meant that the fabric layers on the outside of the roll would have a bigger perimeter and thus, would take higher loads. However, every specimen that exhibited noticeable difference in the loading among the layers was re-set up to ensure at least visibly equal loading. These two issues combined had a significant impact on the uniformity of fabric loading.

Moreover, another factor that may have affected the results is the thickness of the cementitious matrix layer. Most similar studies used a 4 mm – 5 mm thick matrix layer (D'Antino et al., 2014; Sabau et al., 2017; Sneed et al., 2016; Donnini et al., 2019). The DIC external strain measurements generally did not match the internal strain values obtained from the strain gauges, which is expected once slip has occurred (i.e., loss of compatibility between fabric and mortar). Even when the internal and external strain values are close in the case of specimens with low strains like B_2_30_20_S1, there was a difference in the position (i.e., strains penetrate beyond 30 mm for the fabric vs 0-20 mm for the matrix). This may be due to a shear lag effect created as a result of the thickness of the matrix layer; a thinner mortar may have shown external strain profiles closer to the fabric strains. This can be a good area to research to better understand the effects of the matrix thickness.

As mentioned earlier, some of the strain data of the specimens is missing which made it harder to compare the strain profiles at higher loads. One of the reasons is the detachment of strain gauges from the fabric either during matrix application to the fabric or during the test, leading to no readings. Other reasons include the strain gauges being tangled up in the matrix layer which led to negative strain readings at higher slip. It seems the polyurethane protective layer applied to the strain gauges was too thick for some of them to get tangled up in the matrix and give negative strain readings. In addition, few specimens with relatively high failure stress showed significantly low strains compared to other specimens with lower failure stress. It is possible that the instrumented strands in these specimens were not the critical ones.

To avoid similar issues and to achieve better results in future applications, it is recommended to design the FRCM composites with a width range of approximately 50 mm - 60 mm (3 – 4 strands) to reduce the chances of unequal loading of the strands. While the newly introduced gripping system was compact which provided more space for testing, and saved a lot of time setting-up specimens for testing since it did not require the application of epoxy, it is not recommended to use it with multi-layered specimens. The use of multiple fabric layers or a thick matrix will lead to a premature composite debonding failure and if properly anchored with a spike or wrap anchor, will lead to a premature rupture.

Additionally, it is recommended to trowel the matrix layers carefully to avoid damaging the strain gauges and to apply a thin layer of polyurethane to avoid entanglement of the strain gauge in the matrix if the protective layer is too thick.

6.0 Conclusion

This study discussed the effects of varying parameters like the number of C-FRCM layers (1, 2 and 3 layers), different anchorage configurations (non-anchored, spike anchor, wrap anchor and mechanical anchor), bond length (300 or 200 mm) and the fabric type (unidirectional and bidirectional) on the direct shear behaviour of C-FRCM.

All properly anchored specimens using spike and wrap anchors, failed due to fabric rupture. Moreover, a considerable number of the non-anchored specimens failed due to composite-substrate debonding although the failure mode observed the most for non-anchored specimens was fabric rupture due to the unequal loading of the strands which caused the few loaded strands to rupture before the composite – substrate bond capacity was reached. These observations agree with other studies which stated that the increase of the composite thickness as well as the number of layers without anchoring the composite to the substrate, is associated with the composite-substrate debonding mode as it lowers the composite - substrate bond capacity. Therefore, it can be deduced that anchor type and the overall composite thickness are the main factors that control the failure mode of the composite.

Moreover, specimens demonstrated a significant difference in failure stress based on the number of layers as the failure stress decrease with higher number of fabric layers. This result can be attributed to the difficulty experienced while trying to ensure equal loading of the fabric strands for specimens with multiple layers and a higher number of strands during installation. Specimens with bidirectional fabric withstood higher stresses than the unidirectional ones with the same number of layers due to the higher material strength of the bidirectional fabric, while the length of the bonded region was not correlated with the failure stress since the failure modes of these specimens were not governed by debonding.

Furthermore, specimens with bidirectional fabric demonstrated shallower penetration of the strain into the composite. A possible explanation for this observation is that the horizontal fabric strands provide some anchorage for the longitudinal strands. They also exhibited slip initiation at a higher stress compared to unidirectional specimens, while the maximum global slip was more correlated to higher failure stress. Slip initiation stress of unidirectional specimens decreased with more fabric layers which may indicate that the additional layers have a lower bond efficiency. Which is the same reason it generally appears that specimens with three layers of fabric experienced deeper strain penetration into the composite than one-layered or two-layered specimens regardless of the anchor type.

When comparing specimens with the same number of fabric layers, non-anchored specimens exhibited the deepest strain penetration while specimens with spike anchors showed the lowest. This indicates that the use of bidirectional fabric and anchorage systems decreases the strain penetration into the composite and correspondingly, the effective length is shortened. The effective length is longer than 170 mm, 110 mm and 106 mm for non-anchored, wrap anchored and spike anchored specimens with unidirectional fabric on average, respectively. Moreover, the effective length is longer than 100 mm, 100 mm and 110 mm for non-anchored, wrap anchored and spike anchored specimens with bidirectional fabric on average, respectively. These values do not oppose findings in other studies that claimed the effective bond length to be between 200 mm and 330 mm.

The relatively low failure load was one of the main issues faced during experimentation. One of the main reasons behind the low failure load is that the fabric strands were not loaded equally. The design choice to make the specimens 200 mm wide made the issue more evident. In addition to the width, the new gripping system adopted in this experiment made it harder to assure equal distribution of the load among the fabric strands in multi-layered specimens, since the bar needed to be rolled after the fabric is clamped. To achieve better results in future applications, it is recommended to design the FRCM composites with a width range of approximately 50 mm - 60 mm (3 – 4 strands) to reduce the reduce the chances of unequal loading of the strands. Furthermore, it is not recommended to use the newly introduced gripping system with multi-layered specimens although it was compact which provided more space for testing, and saved a lot of time setting-up specimens for testing since it did not require the application of epoxy.

DIC external strain measurements generally did not match the internal strain values obtained from the strain gauges, which is expected once slip has occurred. Even when the internal and external strain values were close, there was a difference in the position (e.g., strains penetrate beyond 30 mm for the fabric vs 0-20 mm for the matrix). This may be due to a shear lag effect created as a result of the thickness of the matrix layer; a thinner mortar may have shown external strain profiles closer to the fabric strains. This can be a good area to research to better understand the effects of the matrix thickness.

7.0 References

Aljazaeri, Z., Janke, M., Myers, J. (2019). A novel and effective anchorage system for enhancing the flexural capacity of RC beams strengthened with FRCM composites. *Composite Structures*, 20–28.

Asgharigharakheili, H., (2022). Investigation of Tensile Strength of Carbon Fabric-Reinforced Cementitious Matrix (FRCM) at High Temperatures. [Master's thesis]. University of Ottawa, Ottawa.

Azam, R., Soudki, K., West, J.S., and Noël, M. (2018). Shear strengthening of RC deep beams with cement-based composites. *Engineering Structures*, Vol. 172, 929-937.

Azam, R., Soudki, K., West, J.S., and Noël, M. (2019). CFRP grid embedded in mortar for strengthening of shear-critical RC beams. *Magazine of Concrete Research*, Vol. 71, No. 14, 761-772.

Bournas, D., Pavese, A., Tizani, W. (2015). Tensile capacity of FRP anchors in connecting FRP and TRM sheets to concrete. *Engineering Structures*, 72-81.

D'Antino, T., Carloni, C., Sneed, L., Pellegrino, C. (2014). Matrix–fiber bond behavior in PBO FRCM composites: A fracture mechanics approach. *Engineering Fracture Mechanics*, 94–111.

D'Antino, T., Papanicolaou, C. (2018). Comparison between different tensile test set-ups for the mechanical characterization of inorganic-matrix composites. *Construction and Building Materials*, 140–151.

D'Antino, T., Poggi, C. (2019). Stress Redistribution in Glass Fibers of G-FRCM Composites. *Key Engineering Materials*, 520-527.

Donnini, J., Chiappini, G., Lancioni, G., Corinaldesi, V. (2019). Tensile behavior of glass FRCM systems with fabrics' overlap: Experimental results and numerical modeling. *Composite Structures*, 398–411.

Eligehausen, R., E. P. Popov, and V. V. Bertero. (1983). Local bond stress–slip relationships of deformed bars under generalized excitations. Rep. No. 83/23. Berkeley, CA: Earthquake

Engineering Research Center, University of California.

Gonzalez-Libreros, J., Sneed, L., D'Antino, T., Pellegrino, C. (2017). Behavior of RC beams strengthened in shear with FRP and FRCM composites. *Engineering Structures*, 830-842.

Marcinczak, D., Trapko, T., Musiał, M. (2019). Shear strengthening of reinforced concrete beams with PBO-FRCM composites with anchorage. *Composites*, 149–161.

Marcinczak, D., Trapko, T. (2019). DIC method in the research of RC beams strengthened with PBO-FRCM materials. *E3S Web of Conferences*, 97, 03008.

Pecce, M., Manfredi, G., Realfonzo, R., Cosenza, E. (2001). Experimental and analytical evaluation of bond properties of GFRP bars. *J. Mater. Civ. Eng.* 13 (4), 282–290.

Pohoryles, D., Melo, J., Rossetto, T., Fabian, M., McCague, C., Stavrianaki, K., Lishman, B., Sargeant, B. (2017). Use of DIC and AE for Monitoring Effective Strain and Debonding in FRP and FRCM-Retrofitted RC Beams. *Journal of Composites for Construction*, p.04016057.

Sabau, C., Gonzalez-Libreros, J., Sneed, L., Sas, G., Pellegrino, C., Taljsten, B. (2017). Use of image correlation system to study the bond behavior of FRCM-concrete joints. *Materials and Structures*, 50:172.

Sneed, L., Verre, S., Carloni, C., Ombres, L. (2016). Flexural behavior of RC beams strengthened with steel-FRCM composite. *Engineering Structures*, 686–699.

Tekieli, M., De Santis, S., de Felice, G., Kwiecien´, A., Roscini, F. (2017). Application of Digital Image Correlation to composite reinforcements testing. *Composite Structures*, 670-688.

Trapko, T., Musiał, M. (2017). PBO mesh mobilization via different ways of anchoring PBO-FRCM reinforcements. *Composites*, 67-74.

Trapko, T., Urbanska, D., Kaminski, M. (2015). Shear strengthening of reinforced concrete beams with PBO-FRCM composites. *Composites*, 63-72.

Wakjira, T., Ebead, U. (2018). Hybrid NSE/EB technique for shear strengthening of reinforced concrete beams using FRCM: Experimental study. *Construction and Building Materials*, 165-177.

Wakjira, T., Ebead, U. (2019). Internal transverse reinforcement configuration effect of EB/NSE-FRCM shear strengthening of RC deep beams. *Composites*, 758–772.

Younis, A., Ebead, U. (2018). Bond characteristics of different FRCM systems. *Construction and Building Materials*, 610-620.

Younis, A., Ebead, U., Shrestha, K. (2017). Different FRCM systems for shear-strengthening of reinforced concrete Beams. *Construction and Building Materials*, 514–526.